MODELING OF TWO STAGE NOZZLE-FLAPPER TYPE ELECTROHYRAULIC SERVOVALVES

A THESIS SUBMITTED TO
THE GRADUATE SCHOOL OF NATURAL AND APPLIED SCIENCES
OF
MIDDLE EAST TECHNICAL UNIVERSITY

BY

Ahmet Can Afatsun

IN PARTIAL FULFILLMENT OF THE REQUIREMENTS
FOR
THE DEGREE OF Master of Science
IN
Mechanical Engineering

May 2019

Approval of the thesis:

MODELING OF TWO STAGE NOZZLE-FLAPPER TYPE ELECTROHYRAULIC SERVOVALVES

submitted by **Ahmet Can Afatsun** in partial fulfillment of the requirements for the degree of **Master of Science in Mechanical Engineering Department, Middle East Technical University** by,

Prof. Dr. Halil Kalıpçılar
Dean, Graduate School of **Natural and Applied Sciences** _____

Prof. Dr. M. A. Sahir Arıkan
Head of Department, **Mechanical Engineering** _____

Prof. Dr. R. Tuna Balkan
Supervisor, **Mechanical Engineering, METU** _____

Examining Committee Members:

Prof. Dr. M. Haluk Aksel
Mechanical Engineering, METU _____

Prof. Dr. R. Tuna Balkan
Mechanical Engineering, METU _____

Prof. Dr. Y. Samim Ünlüsoy
Mechanical Engineering, METU _____

Prof. Dr. Bülent E. Platin
Mechanical Engineering, METU _____

Assoc. Prof. Dr. S. Çağlar Başlamışlı
Mechanical Engineering, Hacettepe University _____

Date: 29.05.2019

I hereby declare that all information in this document has been obtained and presented in accordance with academic rules and ethical conduct. I also declare that, as required by these rules and conduct, I have fully cited and referenced all material and results that are not original to this work.

Name, Surname: Ahmet Can Afatsun

Signature:

ABSTRACT

MODELING OF TWO STAGE NOZZLE-FLAPPER TYPE ELECTROHYRAULIC SERVOVALVES

Afatsun, Ahmet Can
Master of Science, Mechanical Engineering
Supervisor: Prof. Dr. R. Tuna Balkan

May 2019, 130 pages

In this thesis, a detailed mathematical model for a double stage nozzle-flapper type servovalve is developed focusing on its hydraulics. Such valves must comply with very strict performance requirements of aerospace and military industries. To meet these requirements, parts of such a servovalve must be manufactured within the tolerances as low as a few microns. Considering the servovalve consists of many parts that influence overall performance, it becomes obvious that the servovalve must be designed carefully as a system by understanding the effect of deviations of all parameters related to it. Unfortunately, the relations used to define the behavior of servovalve hydraulics in the literature have shortcomings around the operating point. This study is conducted with the intention of fulfilling the need of a simulation model that offers high accuracy on the entire working range. To create such a model, several CFD analyses are carried out using the commercial software ANSYS Fluent®. Available turbulence models' and wall treatment functions' performances are compared with the experimental data to find out which models are most suitable to conduct such analyses. Results of these numerical analyses are used to develop more accurate analytical models for both first and second stages. These models are combined in a system simulation model created by using SimScape® blocks. This

final model is tested with a commercial valve's parameters, provided by the manufacturer. The results are accurate comparing to the datasheet values.

Keywords: Servovalve, Nozzle-Flapper Valve, Spool Valve, Flow Through Orifice, Parameter Optimization

ÖZ

İKİ KADEMELİ NOZUL-KANAT TİPİ ELEKTROHİDROLİK SERVOVALFLERİN MODELLENMESİ

Afatsun, Ahmet Can
Yüksek Lisans, Makina Mühendisliği
Tez Danışmanı: Prof. Dr. R. Tuna Balkan

Mayıs 2019, 130 sayfa

Elektronik ve hidrolik donanımlar arasında ara yüz oluşturma işlevi olan elektro hidrolik servovalfler, elektronik tahrikin basitliği ile hidrolik eyleyicilerin yüksek güç yoğunluğunu bir araya getirirler. Servovalflerin hidrolik preslerden füzelere kadar oldukça geniş kullanım alanları vardır. Bu tez, üstün dinamik başarımları, güvenilirlikleri ve küçük boyutları nedeniyle havacılık ve savunma uygulamalarında tercih edilen çift kademeli nozul-kanat tipi servovalflere yoğunlaşmaktadır. Bu valflerin havacılık ve savunma alanlarında kullanılan her ürün gibi oldukça katı başarım gereksinimlerini karşılamaları gerekmektedir. Bu gereksinimlerin karşılanması için servovalf parçalarının birkaç mikronu geçmeyen geometrik toleranslar içerisinde üretilmesi gerekir. Servovalfin tüm sistem başarımını etkileyen birçok parçadan oluştuğu göz önüne alındığında, tasarımın sistemi etkileyen tüm parametrelerin etkilerini anlayarak dikkatli bir şekilde yapılması gerektiği ortaya çıkmaktadır. Ne yazık ki, literatürde servovalf hidroliğini tanımlayan denklemler çalışma noktası çevresinde hatalı sonuçlar vermektedir. Bu tezde, tüm çalışma bölgesinde yüksek doğrulukta sonuç verecek bir benzetim modeli geliştirilmiştir. Modeli eniyilemek için ANSYS Fluent® ticari yazılımı ile hesaplamalı akışkan dinamiği (HAD) çözümlemelerinden faydalanılmıştır. Mevcut türbülans modelleri ve duvar dibi fonksiyonlarının başarımları, en uygun modelleri saptamak amacıyla

deneysel verilerle karşılaştırılmıştır. Sayısal çözümlemeyle elde edilen sonuçlar kullanılarak hem birinci hem de ikinci kademe için doğruluğu daha yüksek analitik modeller türetilmiştir. Bu modeller ile SimScape® blokları kullanılarak tüm sistem için bir benzetim modeli oluşturulmuştur. Bu model, ticari bir valfin üreticisi tarafından sağlanan parametreleriyle test edilmiştir. Öngörülen çıktıların katalog verileriyle tutarlı olduğu görülmüştür.

Anahtar Kelimeler: Servovalf, Nozul-Kanat Valfi, Sürgülü Valf, Orifis Akışı, Parametre Eniyilemesi

To my family

ACKNOWLEDGEMENTS

First, I would like to express my sincere appreciation to my thesis supervisor Prof. Dr. Tuna BALKAN for his support and guidance throughout my thesis study.

I am grateful for the patience Nergis ÖZKÖSE has shown me throughout my thesis study. Her support made me move on whenever my motivation deteriorated.

Another big thanks is certainly going to my old friend Ümit YERLİKAYA, who introduced me to ROKETSAN Inc. in the first place. His friendship has been and will always be priceless to me.

I am in debt of gratitude to my manager Aslı AKGÖZ BİNGÖL in ROKETSAN Inc. for her friendly support and advices.

I also owe thanks to my department's advisor Prof. Dr. Bülent Emre PLATİN who helped me to compose and refine the scientific reports related to my thesis throughout the study.

I am also grateful for having my friends Tevfik Ozan FENERCİOĞLU, Hasan YETGİN and Hasan Baran ÖZMEN, and sharing the same cubical with them in the workplace for years. Their presence is keeping the happiness in the equation in my professional life and I sincerely hope our friendship lasts till the end of our lives.

Last and certainly the most, I wish to express my sincere thanks to my father Sedat AFATSUN, my mother Nursel AFATSUN and my beloved brothers Oğuzhan and Furkan AFATSUN for the support, joy and peace they have given me all my life. They are the proof that a family is the most precious thing that a person can have.

TABLE OF CONTENTS

LIST OF TABLES

LIST OF FIGURES

LIST OF ABBREVIATIONS

AT	:	Chamber A to return port
BT	:	Chamber B to return port
CFD	:	Computational Fluid Dynamics
FS	:	Full stroke
PA	:	Pressure supply to Chamber A port
PB	:	Pressure supply to Chamber B port
RANS	:	Reynolds Averaged Navier Stokes
RNG	:	Renormalization Group
w/	:	With
w/o	:	Without

LIST OF SYMBOLS

A	:	Any area [m^2]
A_f	:	Fixed orifice area [m^2]
A_{in}	:	Inlet area of a control volume [m^2]
A_n	:	Nozzle area [m^2]
A_s	:	Spool end area [m^2]
A_{out}	:	Outlet area of a control volume [m^2]
B	:	Radial clearance between a spool and its sleeve [m^2]
c_c	:	The damping coefficient obtained when F_c is linearized with respect to $\dot{x_s}$ [N·m/(m/s)]
C_D	:	Any discharge coefficient
$C_{D,0}$	:	Discharge coefficient of a critical lapped spool port
$C_{D,e}$	:	Discharge coefficient of the exit orifice
$C_{D,f}$	:	Discharge coefficient of the fixed orifice
$C_{D,n}$	:	Discharge coefficient of the nozzle's fixed orifice part
$C_{D,s}$	:	Discharge coefficient of an underlapped spool port
$C_{D,v}$	:	Discharge coefficient of the nozzle's variable orifice part
C_θ	:	Underlapped spool port discharge coefficient correction term
c_{FS}	:	Overall damping on first stage [N·m·s]
c_n	:	The damping coefficient obtained when T_n is linearized with respect to $\dot{x_s}$ [N·m/(m/s)]

c_s	:	Spool damping [N/(m/s)]
c_{SS}	:	Overall damping on the second stage [N/(m/s)]
D	:	Any diameter [m]
D_c	:	Curtain diameter [m]
D_e	:	Exit orifice diameter [m]
D_f	:	Fixed orifice diameter [m]
D_n	:	Nozzle diameter [m]
D_s	:	Spool diameter [m]
e	:	Eccentricity between a spool and its sleeve [m]
F_B	:	Bernoulli force on the spool [N]
F_c	:	Control force [N]
F_l	:	Force applied on the flapper by the fluid jet from the left first stage branch nozzle [N]
F_r	:	Force applied on the flapper by the fluid jet from the right first stage branch nozzle [N]
F_x	:	The fluid force on the spool on the axial direction [N]
$\hat{\imath}$	:	Unit vector in the axial direction
J	:	Total error calculated by the penalty function
J_{FS}	:	Inertia of the first stage [N·m·s^2]
k_B	:	Bernoulli force spring coefficient [N/m]
K_B	:	Bernoulli force constant
k_c	:	The spring coefficient obtained when F_c is linearized with respect to x_f [N/m]

k_{fb}	:	Stiffness of the feedback spring [N/m]
k_{ft}	:	Stiffness of the flexure tube [N·m/rad]
k_n	:	The spring coefficient obtained when T_n is linearized with respect to θ [N·m/rad]
K_{ps}	:	Pressure sensitivity [Pa/m]
k_T	:	Torque constant of the torque motor [N·m/mA]
L	:	Any length [m]
L_{AT}	:	Lap length of port AT [m]
L_{BT}	:	Lap length of port BT [m]
L_c	:	Lap length of a nozzle [m]
L_d	:	Damping length of the spool [m]
L_e	:	Spool port opening [m]
L_{ef}	:	Exit length of a fixed orifice [m]
L_{en}	:	Exit length of a nozzle [m]
L_f	:	Distance from flapper pivot point to nozzle axis [m]
L_{PA}	:	Lap length of port PA [m]
L_{PB}	:	Lap length of port PB [m]
L_s	:	Distance from flapper pivot point to the point where the feedback spring touches the spool [m]
L_t	:	Transition length in Anderson's spool orifice model [m]
M	:	Overlapped spool port flow rate formula correction term
m_s	:	Spool mass [kg]

$\hat{n}_{in}$	:	Unit vector normal to the inlet of a control volume
$\hat{n}_{out}$	:	Unit vector normal to the outlet of a control volume
P_A	:	Pressure at Chamber A [Pa]
P_B	:	Pressure at Chamber B [Pa]
P_c	:	Control pressure (pressure difference between the ends of the spool) [Pa]
P_e	:	Exit pressure [Pa]
P_i	:	Intermediate pressure when a nozzle and a fixed orifice are connected in serial [Pa]
P_{in}	:	Pressure at the upstream of an orifice [Pa]
P_l	:	Pressure on the left first stage branch [Pa]
P_L	:	Load pressure [Pa]
P_{out}	:	Pressure at the downstream of an orifice [Pa]
P_r	:	Pressure on the right first stage branch [Pa]
P_s	:	Supply pressure [Pa]
P_T	:	Return (tank) pressure [Pa]
$\hat{r}$	:	Unit vector in the radial direction
R	:	Any radius [m]
$\vec{R}$	:	Force exerted on the control volume by its walls [N]
R_s	:	Spool radius [m]
R_x	:	Force exerted on the control volume by its walls on the axial direction [N]

Re	:	Reynolds number
Re^*	:	Estimated Reynolds number
$\widetilde{Re}$	:	$\log(Re^* + 1)$
Q	:	Any flow rate [m^3/s]
Q_{AT}	:	Flow rate from Chamber A to return [m^3/s]
Q_{BT}	:	Flow rate from Chamber B to return [m^3/s]
Q_l	:	Flow rate of the fluid jet from the nozzle on left first stage branch [m^3/s]
Q_L	:	Load flow rate [m^3/s]
Q_{OL}	:	Flow rate through an overlapped orifice [m^3/s]
Q_{PA}	:	Flow rate from pressure supply to Chamber A [m^3/s]
Q_{PB}	:	Flow rate from pressure supply to Chamber B [m^3/s]
Q_r	:	Flow rate of the fluid jet from the nozzle on right first stage branch [m^3/s]
Q_{UL}	:	Flow rate through an underlapped orifice [m^3/s]
T_n	:	Torque on the armature assembly applied by the fluid jets from the nozzles [N·m]
T_{tm}	:	Torque applied by the torque motor [N·m]
u_l	:	Velocity of the fluid jet from the nozzle on left first stage branch [m/s]
u_r	:	Velocity of the fluid jet from the nozzle on right first stage branch [m/s]
V	:	Any velocity [m/s]
$\vec{V}_{in}$	:	Velocity vector at the inlet of a control volume [m/s]
$\vec{V}_{out}$	:	Velocity vector at the outlet of a control volume [m/s]
w	:	Spool port gradient [m]

x	:	Curtain length [m]
x_0	:	Curtain length when the flapper is at null position [m]
$\tilde{x}_0$	:	The curtain length that makes the pressure sensitivity maximum [m]
x_f	:	Flapper position at nozzle axis [m]
$\dot{x_f}$	:	Flapper velocity at nozzle axis [m/s]
$\ddot{x_f}$	:	Flapper acceleration at nozzle axis [m/s^2]
x_s	:	Spool position [m]
$\dot{x_s}$	:	Spool velocity [m/s]
$\ddot{x_s}$	:	Spool acceleration [m/s^2]
α	:	Bevel angle (outer conical angle) of a nozzle [°]
β	:	Inner conical of a nozzle [°]
ΔP	:	Pressure drop between two points [Pa]
θ	:	Spool port opening angle [rad]
θ_f	:	Rotational position of the flapper [rad]
$\dot{\theta_f}$	:	Rotational velocity of the flapper [rad/s]
$\ddot{\theta_f}$	:	Rotational acceleration of the flapper [rad/s^2]
μ	:	Dynamic viscosity of the working fluid [kg/(m·s)]
ρ	:	Mass density of the working fluid [kg/m^3]

CHAPTER 1

INTRODUCTION

1.1. What is Servovalve?

The term “servovalve”, is apparently made up of two separate words: servo and valve. “Servo”, or in the long form “servomechanism” means an automatic feedback control system in which the output is mechanical position or one of its derivatives, while “valve” is the common name for devices which are used to control the flow of fluids [1]. By using a servovalve, the flow is controlled by controlling the position of a moving body in the valve. In certain classes of valves, like check valves or solenoid on/off valves, the purpose is to allow the fluid to flow or not, but the flow rate is not controlled. In servovalves, the purpose is to control the flow rate precisely and bidirectionally. A simple sketch of a spool valve, which is the main component of proportional valves (i.e., single stage servovalves), is given in Figure 1.1 to illustrate how the flow rate is controlled.

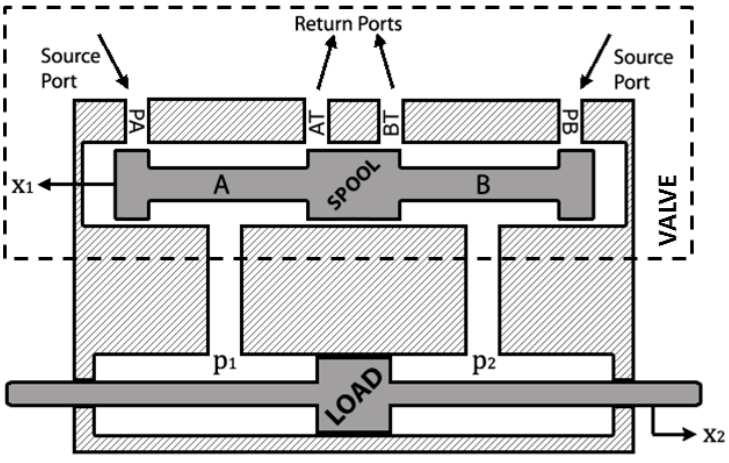

Figure 1.1 – A simple sketch of a spool valve and its load

The valve shown in Figure 1.1 is basically a 4-way spool valve. The moving body of the valve is called “spool”, and the part in which the spool moves, and which contains ports to direct the fluid to right direction is called “bushing” or “sleeve”.

There are four metering ports on the sleeve, two of which, namely source ports, open the pressure source (i.e., high-pressure line) to valve chambers and the other two, namely return ports, open the valve chambers to reservoir/tank (i.e., low-pressure line). In Figure 1.1, source ports are named as PA and PB each of which opens pressure source to chamber A and B, respectively. Similarly, the return ports are named as AT and BT, which open the valve chambers A and B to tank, respectively. This naming convention is used for metering ports throughout the thesis.

As the spool moves to $+x_1$ direction, PA is opened, and AT is closed. So, chamber A is opened to high pressure line to increase the chamber pressure p_1. On the other hand, PB is closed and BT is opened too. Obviously, this opens chamber B to low pressure line to decrease the chamber pressure B. As a result, a pressure difference between the two sides of the load occurs, which causes a net force to happen on the load towards $+x_2$ direction. The resulting force moves the load, but movement speed is limited by the flow rate through the metering ports. This means that by controlling the openings of the ports, i.e., the position of the spool, the velocity of load is controlled with the configuration shown in Figure 1.1.

If the spool is moved towards $-x_1$, the ports which are closed before open, chambers A and B are opened to low- and high-pressure lines, respectively, and the force on the load occurs in the $-x_2$ direction. So, the motion of the load is controlled bidirectionally by moving the spool to different directions.

In practical proportional valves, one end of spool is connected to an actuator, which is usually a force motor or a proportional solenoid. Electronically actuated valves benefit from the advantages of both electronics (easier signal generation and transmission) and hydraulics (high power to weight ratio). That is why the servovalves are referred to with the adjective “electrohydraulic”. The other end of

the spool is connected to a position transducer. This way a closed loop system is obtained to control the position of the spool.

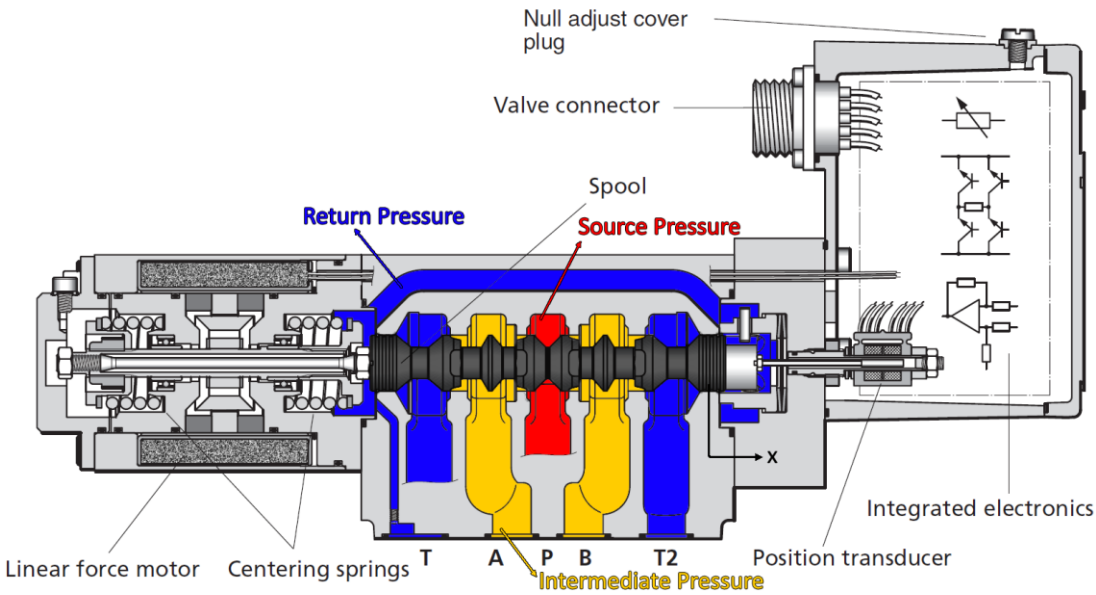

Figure 1.2 – Moog D634-P series single stage servovalve [2]

A commercial example to proportional valves, produced by the company Moog, is given in Figure 1.2. It has a linear force motor as actuator, a position transducer and integrated electronic to close the position control loop of the spool and provide proper input signal to actuator.

The actuator of a single stage servovalve must be chosen so it is strong enough to overcome the "Bernoulli force" which is caused by the flowing fluid through the ports of the valve and defined by the equation (1.1) [2] [8];

$$F = \rho Q V \cos 69° \tag{1.1}$$

where ρ, Q and V are fluid density, volumetric flow rate and flow velocity at the metering port, respectively, while the "69º" is the angle with which the flow leaves the metering port for rectangular port configuration [8] (More on derivation of the Bernoulli force can be found in Section 2.3). Note that equation (1.1) gives the force in only one valve chamber. Since a 4-way spool valve has two chambers, the

resulting axial force on a servovalve spool is twice of that. Obviously, the more rated flow a valve has, the greater the Bernoulli force it is subjected to. So, its actuator must be stronger (i.e., larger in size) to overcome this force. When the actuator is larger, it draws more current, so the battery or power supply must be larger too. That is also the case for all the integrated electronics which are used to control the actuator.

For mobile applications, such as military or aerospace applications, size may matter a lot. Apart from space limitations, bigger components mean higher mass and inductance, i.e., worse dynamic performance. The remedy, which was found for these problems, is to use a pilot stage between the actuator and main stage (i.e., the spool valve) to amplify the power available to move the spool. The valve created this way is called a "double stage servovalve".

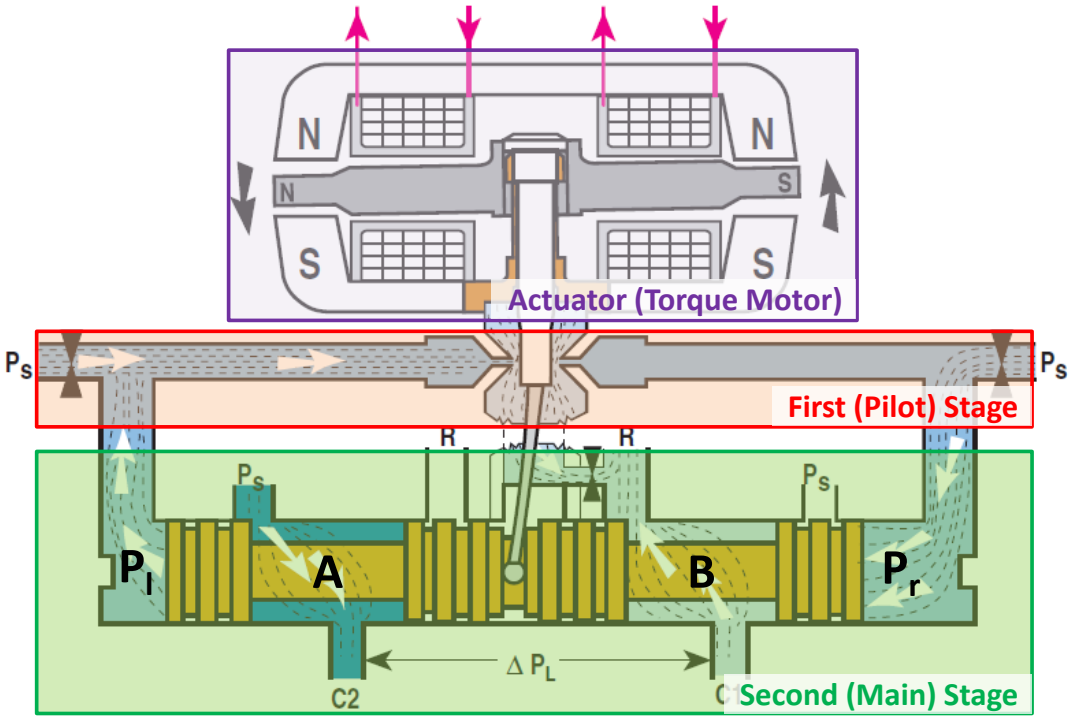

Figure 1.3 – Cross section view of a double stage nozzle-flapper servovalve [4]

Figure 1.3 shows a schematic view of a typical double stage nozzle-flapper servovalve. Its operating principle is as follows;

When current is applied to the torque motor, it rotates the armature due to the magnetic field, let's say counterclockwise in Figure 1.3. This rotation makes the flapper to restrict the fluid flow from the nozzle at the right side of the figure, which causes the pressure "P_r" to increase and "P_l" to decrease. The pressure difference between two outer faces of the spool causes it to translate to left. So, the valve chamber A is opened to pressure port, and B is opened to the reservoir. Thus, the fluid can flow from the pressure source to chamber A, then to chamber B, and then return to reservoir. As the spool moves, it causes the cantilever feedback spring to bend, resulting in a torque on the flapper in the opposite direction to the one applied by the torque motor. This restoring torque retracts the flapper towards its original position until P_r and P_l are the same, i.e., there is no pressure difference between the outer faces of spool. At that point spool stops and a flow rate proportional to the input current is obtained. By changing the sign of the current input, the spool can be moved in opposite direction, making bidirectional flow control possible.

The purpose of the nozzle-flapper valve as the first stage is to amplify the power available to control the flow through the second (main) stage. The electrical input power, which is at an order of magnitude of 0.1 W, is amplified 100 times to 10 W at the first stage. It is then amplified again at the main stage to around 10 kW of hydraulic output power [3]. So it works similar to relays in electronic circuits, controlling a high power with a low power input.

Although the main stage of a servovalve is always a spool valve, the pilot stage may be jet-pipe valve [4], nozzle-flapper valve [5] or again spool valve [6] especially in three stage servovalves which amplifies the power output a further 100 times, compared to two stage servovalves. Among these alternatives, study in this thesis focuses on double stage nozzle-flapper mechanical feedback servovalves, since it is the most common type in aerospace applications.

This section as an introduction to the thesis is included to give brief background information to reader on servovalves. For further information on basics of

servovalves one may refer to numerous resources in literature, such as the textbooks given in [2], [7] and [8].

1.2. Motivation Behind This Study

After the first patent was granted for a two stage servovalve in 1949 [9], servovalve technology matured quickly. Several patents for different designs were granted between late 50's and early 60's (e.g. pressure feedback servovalve [10], [11] and flow rate feedback servovalve [12]). Among these the patent for a mechanical feedback flow control double stage servovalve utilizing a double nozzle-flapper valve for piloting was granted in 1962 [13], which would soon become a de facto standard for aerospace and military applications.

After late 60's, the main structure of double stage servovalves remained unchanged. It was only the developments in smart materials in 2000's that led to the attempts to change the electronic portion (i.e., actuator) of electrohydraulic servovalves. Piezoelectric [14] and magnetostrictive [15] materials seemed as a potential replacement to torque motor as the valve's actuator due to their superior dynamic performance. But the high hysteresis characteristic of smart materials (~%20) makes them unusable in high precision position control systems. For the hydraulic portion, every component stays the way they were in Moog's patent in 1962.

With this maturity in the field, leading companies in the market established their standard commercial servovalve models and customers must select one from their catalogues with a little room for customization. But due to increasing performance requirements especially in military field, custom tailored products are becoming more and more appealing. As the founder of Alibaba.com, Jack Ma said in a conference, "*world is shifting from standardization to personalization*" [16].

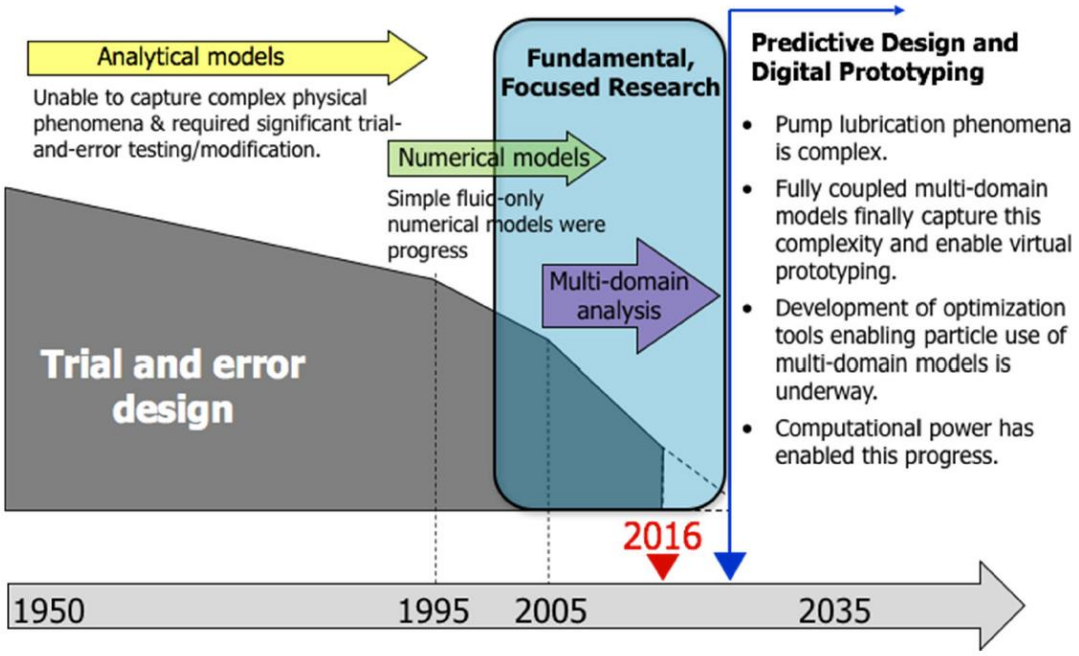

Figure 1.4 – Direction of hydraulic component design [17]

Figure 1.4 is taken from an article on innovations for hydraulic pumps, but it applies to valves as well. As it is implied in the figure, developments in numerical computation models made much faster research and design possible. Although multi-domain analyses are not used for this study, numerical computations are utilized to update all the flow equations to get more accurate models. The main aim is to achieve an accurate overall servovalve model by combining the models for each component. This model will take the effects of a wide range of parameters on servovalve performance into account, like the variations in geometric dimensions or fluid properties, making it possible to design custom servovalves rapidly.

1.3. Objectives of the Thesis

A double stage servovalve consists of three sub-components;

1. An actuator to drive the valve – typically a torque motor

2. A piloting (first) stage to amplify the power available to control the main flow – a nozzle-flapper valve in this study
3. The main (second) stage to direct the main flow and control its flow rate – i.e., a spool valve

In this thesis only the hydraulic aspects of a servovalve will be studied, i.e., only the first and second stages are the main subjects of this thesis. The actuator will not be studied.

At first, a deeper understanding on the servovalves will be gained by examining the existing analytical relations and CFD analyses. Then a complete servovalve model will be created after verification of results obtained using CFD analyses. Finally, a case study will be conducted using this model, by interpreting the overall requirements on a servovalve, determining the requirements on each sub-component and making a tolerance analysis for geometric dimensions according to the particular requirements.

1.4. Literature Survey

Since servovalve designs were matured back in 60's and basic relations defining their performance are well established, textbooks on fluid power control usually dedicate at least a chapter to them. So, the natural starting point to learn about servovalves is these textbooks.

Among these textbooks, one particular book is considered as the holy book of fluid power control and frequently referred to in publications on this field, namely Hydraulic Control Systems by Herbert Merritt, published in 1967 [7]. Both nozzle-flapper and spool valves are examined in the book separately and all the basic equations which define their characteristics are given. Especially the sections on spool valves give extensive information on characteristics of spool valves, studying the forces they are exposed to and the effects of geometry on their performance.

There is also an informative chapter dedicated to servovalves where both static and dynamic performances of servovalves were discussed.

Another important reference is the book Fluid Power Control by Blackburn, Reethof and Shearer published back in 1960 [2], to which Merritt himself refers to in Hydraulic Control Systems. There are heavy discussions on control valve configurations and their performance characteristics in this book too. There is also a chapter on electrohydraulic actuation which discusses two stage servovalves, but since servovalves still had some way to go in 1960, the information here is not as mature as it is in ref. [7].

The book by W. Anderson, Controlling Electrohydraulic Systems (1988) is another notable reference [18]. The basics of spool and nozzle-flapper valves are discussed again but the book is more involved with application of control theory on fluid power control.

A more recent textbook on the field is Fluid Power Engineering by M. Rabie, published in 2009 [19]. There is a whole chapter dedicated on modeling and simulation of electrohydraulic systems, which is of interest to this thesis.

The second textbook reference from 2009 is the book by J. Watton, Fundamentals of Fluid Power Control. The basic discussions appear here again but focus is more on system dynamics and application of the simulation models.

Apart from textbooks, there are also very useful research and conference papers in literature on modeling of servovalves. A series of papers published in 1988-89 written by J. Lin and A. Akers studied nozzle-flapper modeling and dynamics. Authors tried to predict both static and dynamic performance of a nozzle-flapper valve in the first of these papers, using a linear model [20]. The results were compared to experiments, as well as to the older predictions given in [7] and [21]. The same study was issued again later as a journal paper [22]. Then the authors

performed the same analysis using nonlinear models in [23] and obtained similar results to [20] and [22].

Aung et al. investigated nozzle-flapper valves in terms of flow forces and energy loss characteristics [24]. CFD analyses were made on different structures and null clearances. Results for energy loss were compared against experimental results. Results for flow force proved that the traditional flow force models are valid especially for smaller null clearances than one tenth of nozzle diameter.

Zhu and Fei proposed a new criterion for designing a nozzle-flapper valve [25]. Traditional design criterion was criticized since its only objective is to maximize the null control pressure. New performance characteristics for nozzle-flapper valve were defined in the paper, namely symmetry, linearity and sensitivity of control pressure, and the new design was made by improving symmetry and linearity but deteriorating sensitivity. The work is built upon the existing flow models for nozzle-flapper valves, new performance characteristics were defined by manipulating the existing mathematical relations and no CFD analyses or experiments were conducted.

Li et al. deduced mathematical models for flow force and forced vibration [26]. The models were validated with both CFD analyses and experiments. Natural frequency of armature assembly was measured and effects of inlet pressure fluctuation near that frequency were investigated. The work is beneficial for understanding the forces on flapper and behavior of nozzle-flapper valves under these forces.

Kılıç et al. studied the effects of increasing the pressure at nozzle outlet by introducing a drain orifice before the flow is directed to reservoir after leaving the nozzle [27]. Existing mathematical relations were used to model the flows. The cases in which the outlet orifice present or not were compared in dimensionless load pressure vs. load flow rate graphs. Results showed that by presenting a drain orifice, variations in load pressure decreases as the load flow rate changes. A similar analysis on drain orifice was also done by Watton previously [28].

Like the papers written on nozzle-flapper valves by Lin and Akers, A. Ellman et al. have written a series of papers on modeling of spool valves. In [29] and [30], flow in a short annulus, which is encountered in closed ports of spool valves, and leakage flow of servovalves were modeled, respectively. In these works, flow models consist of constants which must be identified according to the characteristic flow and pressure curves of the valve that is to be modeled. This means that models developed in these works can only be used to model an existing valve, for the purpose of predict its performance or design a controller for it. In [31] pressure gain characteristic of servovalves is studied. Again, a flow model for spool valve ports which is based on system identification was used. Study of relation between the pressure gain and internal leakage and influence of internal leakage on system damping in the work are particularly useful.

Eryılmaz and Wilson conducted a similar work on modeling of servovalves [32]. Their model also relies on predetermined valve data. Model's parameters must be identified according to this data, so the purpose is to model an existing valve for control purposes rather than designing it. Although the model is valid for entire spool position range, it is not valid for the valves which are not zero lapped.

Another work to include leakage flow in servovalve model for control purposes was accomplished by Feki and Richard [33]. The study is very similar to Eryılmaz and Wilsons's [32], even the experimental data to test the model's performance was provided by Dr. Eryılmaz. Their model also deals with zero lapped valves and all ports must be symmetrical, but they underlined that the model can be extended to other lapping conditions.

Mookherjee et al. published a valuable study on design of direct drive valves (DDV) [34]. In the paper, a model for the flows through spool valve control ports was developed based on analytical relations and boundary layer analysis. Since they approached the subject from a design point of view, the model's parameters are all physical quantities. It can handle a spool valve design with different lapping

conditions for all ports and is valid for entire spool position range. Hence the model can be used for tolerance analysis of geometric dimensions of a spool valve.

In [35] and [36] Gordic et al. modeled a double stage servovalve and studied the leakage flow in spool valves, respectively. In these works, they based their spool valve flow model on the study given in [34]. But as opposed to [34], they used a constant discharge coefficient in their model. They estimated a valve's load pressure and internal leakage with respect to spool position using their model and compared the results to experiments and output of other models from [31] and [32]. Estimation performance of the model seems reasonable, but the implicit equations making up the model make it difficult to use it in transient simulations.

Nakada and Ikebe measured the unsteady axial flow force on spool valve and compared the result to the theoretical model [37]. The theoretical model that they have used was based on the momentum theory Ikebe and Ouchi had derived [38]. It was concluded in the paper that axial flow force on the spool increases at high frequency region due to unsteady components, and the chamber volume of spool valve has a large influence on this increase.

Another class of academic works particularly useful to the present study is the ones studying the discharge characteristics of orifices. Since orifices have a very central role of a double stage servovalve's function, their accurate modeling is crucial in simulation of servovalves. There are countless papers studying the flow through orifices in the literature. But since discharge coefficient is very dependent of geometry, focusing on particular works on geometries that can be found in servovalves makes more sense.

Discharge through the fixed orifice geometry in the double stage servovalve was studied before [39]. In the paper, both numerical analyses and experiments were conducted, and results were compared. In numerical analyses, different turbulence models were used to find out which model provides most accurate results comparing to experimental data. Paper's contributions are directly related to the present study.

Pan et al. analyzed discharge characteristics of a spool valve [40]. The radial clearance is totally disregarded in the paper and there are some ambiguities in numerical analysis section, e.g. no word was mentioned on the turbulence modeling. Moreover, the experiments were done using an equipment to represent the orifice in spool valves, but not an actual spool valve. Nevertheless, the authors claimed that results from simulations in excellent agreement with the experiments.

Posa et al. conducted a similar study on discharge characteristics of spool valves, by criticizing Reynolds Averaged Navier Stokes (RANS) methods on turbulence modeling and using Direct Numerical Solution (DNS) instead [41]. Although the authors did not conduct any experiments to back their conclusions, they claimed that the discharge coefficient in a spool valve can be as high as 0.77 as opposed to ref. [40] which claimed it never reaches 0.7.

Valdes et al. studied the modelling of flow coefficients in different hydraulic restriction geometries using CFD simulations [42] [43]. These geometries do not include a spool valve, but the papers are still useful for gaining some insight on the job.

Mondal et al. studied the leakage flow through a spool valve by using an indigenous CFD code to estimate the port lappings and radial clearances of different valves, comparing the leakage flow and load pressure data obtained by experiments [44].

1.5. Outline of the Thesis

This study is focused on modeling of a double stage nozzle-flapper type electro-hydraulic servovalve in detail, including the nonlinearities known to exist in servovalves. The purpose of obtaining such a detailed model is to use it in the tolerance analysis of geometric dimensions to enable rapid custom-tailored product development. So the rest of the chapters are organized as follows;

In Chapter 2, the current state of art of modeling a double stage servovalves is summarized. First a very general overview of a double stage servovalve is given. Then modeling of the first and second stages is gone through. At the end the limitations and assumptions of existing relations are underlined.

In Chapter 3, existing relations given in Chapter 2 for first and second stages are modified to eliminate the limitations they possess. CFD analyses are utilized to improve the accuracy of flow rate – pressure drop relations wherever possible and they are validated against experimental data.

In Chapter 4, all the mathematical models are integrated together to complete the double stage nozzle flapper servovalve model. In the model, the first and second stages are handled in detail, while the actuator part is barely more than a transfer function just to reflect the effects of nonlinearities an actuator may have. The model is then tested using the known parameters of a commercial servovalve.

Chapter 5 is dedicated to summary and conclusions.

CHAPTER 2

CURRENT STATE OF THE ART OF MODELING DOUBLE STAGE NOZZLE-FLAPPER SERVOVALVES

2.1. Overview of Servovalve Physical Model

Working principle of a double stage mechanical feedback nozzle-flapper servovalve with a torque motor as the actuator is explained in Section 1.1. A simple block diagram representation of Figure 1.3 is given in Figure 2.1.

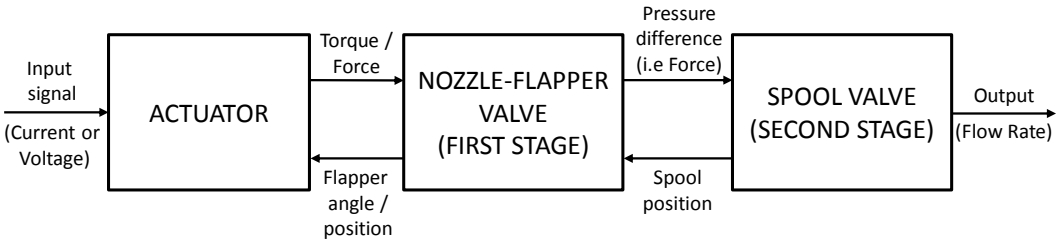

Figure 2.1 – Block diagram representation of double stage servovalve physical model

In Figure 2.1, three components of a double stage servovalve as listed in Section 1.3 are given as sub-system block and relation between them are shown in servovalve system level. Among these sub-systems, actuator will not be studied in detail in the scope of this thesis, but the first and second stages will be studied as detailed as possible. In what follows, existing mathematical relations for modeling the latter two components are given to constitute a basis for a more detailed model. For the modeling information given in this chapter the textbooks [7], [18] and [19] were referred to.

2.2. Nozzle-Flapper Valve Model

Figure 2.2 shows a schematic view of a double stage nozzle-flapper servovalve.

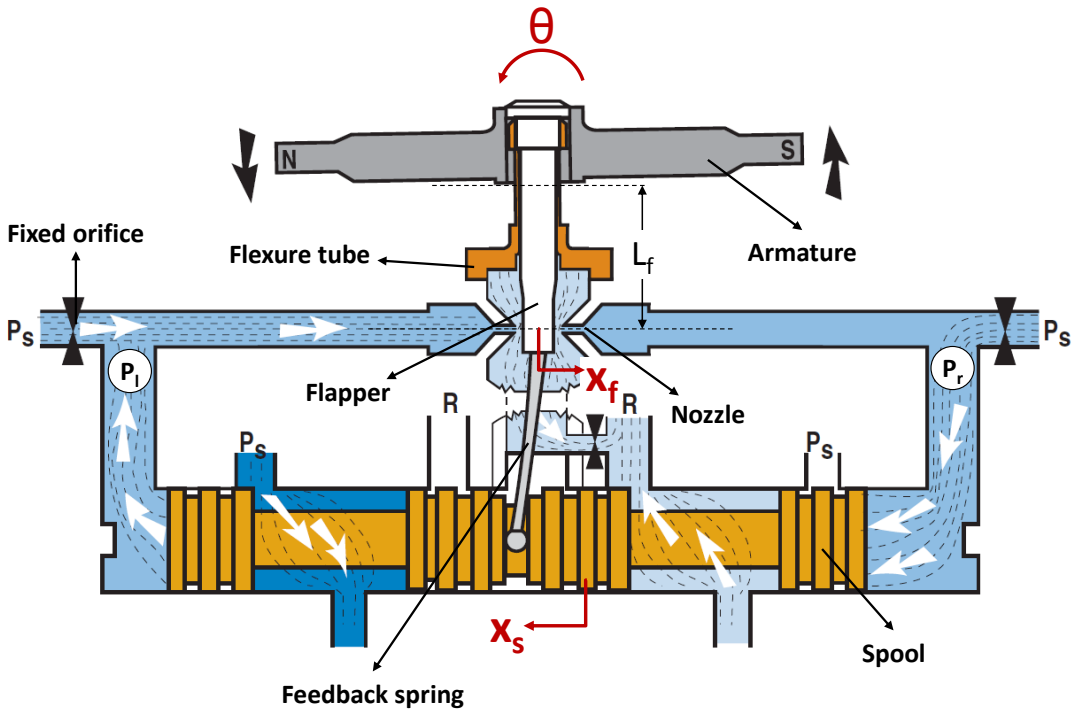

Figure 2.2 – Parts of a double stage nozzle-flapper servovalve [5]

In the configuration show in Figure 2.2, input to the first stage is the torque created by the torque motor. As a response to this input, armature rotates causing the flapper to rotate too. Equation of motion for this rotation is given in equation (2.1).

$$T_{tm} + T_n = J_{FS}\ddot{\theta} + c_{FS}\dot{\theta} + \left(k_{ft} + k_{fb}L_s^2\right)\theta + k_{fb}L_s x_s \tag{2.1}$$

The external torque acting on the flapper is the combination of the torques from torque motor (T_{tm}) and nozzles (T_n) caused by the momentum of the fluid coming out. The inertia term J_{FS} is the inertia of all rotating parts in the flapper assembly, while the damping term c_{FS} is the combination of structural, material and hydraulic damping acting on the flapper. Since these contributions to damping are typically very small compared to mass and stiffness [45], the damping ratio of the nozzle-flapper valve is so small [26] that sometimes the damping term in equation (2.1) is

totally neglected [7]. The stiffness coefficients k_{fb} and k_{ft} are the stiffness values of feedback spring and flexure tube, respectively.

Using the parameters shown in Figure 2.3, the torque on the flapper exerted by the fluid jets coming out of the nozzles can be expressed as;

$$T_n = (F_l - F_r)L_f \tag{2.2}$$

where F_l and F_r are the forces applied on the flapper by the fluid jets. These forces are given by [7];

$$F_l = A_n\left(P_l + \frac{1}{2}\rho u_l^2\right) \tag{2.3}$$

$$F_r = A_n\left(P_r + \frac{1}{2}\rho u_r^2\right) \tag{2.4}$$

In equations (2.3) and (2.4) A_n is the exit area of a nozzle, while u_l and u_r are the x-components of velocities of fluid jets from corresponding nozzles;

$$u_l = \frac{Q_l}{A_n} = \frac{4Q_l}{\pi D_n^2} \tag{2.5}$$

$$u_r = \frac{Q_r}{A_n} = \frac{4Q_r}{\pi D_n^2} \tag{2.6}$$

Q_l and Q_r are the flow rates at the exits of nozzles and calculated using the orifice formula assuming zero pressure outside the nozzles;

$$Q_l = C_{D,n}\pi D_n(x_0 + x_f)\sqrt{\frac{2}{\rho}P_l} \tag{2.7}$$

$$Q_r = C_{D,n}\pi D_n(x_0 - x_f)\sqrt{\frac{2}{\rho}P_r} \tag{2.8}$$

where $\pi D_n(x_0 \pm x_f)$ is called the "curtain area". A detailed sectional view of double nozzle-flapper valve used in two stage servovalves is given in Figure 2.3.

Note that the parameters D_c, L_e, α and β in Figure 2.3 might have an influence on the flow rate and force expressions too, but for the basic theoretical analysis that can be found in classical textbooks, effects of such geometrical details are usually not examined.

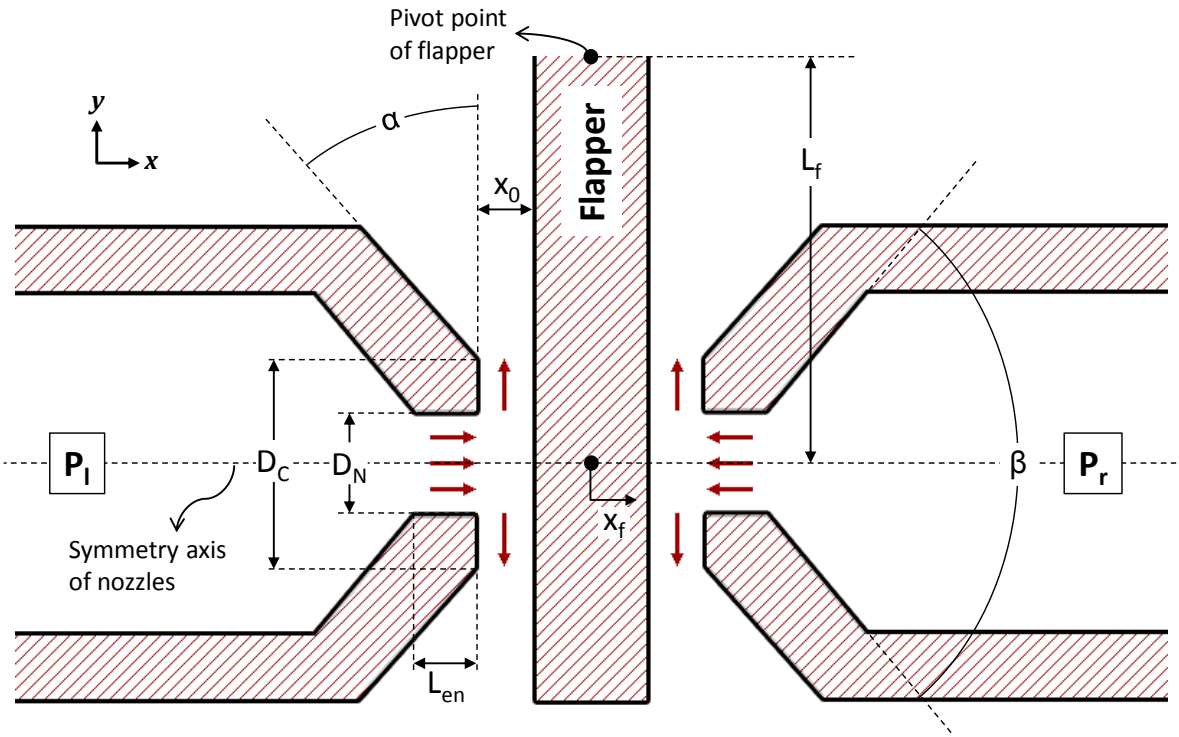

Figure 2.3 – Geometric dimensions of a nozzle-flapper valve

Next step should be to find the definitions for P_l and P_r. To find P_l and P_r continuity equation in the control volume limited between the nozzle exits, fixed orifices and the spool outer walls and corresponding fixed orifices (refer to Figure 2.2) can be evaluated. Assuming the fluid is incompressible;

$$Q_{in} = Q_{out} \tag{2.9}$$

For the left branch of the first stage it becomes;

$$C_{D,f}\frac{\pi D_f^2}{4}\sqrt{\frac{2}{\rho}(P_s - P_l)} + A_s\dot{x}_s = C_{D,n}\pi D_n(x_0 + x_f)\sqrt{\frac{2}{\rho}P_l} \tag{2.10}$$

And for the right branch;

$$C_{D,f}\frac{\pi D_F^2}{4}\sqrt{\frac{2}{\rho}(P_s - P_r)} = C_{D,n}\pi D_N(x_0 - x_f)\sqrt{\frac{2}{\rho}P_r} + A_s\dot{x}_s \tag{2.11}$$

The MATLAB code given in Appendix A used to obtain the definitions of P_l and P_r using equations (2.11) and (2.12), substitute equations (2.3) to (2.12) into equation (2.2) and linearize it around $x_f = \dot{x}_s = 0$;

$$\Delta T_n = \frac{\partial T_n}{\partial \theta}\Big|_{\substack{\theta=0 \\ \dot{x}_s=0}} \theta + \frac{\partial T_n}{\partial \dot{x}_s}\Big|_{\substack{\theta=0 \\ \dot{x}_s=0}} \dot{x}_s = -k_n\theta + c_n\dot{x}_s \tag{2.12}$$

where

$$k_n = \frac{16\pi C_{D,f}^2 C_{D,n}^2 D_f^4 L_f^2 P_s x_0 \left(D_n^4 - C_{D,f}^2 D_f^4\right)}{\left(C_{D,f}^2 D_f^4 + 16 C_{D,n}^2 D_n^2 x_0^2\right)^2} \tag{2.13}$$

and

$$c_n = \frac{2\pi C_{D,f} C_{D,n} D_f^2 D_n D_s^2 L_f x_0 \left(16 C_{D,n}^2 x_0^2 + D_n^2\right)\sqrt{2\rho P_s}}{\left(C_{D,f}^2 D_f^4 + 16 C_{D,n}^2 D_n^2 x_0^2\right)^{1.5}} \tag{2.14}$$

By substituting equation (2.12) into (2.1) with $x_f = L_f\theta$ and rearranging, one gets

$$T_{tm} = J_{FS}\ddot{\theta} + c_{FS}\dot{\theta} + \left(k_{ft} + k_n + L_s^2 k_{fb}\right)\theta + k_{fb}L_s x_s - c_n\dot{x}_s \tag{2.15}$$

Theoretical analysis in this section is made assuming symmetrical nozzles and fixed orifices on each side for simplicity. But for a geometrical tolerance analysis no symmetrical dimensions should be assumed, which will be the case in the following chapters.

2.3. Spool Valve Model

In Figure 2.2 spool is driven by the pressure difference created on both of its ends by the movement of flapper. So the equation of motion for the spool is given in

$$A_s(P_r - P_l) + F_B = m_s\ddot{x}_s + c_s\dot{x}_s + k_{fb}(x_s + L_s\theta) \tag{2.16}$$

L_s is the distance between the pivot point of the flapper and the spool-end of the feedback spring as shown in Figure 2.4.

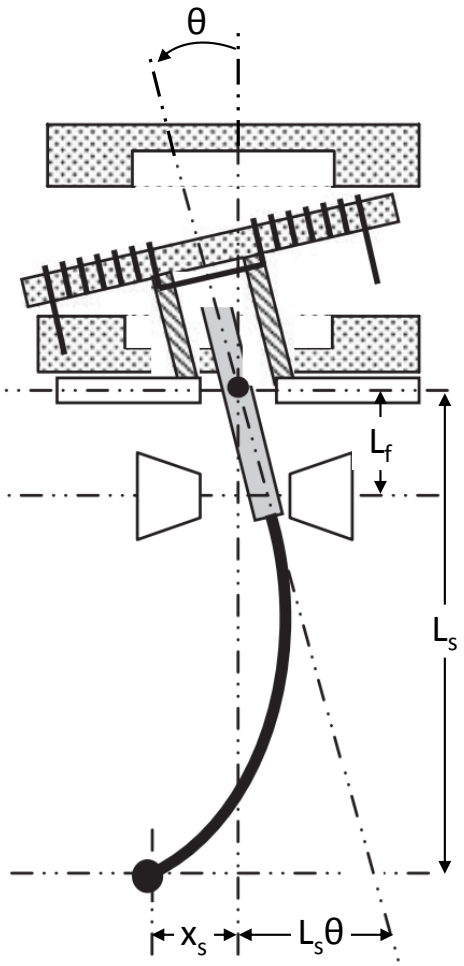

Figure 2.4 – Exaggerated view of first stage when both spool and flapper is moved [9]

The term F_B in equation (2.16) denotes the Bernoulli force occurring on the spool due to fluid flow [7]. It is denoted as F_x in Figure 2.5.

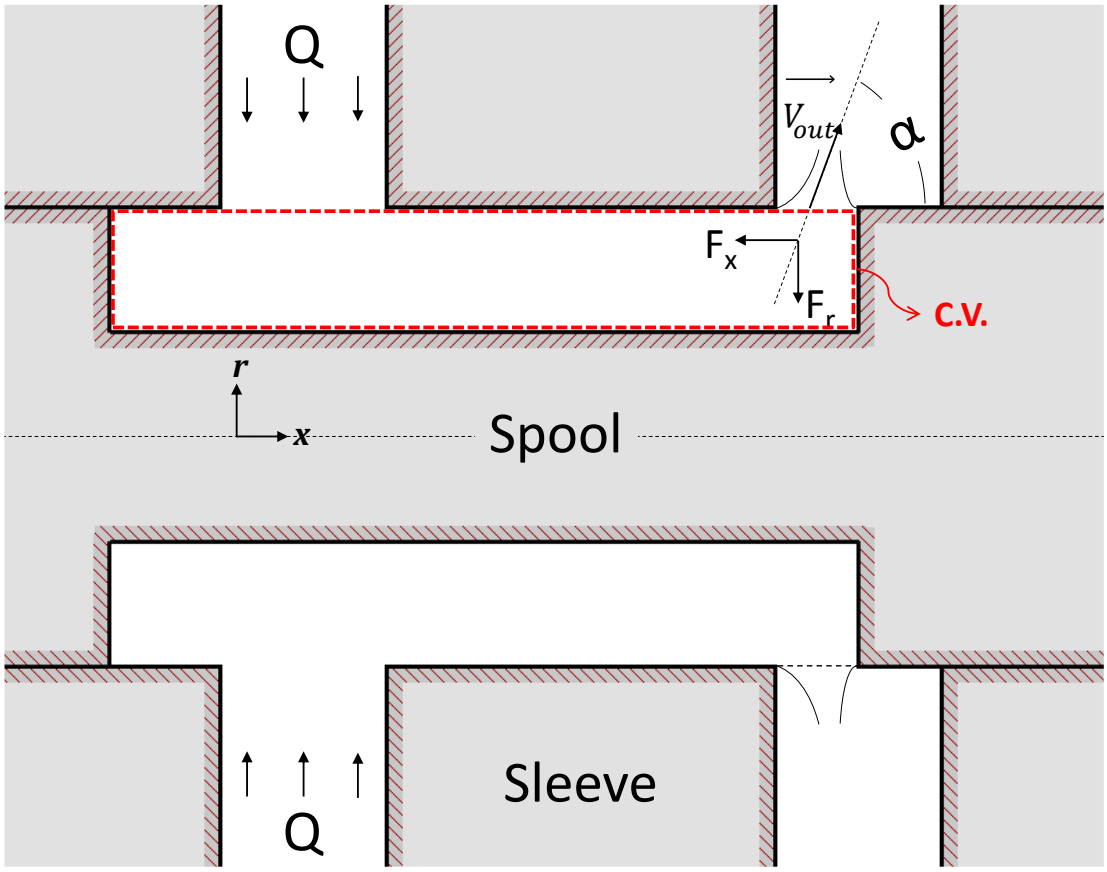

Figure 2.5 – Bernoulli force on the spool

The Bernoulli force on a spool under a certain flow rate can be found applying Reynolds' Transport Theorem for momentum on the control volume shown in Figure 2.5.

$$\vec{R} - P_{in}A_{in}\hat{r} - P_{out}A_{out}\hat{r} = \int_{A_{in}} \rho\vec{V}_{in}(\vec{V}_{in}\cdot\hat{n}_{in})dA + \int_{A_{out}} \rho\vec{V}_{out}(\vec{V}_{out}\cdot\hat{n}_{out})dA \tag{2.17}$$

In equation (2.17) $\vec{R}$ is the force exerted on the control volume by the walls. It is more convenient to express relations about servovalve in terms of flow rate rather than velocity, since flow rate is the output of a valve. The velocity V_{out} in Figure 2.5 – Bernoulli force on the spool can be related to flow rate as

$$V_{out} \sin\alpha = \frac{Q}{A_{out}} \rightarrow V_{out} = \frac{Q}{A_{out} \sin\alpha} \tag{2.18}$$

Since only the r-component of V_{out} contributes to the flow rate, it is multiplied by $\sin\alpha$ in equation (2.18). Similarly V_{in} can be related to flow rate as

$$V_{in} = \frac{Q}{A_{in}} \tag{2.19}$$

The unit vectors $\hat{n}_{in}$ and $\hat{n}_{out}$ in equation (2.17) are the normal vectors of the inlet and outlet of the control volume, respectively, and both of them are equal to $\hat{r}$. So equation (2.17) can be rewritten as

$$\begin{aligned} \vec{R} - P_{in}A_{in}\hat{r} - P_{out}A_{out}\hat{r} &= \int_{A_{in}} \rho \frac{Q}{A_{in}}(-\hat{r})\left[\frac{Q}{A_{in}}(-\hat{r})\cdot\hat{r}\right]dA \\ &+ \int_{A_{out}} \rho \frac{Q}{A_{out}\sin\alpha}(\hat{r}\sin\alpha \\ &+ \hat{\imath}\cos\alpha)\left[\frac{Q}{A_{out}\sin\alpha}(\hat{r}\sin\alpha + \hat{\imath}\cos\alpha)\cdot\hat{r}\right]dA \end{aligned} \tag{2.20}$$

If solved for only the x-component of $\vec{R}$;

$$R_x = \rho \frac{Q^2}{A_{out}} \cot\alpha \tag{2.21}$$

Since $\vec{R}$ is the force applied by the walls on the control volume, the force applied on the spool by the flow becomes

$$F_x = -R_x = -\rho \frac{Q^2}{A_{out}} \cot\alpha \tag{2.22}$$

The angle α in equation (2.22) is actually a function of orifice opening at the outlet but known to approach to 69° as the outlet orifice is further opened [7]. To obtain

linear output the outlet ports of the sleeve in servovalves are always manufactured as rectangular slots as shown in Figure 2.6. So, outlet area is actually a rectangular area;

$$A_{out} = wx_s \tag{2.23}$$

where w is the area gradient of all rectengular slots along the periphery. Since there are two chambers in a servovalve the Bernoulli force F_B in equation (2.16) should be twice of F_x in equation (2.22);

$$F_B = -\frac{2\rho Q^2}{wx_s}\cot 69° \cong -\frac{0.77\rho Q^2}{wx_s} \tag{2.24}$$

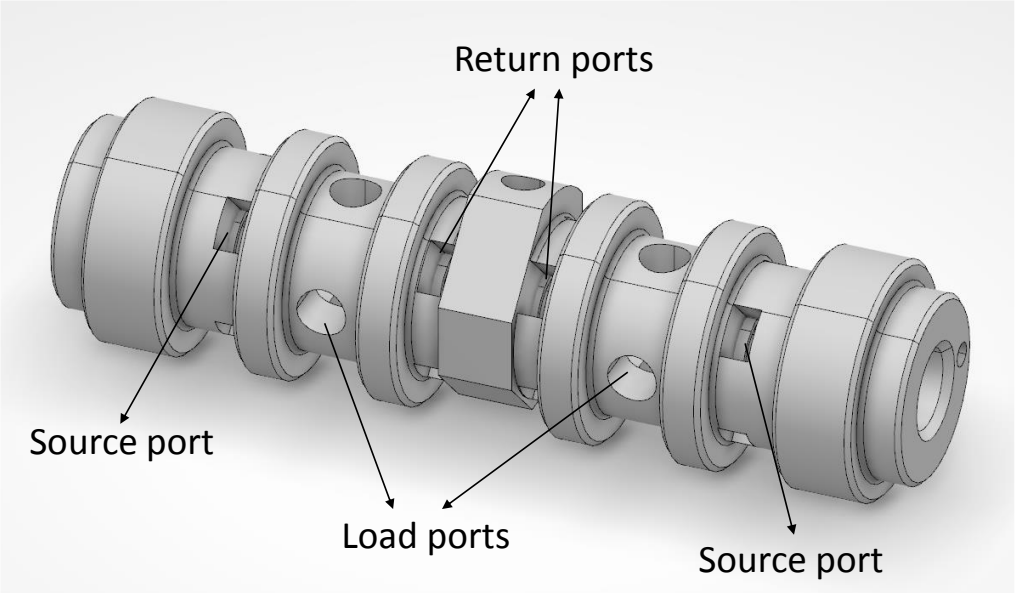

Figure 2.6 – CAD model of a servovalve sleeve

The damping term in equation (2.16) is actually the viscous friction between the spool and sleeve, due to the resistance of the film layer of hydraulic oil in the radial clearance to shear. It can be expressed as

$$c_s = \frac{\pi D_s L_d \mu}{B} \tag{2.25}$$

where L_d is the total length of the sections with largest diameter on the spool (refer to Figure 2.2) [7]. Also replacing x_f with $L_f\theta$ again, equation (2.16) now becomes

$$A_s(P_r - P_l) = m_s\ddot{x}_s + c_s\dot{x}_s + k_{fb}(x_s + L_s\theta) + \frac{0.77\rho Q^2}{wx_s} \tag{2.26}$$

The control ports of a spool valve may assume two different geometrical conditions depending on the spool position: open or closed. So to calculate the flow rate through the any of these ports, appropriate function relating the pressure drop across the port to the flow rate for each geometrical condition must be applied.

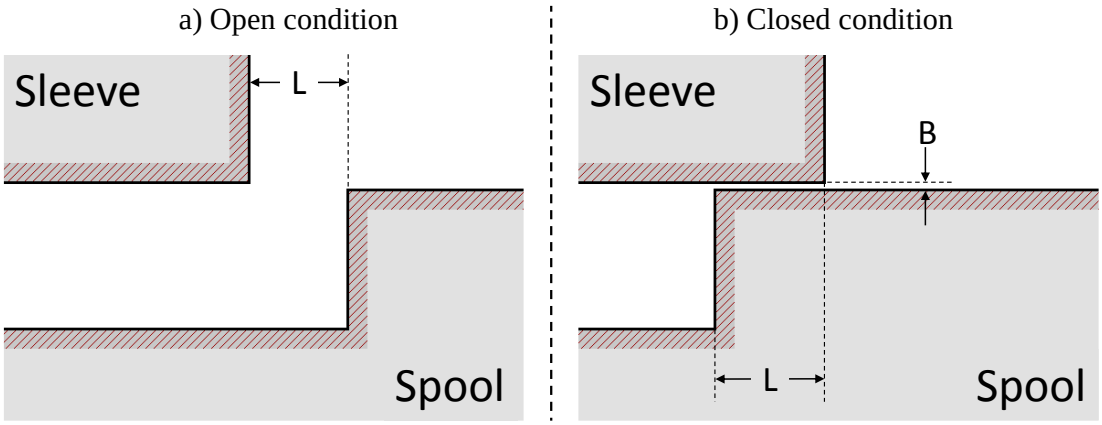

Figure 2.7 – Open and closed conditions of a spool valve control port

Figure 2.7 shows the open and closed conditions that can be encountered during the operation of a spool valve. When the control port is opened, the flow occurs across the orifice created between the sharp edges of spool and sleeve. So the flow rate through such an orifice can be expressed using the standard orifice equation;

$$Q = C_{D,s}wL\sqrt{\frac{2}{\rho}\Delta P} \tag{2.27}$$

w here can be replaced with πD_s if entire periphery is assumed to be open. When the control port is closed, as shown in Figure 2.7b, the working fluid is forced to flow

through the thin gap of radial clearance between the spool and the sleeve. Flow rate in this case is calculated using equation (2.28) [7].

$$Q = \frac{\pi R_s B^3}{6\mu L}\left(1 + \frac{3e^2}{2B^2}\right)\Delta P \tag{2.28}$$

The term $\left(1 + \frac{3e^2}{2B^2}\right)$ in equation (2.28) is used to account for eccentricity between spool and sleeve, where e denotes the distance between their axes as shown in detail in Figure 2.8.

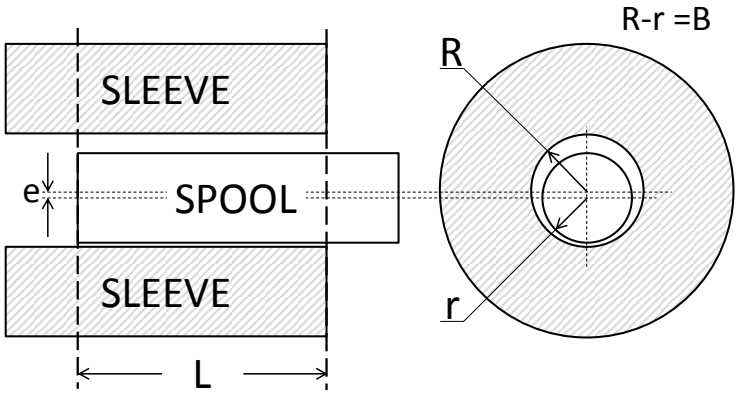

Figure 2.8 – Eccentricity in closed condition

If the all the controlling edges on the spool matches the corresponding edges on the sleeve when the spool is in null position ($x_s = 0$), i.e., the valve is zero lapped as shown in Figure 2.9, then $L = x_s$ for all control ports so L in equation (2.27) can be replaced by x_s.

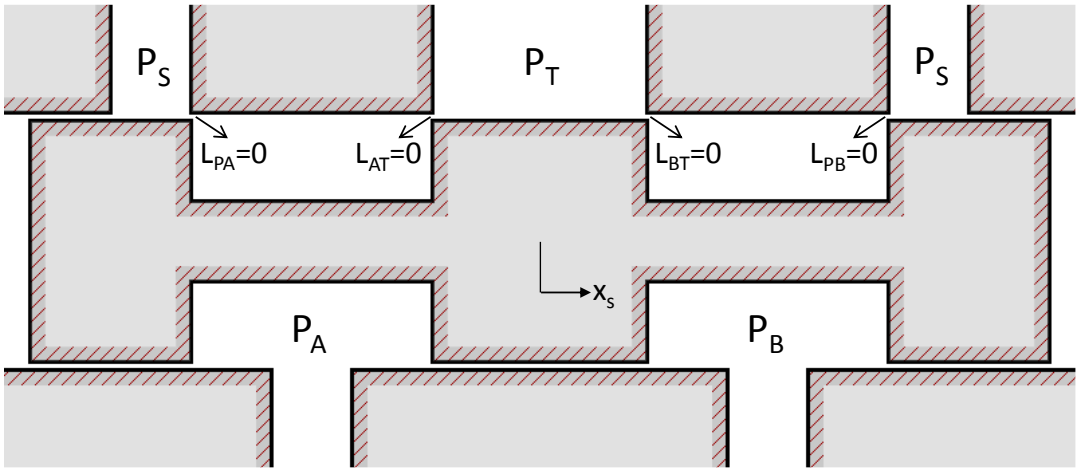

Figure 2.9 – Zero lapped control ports

When the spool in Figure 2.9 is moved a certain amount as shown in Figure 2.10, the fluid is allowed to flow from pressure source to chamber A and from chamber B to reservoir. The rates of these flows can be calculated using equation (2.27);

$$Q_{PB} = C_{D,s} w x_s \sqrt{\frac{2}{\rho}(P_s - P_B)} \tag{2.29}$$

$$Q_{AT} = C_{D,s} \pi D_s x_s \sqrt{\frac{2}{\rho}(P_A - P_T)} \tag{2.30}$$

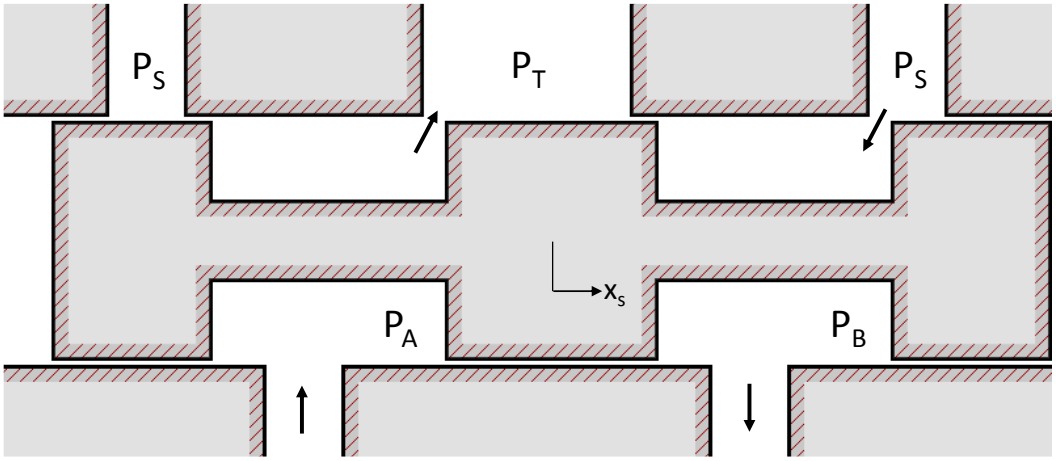

Figure 2.10 – Spool valve in open position

The flow rates at the other control ports can be neglected when compared to open ports, so for continuity Q_{PB} must equal to Q_{AT}. Assuming $P_T = 0$;

$$C_{D,s} w x_s \sqrt{\frac{2}{\rho}(P_s - P_B)} = C_{D,s} w x_s \sqrt{\frac{2}{\rho} P_A}$$

$$P_s = P_B + P_A \tag{2.31}$$

The pressure difference between the load ports is defined as the load pressure.

$$P_L \triangleq P_B - P_A \tag{2.32}$$

Solving equations (2.31) and (2.32) together for P_A;

$$P_A = \frac{P_s - P_L}{2} \tag{2.33}$$

Substituting equation (2.33) into equation (2.30);

$$Q_L = C_{D,s} w x_s \sqrt{\frac{P_S - P_L}{\rho}} \tag{2.34}$$

The flow rate expression given in equation (2.34) is the flow rate through a spool valve and can be substituted into equation (2.26) to get

$$A_s(P_r - P_l) = m_s \ddot{x}_s + c_s \dot{x}_s + \left[0.77 C_{D,s}^2 w (P_s - P_L) + k_{fb}\right] x_s + k_{fb} L_s \theta \tag{2.35}$$

Again, for simplicity all ports are assumed to be zero lapped. But for a geometric tolerance analysis, deviations for lappings must be considered.

Eq. (2.35) may be further expanded by substituting the definitions of P_r and P_l as they are found in Section 2.2. Again the linearized form of the term $A_s(P_r - P_l)$ can be found using the MATLAB code given in Appendix A ($F_c \triangleq A_s(P_r - P_l)$);

$$\Delta F_c = \left.\frac{\partial F_c}{\partial x_f}\right|_{\substack{x_f=0 \\ \dot{x}_s=0}} x_f + \left.\frac{\partial F_c}{\partial \dot{x}_s}\right|_{\substack{x_f=0 \\ \dot{x}_s=0}} \dot{x}_s = k_c x_f - c_c \dot{x}_s \tag{2.36}$$

where

$$k_c = \frac{16\pi C_{D,f}^2 C_{D,n}^2 D_f^4 D_n^2 D_s^2 P_s x_0}{\left(C_{D,f}^2 D_f^4 + 16 C_{D,n}^2 D_n^2 x_0^2\right)^2} \tag{2.37}$$

and

$$c_c = \frac{2\pi C_{D,f} C_{D,n} D_f^2 D_n D_s^4 x_0 \sqrt{2\rho P_s}}{\left(C_{D,f}^2 D_f^4 + 16 C_{D,n}^2 D_n^2 x_0^2\right)^{1.5}} \tag{2.38}$$

By replacing $A_s(P_r - P_l)$ in equation (2.35) with ΔF_c in equation (2.36) with $x_f = L_f\theta$ one finds the final form of the equation of motion for the second stage;

$$\begin{aligned}\left(k_c L_f - k_{fb} L_s\right)\theta = m_s \ddot{x}_s + (c_s + c_c)\dot{x}_s \\ +\left[0.77 C_{D,s}^2 w (P_s - P_L) + k_{fb}\right] x_s\end{aligned} \tag{2.39}$$

Before closure, it would be appropriate to discuss the damping on the spool which is the summation of two components: c_s which is due to shear stress caused by the fluid in the radial clearance and c_c which is due to restriction of fixed orifices against the flow to move the spool. These two components are evaluated for typical parameters given in Table 2.1.

Table 2.1 – Some typical servovalve parameters

Parameter	Definition	Value
$C_{D,f}$	Fixed orifice discharge coefficient	0.7
$C_{D,n}$	Nozzle discharge coefficient	0.6
D_n	Diameter of nozzle exit	200 µm
D_f	Diameter of fixed orifice	200 µm
D_s	Diameter of spool	5 mm
x_0	Null curtain length	30 µm
P_s	Supply pressure	210 bar
ρ	Density of the hydraulic fluid	860 kg/m^3
μ	Viscosity of the hydraulic fluid	0.018 Pa·s
L_d	Damping length of the spool	10 mm
B	Radial clearance	2 µm

From equations (2.25) and (2.38) it is calculated that $c_s = 1.414 \frac{N}{m/s}$ and $c_c = 2410 \frac{N}{m/s}$ with the parameters in Table 2.1. It is apparent that c_c is three order of magnitudes higher than c_s, so it can be concluded that damping caused by the fixed orifices on the spool is without dispute dominant and c_s can be totally omitted in the equations.

2.4. Limitations and Assumptions of the Existing Models

Figure 2.11 shows flow rate vs. curtain length graph of the valve geometry shown in Figure 2.12. In the graph, flow rate results obtained using equation (2.8) and CFD analyses are compared. Numerical values of the parameters used in calculations are given in Table 2.2.

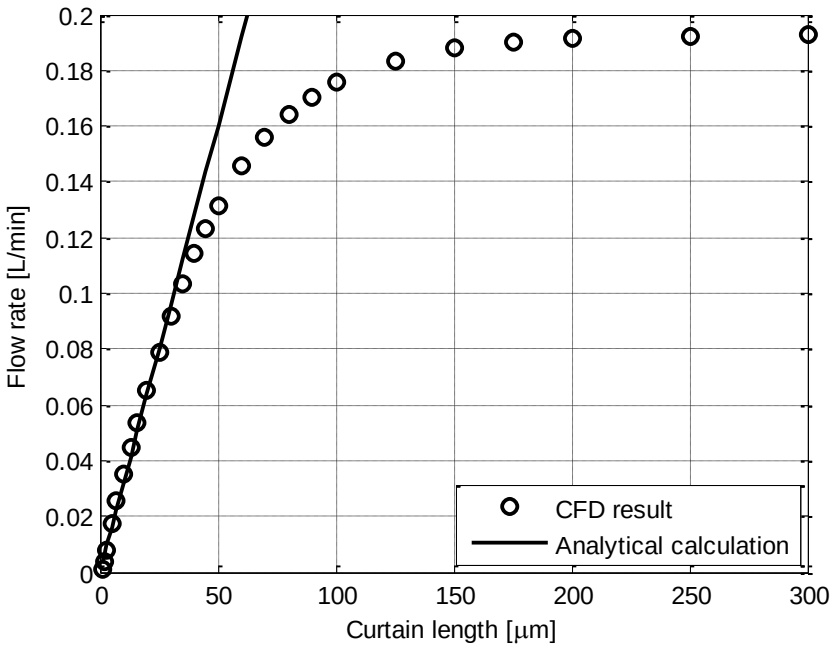

Figure 2.11 – Flow rate vs. curtain length graph of a single nozzle-flapper valve

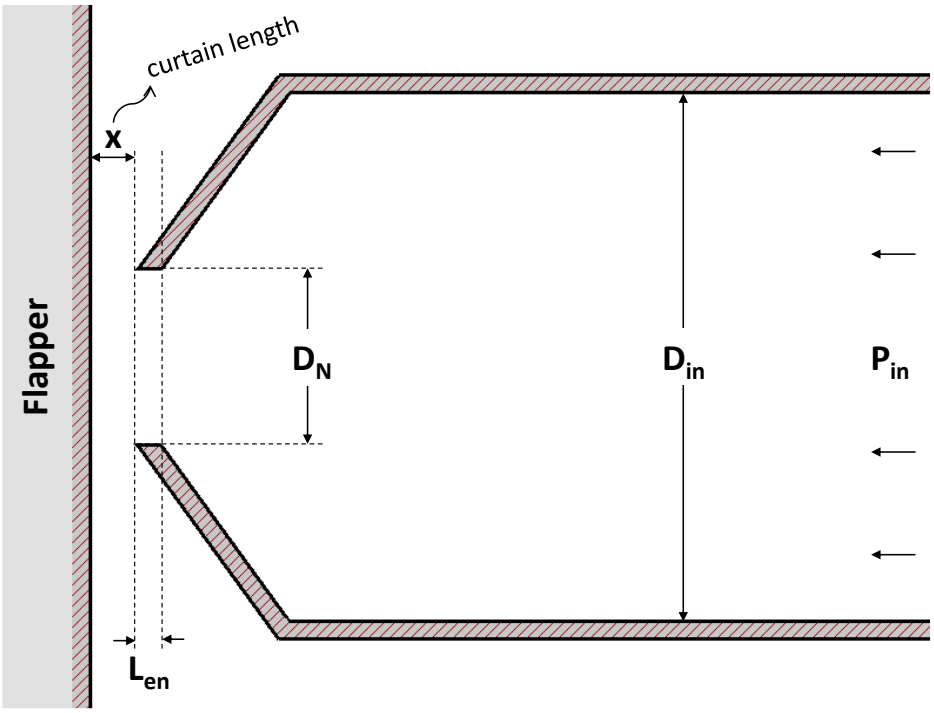

Figure 2.12 – Sample nozzle-flapper valve analysis geometry

Table 2.2 – Numerical values of parameters in Figure 2.12

Parameter	Value	Definition
P_{in}	100 bar	Inlet pressure
D_{in}	1000 µm	Inlet diameter
D_n	200 µm	Nozzle diameter
L_e	10 µm	Nozzle exit length
µ	0.02 Pa·s	Dynamic viscosity of the fluid
ρ	1000 kg/m^3	Mass density of the fluid

As opposed to practical nozzle geometry shown in Figure 2.3, a nozzle geometry closer to ideal case with no curtain diameter ($D_c = 0$) and a small exit length ($L_e = 10\ \mu m$) as shown in Figure 2.12. CFD analyses are done in a 2D axisymmetric domain.

Figure 2.12 shows that even with the ideal geometry, equation (2.8) is valid only within a certain curtain length. When the geometric parameters shown in Figure 2.3 are also taken into account, the region in which the flow rate function is valid should

be known precisely and if necessary the function should be modified for more accurate estimations in a wider range.

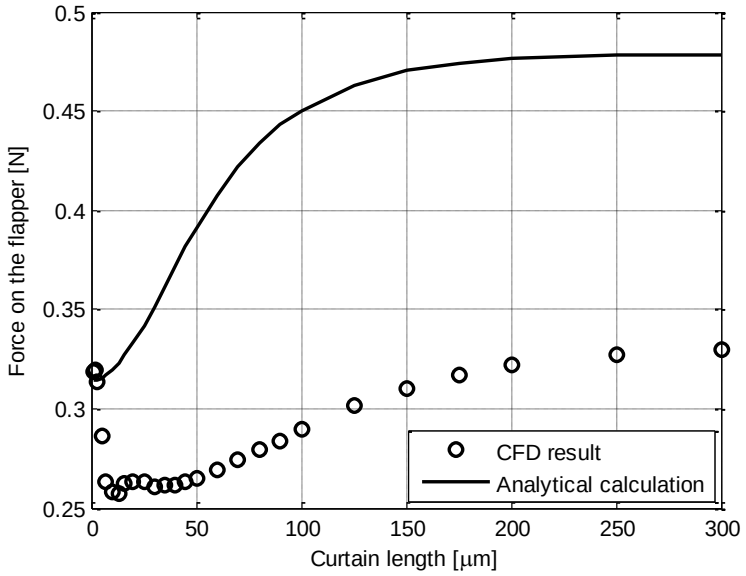

Figure 2.13 – Flapper force vs. curtain length graph of a single nozzle-flapper valve

Figure 2.13 shows the force estimations on the flapper of both CFD analyses and equation (2.4). Flow rate data to be used by equation (2.4) are also taken from CFD analyses. As can be seen with data from CFD analyses, equation (2.4) still overestimates the force on the flapper comparing to CFD results. This is an indication that equation (2.4) should be revisited too for increased force estimation accuracy.

In regards of the spool valve model, the most obvious defect is seen in flow rate estimation functions given in equations (2.27) and (2.28). Both equations are expected to give the same flow rate when $L = 0$. But equation (2.28) yields infinity flow rate whereas equation (2.27) yields zero when $L = 0$. Figure 2.14 – is given to demonstrate the flow rate estimation performances of both equations around zero orifice opening with some arbitrary parameters for a single annular orifice.

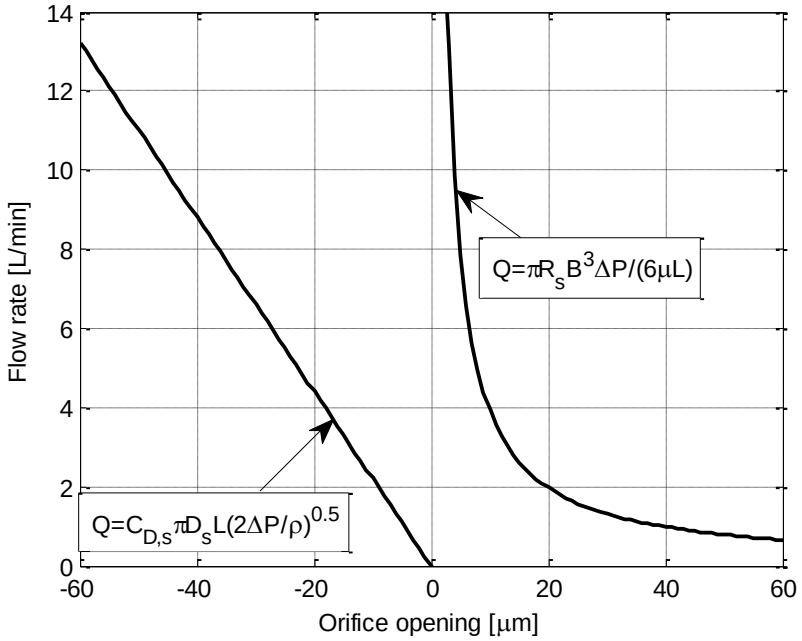

Figure 2.14 – Flow rate estimation performances of equations (2.27) and (2.28)

Wayne Anderson suggested a remedy to this inaccuracy around zero problem in ref. [18]; namely, to use the equation (2.40) instead of equations (2.27) and (2.28).

$$Q = \begin{cases} \dfrac{\pi R_s B^3}{6\mu L}\left(1 + \dfrac{3e^2}{2B^2}\right)\Delta P \; if \; L > L_t \\ C_{D,s}\pi D_s B\sqrt{\dfrac{2}{\rho}\Delta P} \; if \; 0 \le L \le L_t \\ C_{D,s}\pi D_s(|L| + B)\sqrt{\dfrac{2}{\rho}\Delta P} \; if \; L < 0 \end{cases} \tag{2.40}$$

where

$$L_t = \frac{B^2\left(1 + \dfrac{3e^2}{2B^2}\right)\sqrt{\Delta P}}{12\mu C_{D,s}\sqrt{\dfrac{2}{\rho}}} \tag{2.41}$$

Performance of equation (2.40) is compared to CFD analyses in Figure 2.15.

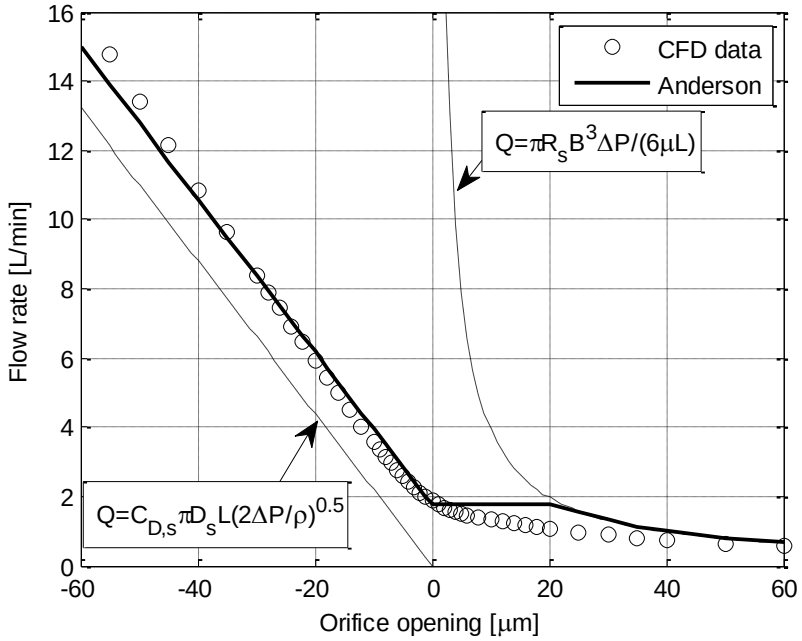

Figure 2.15 – Comparison of flow rate estimation performances of Anderson's algorithm and CFD analysis

In Figure 2.15, it is seen that Anderson's approach certainly captures the general form of numerical solution better than equations (2.27) and (2.28). But the overall curve consists of non-smooth transition points which would decrease the accuracy significantly when applied to the flow simulation of a four-way valve.

Performing accurate simulations around null position of a spool valve is crucial, since performance around null position directly dictates internal leakage and pressure sensitivity of a spool valve. So, this problem will be addressed in the following chapters for a more accurate spool valve flow model.

CHAPTER 3

DEVELOPING MORE ACCURATE FLOW MODELS

In this chapter, more accurate flow models reflecting the real geometrical aspects of the components are developed relying on the CFD analyses. To assure the accuracy of the CFD analysis results, right turbulence model and near wall treatment option are determined for such orifice flows by comparing the results of possible combination with test results.

3.1. Determination of Most Suitable Numerical Models

Control of fluid flow by a servovalve is accomplished by basically using orifices. To pick the turbulence model and near wall treatment option with the best flow rate estimation performance for orifice geometries, tests are conducted on a simple fixed orifice to obtain its flow rate vs. pressure curve. Then analyses are conducted on ANSYS Fluent ® with available models, and the most suitable model combination for the purposes of this study is determined.

The tested fixed orifice geometry is given in Figure 3.1.

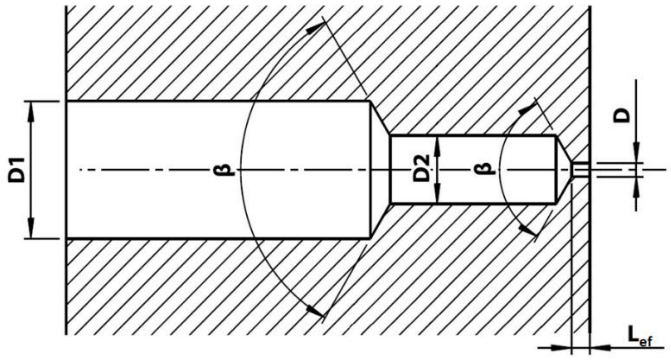

Figure 3.1 – Fixed orifice geometry used in tests and analyses

The diameter D1 is at the downstream of the flow. Nominal values of the dimensions in Figure 3.1 are given in Table 3.1.

Table 3.1 – Nominal dimensions of tested fixed orifice geometry

Dimension	Nominal Values
D1	2 mm
D2	1 mm
D	200 µm
L_e	270 µm
β	118°

The critical dimension here is the diameter "D", which is the orifice dimeter as can also be seen in Figure 3.2 in more detail.

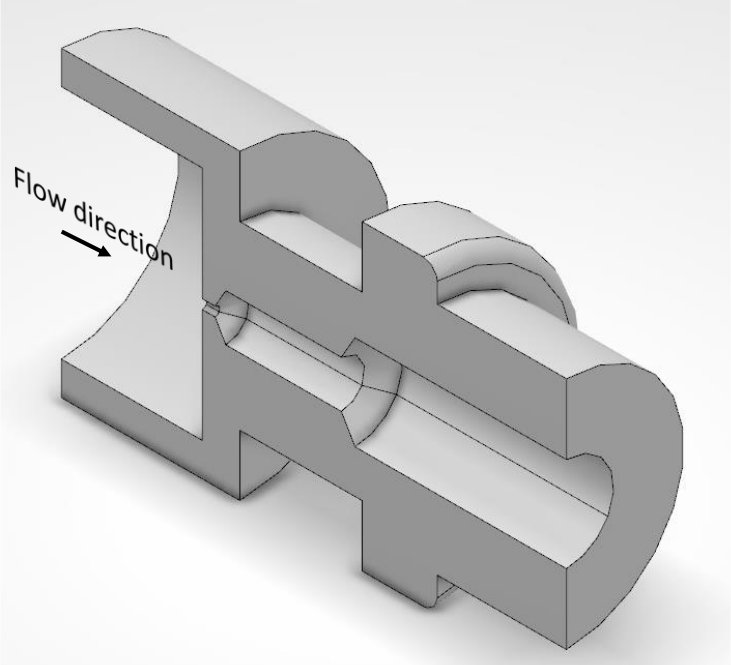

Figure 3.2 – Isometric view of fixed orifice CAD model cross section

Orifice diameter "D" of tested fixed orifice is measured in Dorsey Paragon 24P profile projector as 199.2 µm and this value is used in CFD analyses. The test are conducted using the assembly given in Figure 3.3.

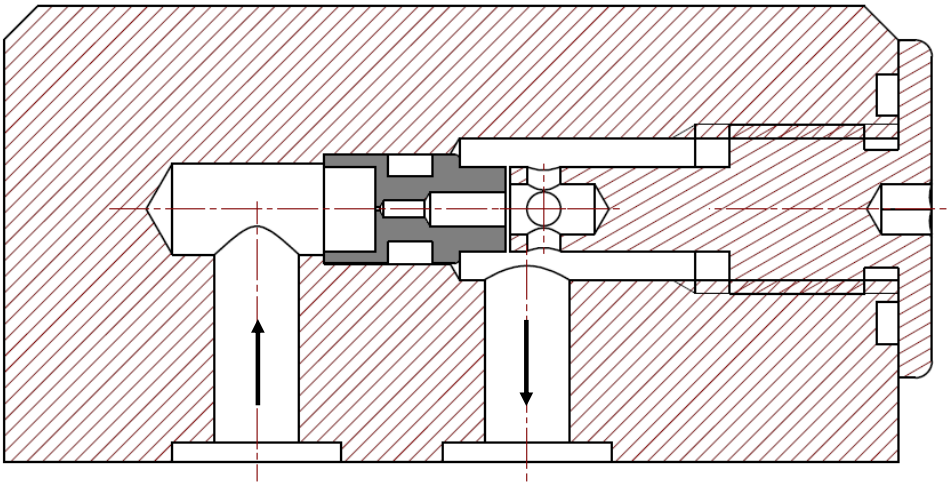

Figure 3.3 – Cross sectional view of fixed orifice test assembly

Inlet and outlet pressures are measured right at the entrance and exit of the assembly, respectively. The equipment and working fluid used in the tests are given in Table 3.2. To ensure the sealing between the orifice and the test block a Parker N0756 2-007 o-ring is used.

Table 3.2 – Equipments used in fixed orifice tests

Equipment	Company	Model	Details
Pump	Parker	PV080	Variable Displacement, 80cc
Flowmeter	VSE	VSI 0.1	10000 pulse/L resolution, 10 L/min maximum flow rate
Pressure sensor	Hydac	HDA 4846-A-400-000	0-400 bar measurement range, accuracy ≤ ±%0.125 FS
Pressure sensor	Hydac	HDA 4846-A-060-000	0-60 bar measurement range, accuracy ≤ ±%0.125 FS
Working fluid	Belgin Oil	MIL-H-5606	@20 °C

The result of the test is given in Figure 3.4.

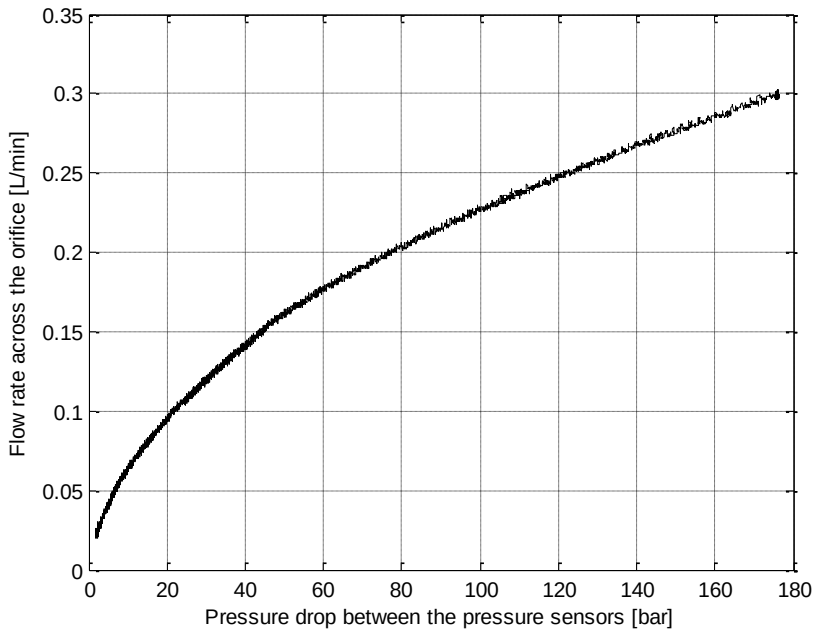

Figure 3.4 – Flow rate vs. pressure drop curve of the tested fixed orifice

Since inlet and outlet diameters of the test assembly are 5 mm each while the orifice diameter is 199.2 μm, the resistances to flow between each pressure sensor and the orifice can be neglected; i.e., pressure drop in the test can be assumed to be caused only by the fixed orifice. This assumption makes it possible to analyze the flow through fixed orifice in a 2D grid. To further justify this assumption an analysis is conducted using the full geometry in a 3D domain to calculate the pressure drops between the inlet/outlet and the orifice. 3D CAD model of the test assembly is given in Figure 3.5.

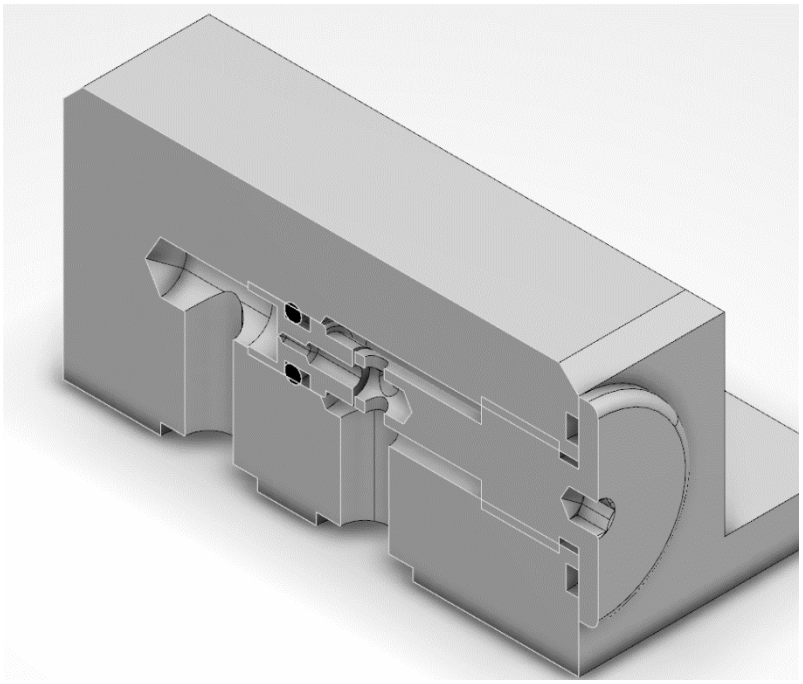

Figure 3.5 – Cross sectional view from the CAD model of the test assembly

In DesignModeler® the fluid volume inside the test assembly is extracted and simplified for analysis. The resulting geometry is shown in Figure 3.6. To reduce the computational time, only half of the volume is used benefiting from the symmetry.

The grid is generated on the geometry shown in Figure 3.6 with minimum 8 elements across any gap, growth rate of 1.08 and 5 levels of boundary layer on the walls. The resulting grid has 1,094,439 elements with a minimum orthogonal quality of 15.8%. The average orthogonal quality of the elements is 79.7% with the standard deviation of 11.8%.

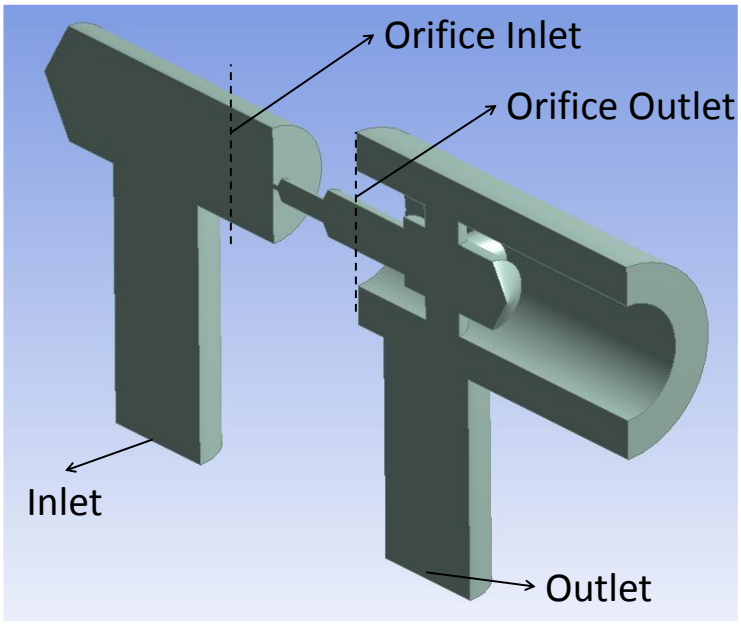

Figure 3.6 – Fluid volume used in 3D fixed orifice analysis

The convergence criteria used in Fluent is to drop below 10^{-3} for all equations. Second order upwind scheme is used to discretize all the governing equations. With 0.15 L/min inlet flow rate, which is the half of the maximum value seen in Figure 3.4 since half of the geometry is used, the computation is completed at 343rd iteration and final area weighted average static pressure values are given in Table 3.3.

Table 3.3 – Pressure drops according to CFD analysis

Surface	Pressure [bar]
Inlet	194.706
Orifice inlet	194.704
Orifice outlet	0.00357574
Outlet	0

There are 5 orders of magnitude of difference when the pressure drop across the orifice is compared to pressure drops across the other sections. This indicates that it is totally safe to assume that the pressure drop occurs only across the orifice. So the rest of the analyses are done in the 2D axisymmetric grid shown in Figure 3.7.

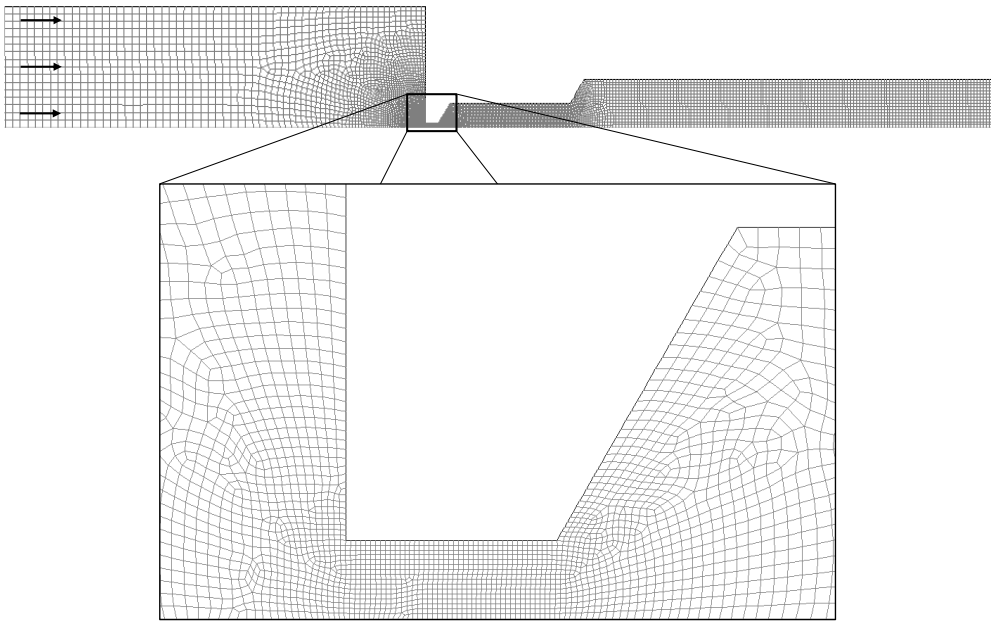

Figure 3.7 – The grid used in 2D axisymmetric fixed orifice analyses

Some details about the grid shown in Figure 3.7 are given in Table 3.4.

Table 3.4 – Information on the grid used in 2D axisymmetric fixed orifice analyses

Minimum num. of cells across any gap	16
Growth rate	1.04
Num. of elements	8524
Min. orthogonal quality	63%
Average orthogonal quality	98%
Std. dev. of orthogonal quality	3%

In Fluent following turbulence model and near-wall treatment options were used for comparison;

- Standard k-ε Model + Enhanced Wall Treatment
- Standard k-ε Model + Menter-Lechner
- Standard k-ε Model + Scalable Wall Functions
- RNG k-ε Model + Enhanced Wall Treatment

- RNG k-ε Model + Menter-Lechner
- RNG k-ε Model + Scalable Wall Functions
- Realizable k-ε Model + Enhanced Wall Treatment
- Realizable k-ε Model + Menter-Lechner
- Realizable k-ε Model + Scalable Wall Functions

Only the variations of the k-ε model are considered at first since k-ε model is the most widely used turbulence model in CFD analyses [46] and would probably offer an adequate performance with one of the possible combinations. Also use of k-ε model, along with second order upwind scheme for discretization of governing equations were justified before [47]. All the model constants related to the turbulence equations are left at their default values in Fluent 18.1. Flow rates corresponding to 13 different inlet pressure values ranging between 1 and 200 bar were calculated using ANSYS Workbench's parametric analysis capability on the grid shown in Figure 3.7 for 9 different turbulence model combinations in steady-state calculations. Other details about the calculations are given in Table 3.5.

Table 3.5 – Calculation details for 2D axisymmetric fixed orifice analyses

Convergence criteria	Residuals to drop below 10^{-4} for all equations
Pressure-Velocity coupling scheme	Coupled
Discretization scheme	Second order upwind for all equations
Maximum iteration	10000
Mesh adaption	Every 300th iteration
Max. level of refinement for adaption	2
Adaption method	Cells with at least 10% of max. velocity gradient
Material properties	Density: 860 kg/m3 Viscosity: 0.018 Pa·s (Properties of MIL-H-5606 @ 20 °C [48])

Results of the analyses are shown in Figure 3.8 to Figure 3.10.

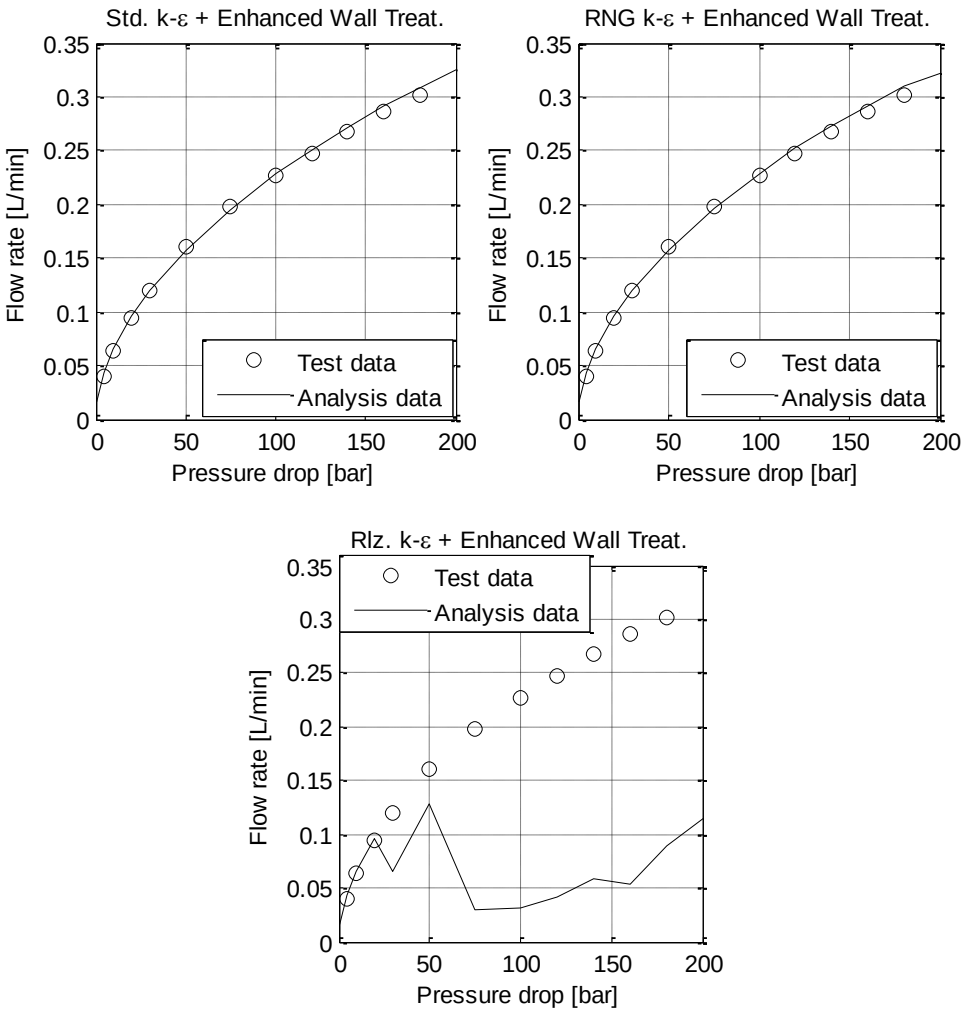

Figure 3.8 – Analysis results with Enhanced Wall Treatment

Figure 3.8 shows the results of the analyses conducted using "Enhanced Wall Treatment" near-wall treatment option. It is seen that Standard and RNG k-ε models shows similar flow rate estimation performances while Realizable k-ε model fails to meet the convergence criteria for most pressure drop values and ends up in unacceptable estimations.

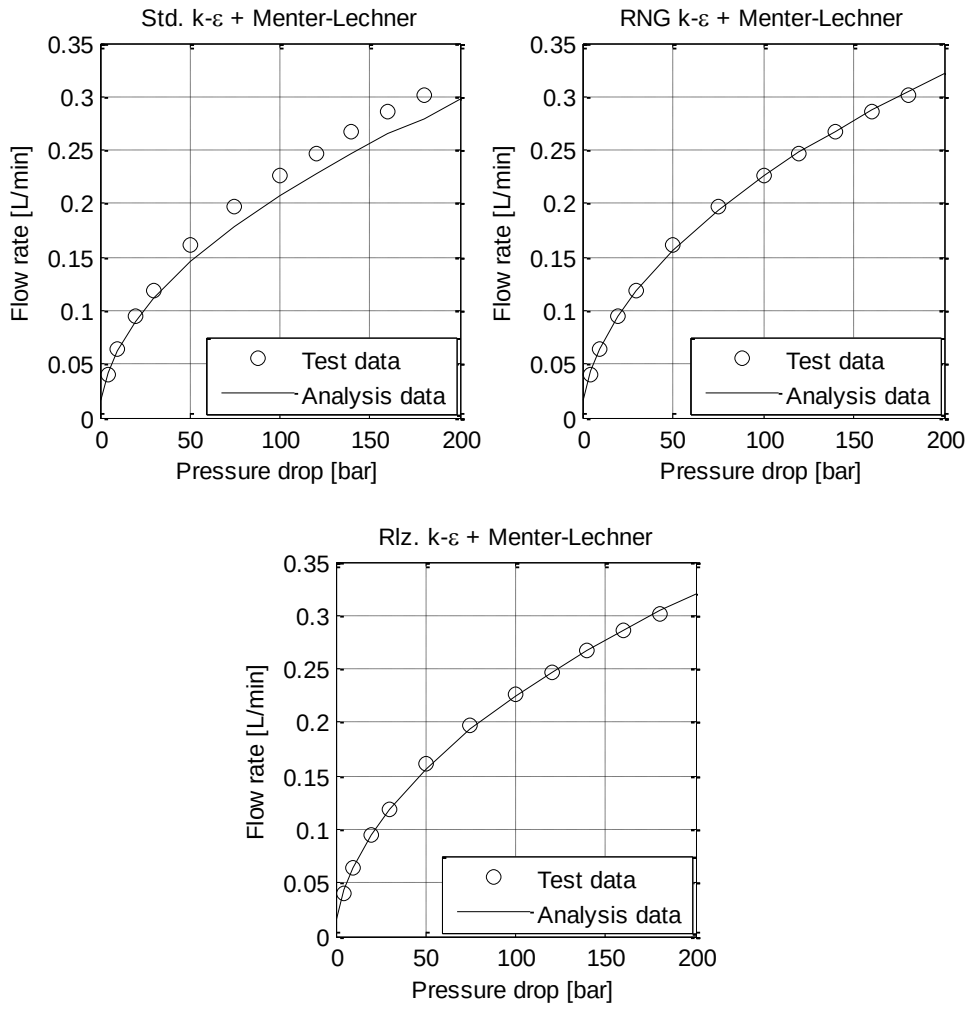

Figure 3.9 – Analysis results with Menter-Lechner

Figure 3.9 shows the results of the analyses conducted using "Menter-Lechner" near-wall treatment option. In this case using Standard k-ε model clearly results in underestimation of flow rate. But RNG and Realizable k-ε demonstrates promising performances.

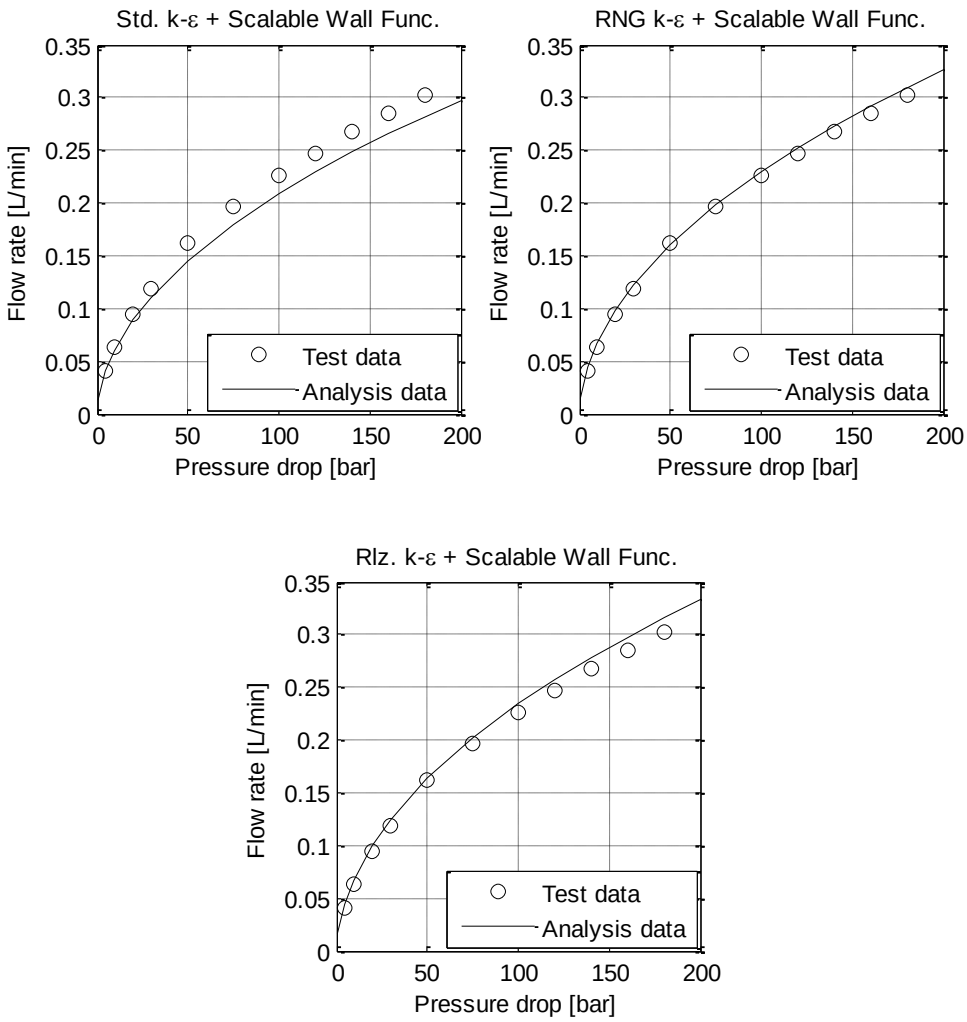

Figure 3.10 – Analysis results with Scalable Wall Functions

Figure 3.10 shows the results of the analyses conducted using "Scalable Wall Functions" near-wall treatment option. Standard k-ε model again underestimates the flow rate, while Realizable k-ε model overestimates it. In this case using RNG k-ε model shows better performance than the other combinations.

To assess the performances of the model combinations objectively, following penalty function is defined to grade them;

$$J = \int_{\Delta P=5\ bar}^{180\ bar} \left(\frac{Q_{test} - Q_{analysis}}{Q_{test}}\right)^2 dP \tag{3.1}$$

The penalty function is evaluated between 5 and 180 bar of pressure drop since this is the interval in which test data is available. The resulting error points are given in Table 3.6.

Table 3.6 – Flow rate estimation error points of turbulence models

RNG k-ε + Menter-Lechner	0.036
Realizable k-ε + Menter-Lechner	0.038
Standard k-ε + Enhanced Wall Treatment	0.049
RNG k-ε + Enhanced Wall Treatment	0.061
RNG k-ε + Scalable Wall Functions	0.097
Realizable k-ε + Scalable Wall Functions	0.270
Standard k-ε + Menter-Lechner	1.063
Standard k-ε + Scalable Wall Functions	1.101
Realizable k-ε + Enhanced Wall Treatment	Fail

According to Table 3.6 the best flow rate estimation performance is demonstrated by RNG k-ε + Menter-Lechner combination among the tested combinations. So the analyses in the following sections are conducted using RNG k-ε + Menter-Lechner combination.

3.2. Nozzle-Flapper Valve Model

As already mentioned, flow through a nozzle-flapper valve is modeled using equation (2.7). According to Figure 2.11, equation (2.7) is only valid when the curtain length is near zero. As the gap between nozzle and flapper increases, the error of equation (2.7) increases too since curtain area is no longer the controlling orifice and nozzle starts to behave like a fixed orifice. To reflect this effect in analytical formulation, a nozzle-flapper valve can be considered as two orifices connected in serial, as shown in Figure 3.11.

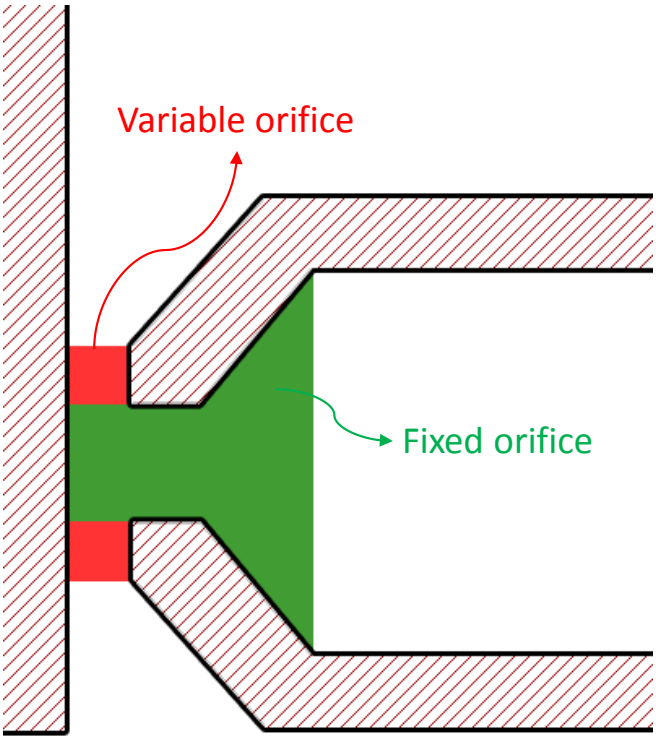

Figure 3.11 – Two orifices in a nozzle-flapper valve

Equivalent circuit diagram of the configuration shown in Figure 3.11 is given in Figure 3.12.

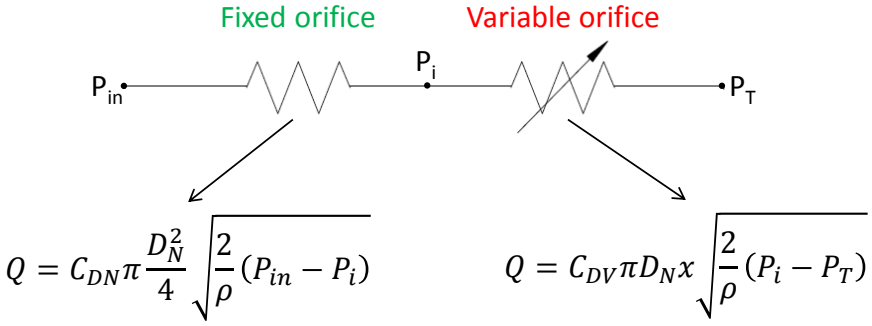

Figure 3.12 – Equivalent circuit diagram of a nozzle-flapper valve

Since the orifices are in serial, the flow rates through them are the same. If the flow rate equation of the fixed orifice in Figure 3.12 is solved for the intermediate pressure "P_i" it is found that

$$P_i = P_{in} - \frac{8Q^2\rho}{\pi^2 C_{D,n}^2 D_n^4} \tag{3.2}$$

Similarly solving the flow rate equation of the variable orifice for P_i one obtains

$$P_i = \frac{Q^2\rho}{2\pi^2 C_{D,v}^2 D_n^2 x^2} + P_T \tag{3.3}$$

Substituting the P_i definition of equation (3.2) into equation (3.3) and solving for the flow rate;

$$Q = \frac{C_{D,v} C_{D,n} \pi D_n^2 x}{\sqrt{16 C_{D,v}^2 x^2 + C_{D,n}^2 D_n^2}} \sqrt{\frac{2}{\rho}(P_{in} - P_T)} \tag{3.4}$$

The discharge coefficients of fixed and variable parts, i.e., $C_{D,n}$ and $C_{D,v}$ in equation (3.4) should be determined using CFD. To determine $C_{D,v}$, an axisymmetric nozzle-flapper valve geometry without the fixed orifice part, as shown in Figure 3.13 is modeled for CFD analyses.

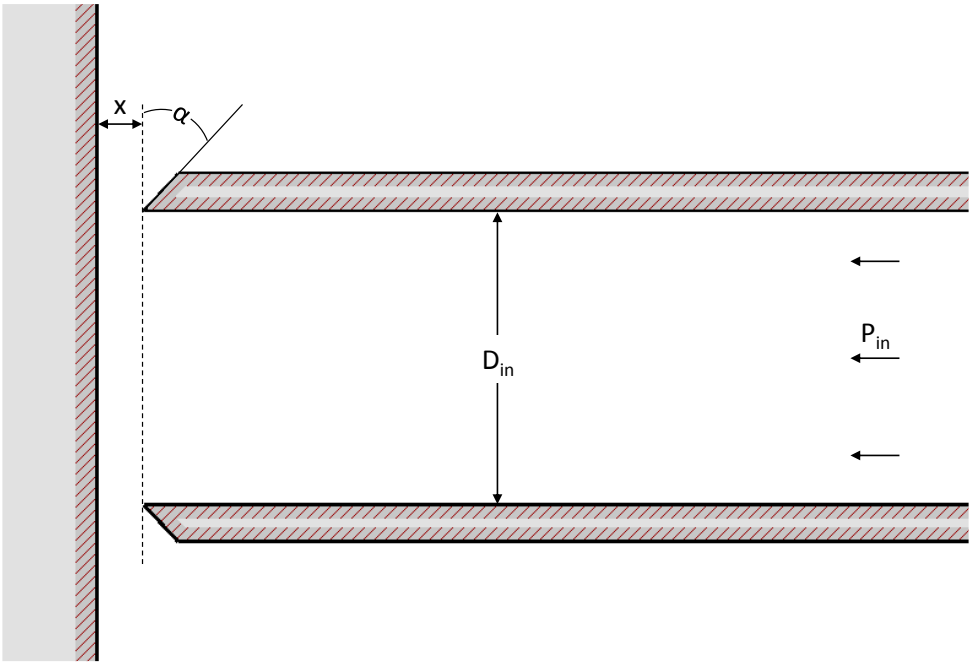

Figure 3.13 – Nozzle-flapper valve geometry with only the variable orifice

It is known that discharge coefficient is a function of geometry and Reynolds number [7]. So for the same geometry, such as the nozzle-flapper geometry shown in Figure 3.13, discharge coefficient should be modeled as a function of Reynolds number. The Reynolds number is defined as

$$Re = \frac{\rho V L}{\mu} \tag{3.5}$$

The characteristic length "L" is the curtain lenght "x" in Figure 3.13. To define a function for the discharge coefficient of which the Reynolds number is the independent variable, the Reynolds number must be estimated before the flow actually occurs. To make this estimation, flow velocity "V" can be substituted with the velocity definition of the standard orifice equation;

$$V = \sqrt{\frac{2}{\rho}\Delta P} \tag{3.6}$$

So the Reynolds number estimation becomes

$$Re^* = \frac{x\sqrt{2\rho\Delta P}}{\mu} \tag{3.7}$$

Since the outlet pressure is 0 bar in all the analyses, ΔP in equation (3.7) is actually the inlet pressure. To determine $C_{D,v}$ characteristic as a function of Re^*, analyses are conducted at 50 design points by varying x, ρ, P_{in} and μ to obtain flows at different Reynolds numbers on the geometry shown in Figure 3.13 with D_{in} = 4 mm and α = 30°. Details about grid generation and calculations are given in Table 3.7.

The resulting $C_{D,v}$ vs. Re^* graph is given in Figure 3.14. As shown in the figure, $C_{D,v}$ approaches to 0.616 as Re^* approaches to infinity. This value is consistent with the theoretical discharge coefficient value for sharp edged orifices, known to be 0.611 in the literature with a minor error [49] [50]. The general shape of the curve is also consistent with the typical discharge coefficient vs. Reynolds number curves in the literature [7] [51].

Table 3.7 – Calculation details for nozzle-flapper valve discharge coefficient analyses

Minimum num. of cells across any gap	25
Growth rate	1.04
Convergence criteria	Change in the flow rate to drop below 10^{-6}% with respect to previous iteration
Pressure-Velocity coupling scheme	Coupled
Discretization scheme	Second order upwind for all equations
Turbulence Model	RNG k-ε
Near Wall Treatment	Menter-Lechner
Maximum iteration	5000
Mesh adaption	Every 250th iteration
Max. level of refinement for adaption	2
Adaption method	Cells with at least 10% of max. velocity gradient

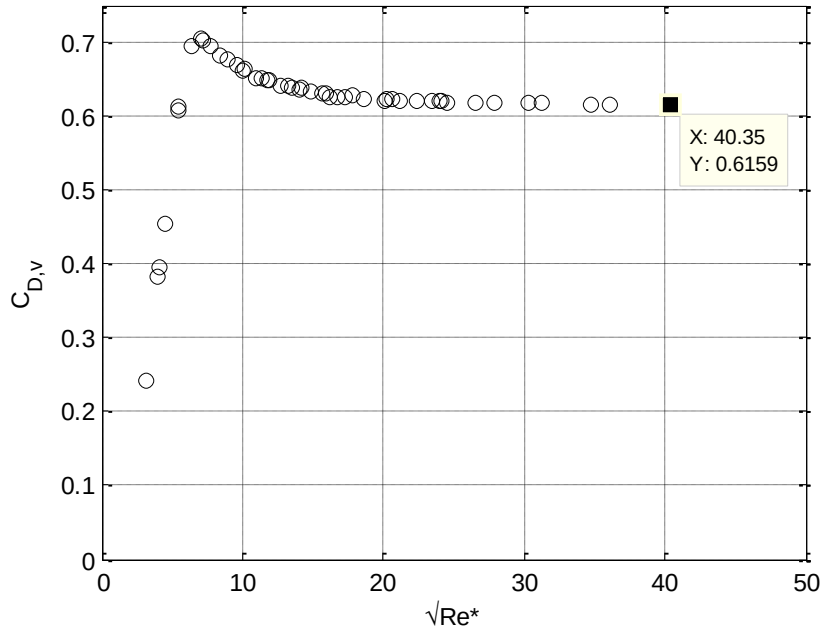

Figure 3.14 – $C_{D,v}$ vs. Re curve*

With the discharge characteristic given in Figure 3.14 is known, one might consider to use the asymptotical value as a constant discharge coefficient in equation (3.4), or fit a function to the discharge coefficient data for a more accurate model an use variable $C_{D,v}$. A third option could be to determine the Reynolds number around

which the valve to be modeled is working and use the corresponding $C_{D,v}$, again as a constant.

Before proceeding with one of these options, effects of geometrical changes on discharge coefficient should be examined too. At first, the effect of changes in the angle "α" is examined (refer to Figure 3.13). The same numerical analysis, of which the details are given in Table 3.7 is conducted again for 5 different values of α (10, 20, 45, 60 and 75°).

Figure 3.15 shows the effect of bevel angle on $C_{D,v}$ for $\alpha = 10$ and 20°. In equation (3.7), x is defined as an independent variable of Re^*. So, if $C_{D,v}$ is expected to be a function of Re^* only, changes in x should not affect the $C_{D,v}$ if Re^* is constant. By looking at the discontinuities at transition points for x, Figure 3.15a clearly tells that this is not the case for $\alpha = 10°$. The reason for that is, fluid is forced to flow through a narrow gap for smaller values of x when α is below a certain value, so the orifice shape observed in such a situation cannot be considered as sharp edged anymore. This observation points out that it is not enough to introduce x only in the definition of Re^*. Rather, $C_{D,v}$ should be a function of both x and Re^*. In Figure 3.15b, it is seen that this effect is not as severe as it is for $\alpha = 10°$, but it still exists.

$C_{D,v}$ characteristics for $\alpha = 45$ and 75° are shown in Figure 3.16. It is seen that overshoot from the asymptotical value of 0.611 still exist for $\alpha = 45°$, but much less significant than it is for $\alpha = 10$ and 20°. For $\alpha = 75°$ there is no overshoot, but $C_{D,v}$ approaches the asymptotical value with a low rate. It is desirable to have a constant discharge coefficient over the widest possible Reynolds number range for a predictable flow rate performance. Figure 3.16 shows that an optimum bevel angle for this purpose can be determined between 45 and 75°. Figure 3.17 is given to illustrate that a bevel angle of 50° is a good value to have a constant discharge coefficient for the geometry in Figure 3.13.

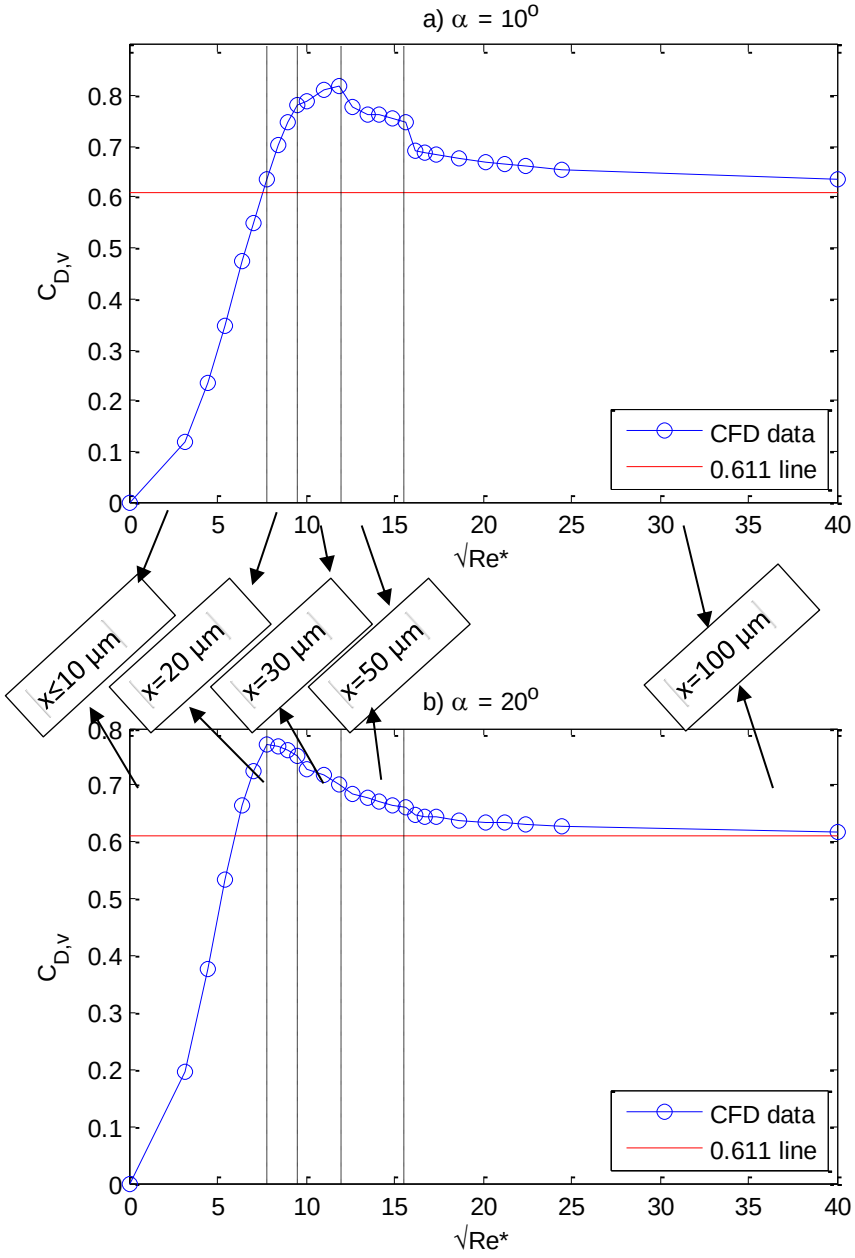

Figure 3.15 – The effect of bevel angle on C_{DV} for α = 10 and 20°

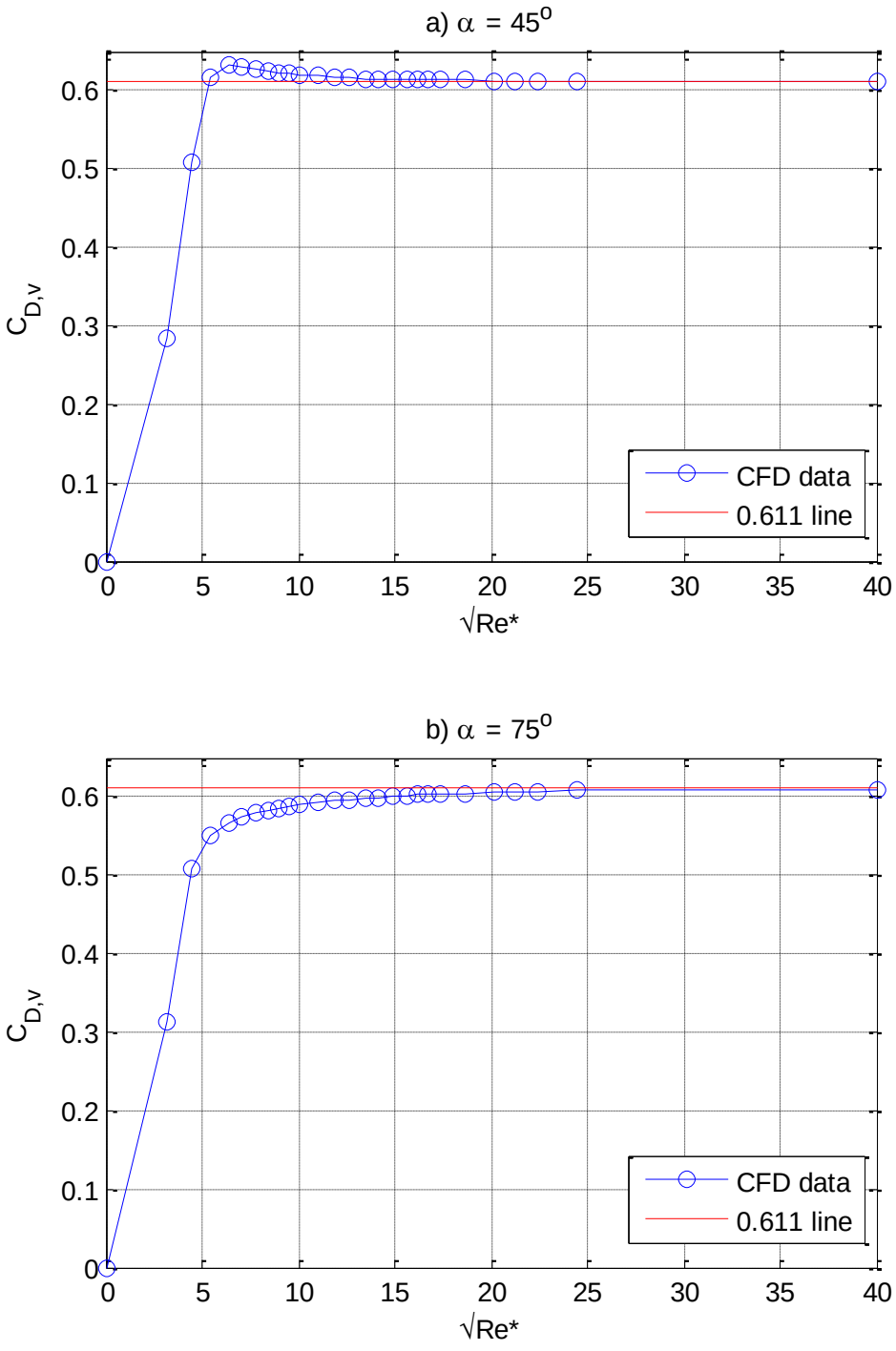

Figure 3.16 - The effect of bevel angle on C_{DV} for α = 45 and 75°

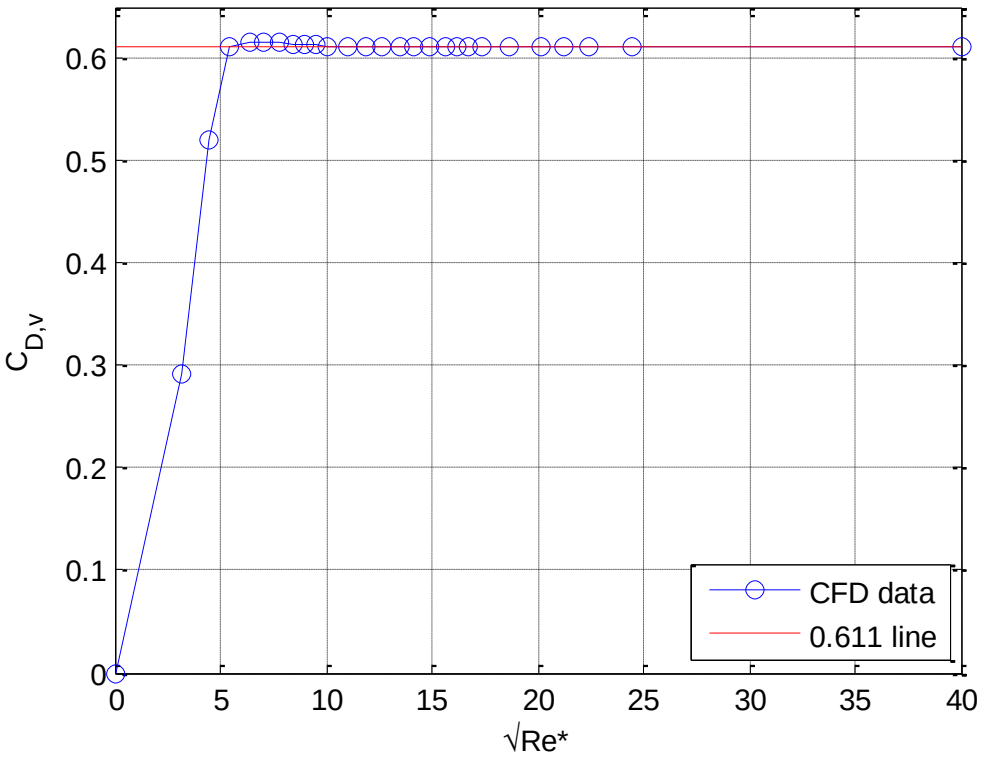

Figure 3.17 – C_{DV} curve for $\alpha = 50°$

To determine discharge coefficients $C_{D,v}$ and $C_{D,n}$ of nozzle, and $C_{D,f}$ of fixed orifice in the same analysis a full factorial numerical analysis is conducted with the fixed orifice geometry shown in Figure 3.1 is connected in serial to the nozzle geometry shown Figure 2.3. Design variables of the analysis with corresponding high and low values are given in Table 3.8.

Table 3.8 – First stage full factorial analysis desing variables

Variable	High Value (µm)	Low Value (µm)
L_c	400	200
L_{en}	300	100
L_{ef}	300	100
R_f	150	100
R_n	150	100

L_c in Table 3.8 is the lap length in Figure 2.3 defined as;

$$L_c = \frac{(D_c - D_n)}{2} \tag{3.8}$$

All design points are analyzed at seven different curtain lengths of 5, 10, 20, 40, 75, 100 and 500 μm. Analyses are conducted with the settings given in Table 3.9, with inlet and outlet pressures of 200 and 0 bar, respectively. Bevel angle "α" in Figure 2.3 is fixed at 50° as found to be optimum previously, and the angle "β" is fixed at standard drill angle of 118° [52]. The pressure between the nozzle and the fixed orifice, the flow rate and the force applied on the flapper are obtained from the analyses.

Table 3.9 – Calculation details for first stage discharge coefficient analyses

Minimum num. of cells across any gap	16
Growth rate	1.04
Convergence criteria	Change in the flow rate, intermediate pressure and force on the flapper to drop below 10^{-5}% with respect to previous iteration
Pressure-Velocity coupling scheme	Coupled
Discretization scheme	Second order upwind for all equations
Turbulence Model	RNG k-ε
Near Wall Treatment	Menter-Lechner
Maximum iteration	4000
Mesh adaption	Every 100th iteration
Max. level of refinement for adaption	2
Adaption method	Cells with at least 10% of max. velocity gradient
Material properties	Density: 860 kg/m3 Viscosity: 0.018 Pa·s (Properties of MIL-H-5606 @ 20 °C [48])

At 500 μm of curtain length, the flow rate is already become independent of the curtain length (see Figure 2.11), i.e., the variable orifice part of the nozzle-flapper valve in Figure 3.11 is ineffective and nozzle is acting as a fixed orifice. So, the equivalent circuit representation of this case becomes as shown in Figure 3.18.

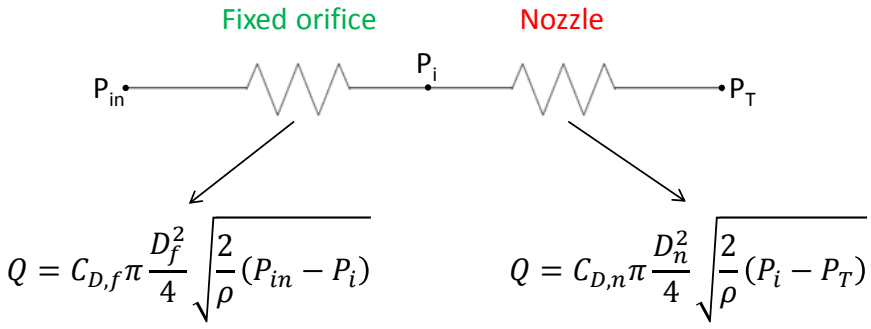

Figure 3.18 – Fixed orifice and nozzle connected in serial when the flapper is far away

Therefore P_i and Q data obtained for 500 µm curtain length is used to determine $C_{D,n}$ and $C_{D,f}$ in the equations given on Figure 3.18 and result are given in Table 3.10. The mean values for $C_{D,n}$ and $C_{D,f}$ are accepted as their respective values.

After $C_{D,n}$ and $C_{D,f}$ are determined, the analysis data for 5, 10, 20, 40, 75 and 100 µm curtain lengths are used to determine $C_{D,v}$. This time only the nozzle-flapper portion of the analysis domain is of interest, through which the flow rate is defined by equation (3.4). P_{in} in the equation (3.4) is P_i as shown in Figure 3.18 and P_T is zero.

Taking the flow rate data from the analysis reference, the $C_{D,v}$ value yielding the lowest error according to the penalty function given in equation (3.9) for each case given in Table 3.10 is found.

$$J = \sum_{x=5\mu m}^{100\mu m} \left(\frac{|q_{ref} - q_x|}{q_{ref}}\right)^2 x \tag{3.9}$$

In equation (3.9) x is the curtain length, q_{ref} and q_x are the flow rates found in analysis and calculated by equation (3.4) for that curtain length, respectively. Since equation (3.4) is already expected to yield high error at low curtain lengths due to the effect of lap length L_c, penalty is multiplied by x in equation (3.9) to ensure that error at higher x values are penalized more.

Table 3.10 – $C_{D,f}$ and $C_{D,n}$ values calculated in 500 μm

Case	L_c	L_{en}	R_f	L_{ef}	R_n	$C_{D,f}$	$C_{D,n}$	$C_{D,v}$
1	200	100	100	100	100	0,730	0,817	0,904
2	200	100	100	100	150	0,714	0,822	0,859
3	200	100	100	300	100	0,760	0,817	0,903
4	200	100	100	300	150	0,766	0,821	0,857
5	200	100	150	100	100	0,699	0,821	0,904
6	200	100	150	100	150	0,669	0,818	0,844
7	200	100	150	300	100	0,762	0,821	0,905
8	200	100	150	300	150	0,765	0,813	0,843
9	200	300	100	100	100	0,728	0,789	0,881
10	200	300	100	100	150	0,714	0,817	0,861
11	200	300	100	300	100	0,760	0,791	0,880
12	200	300	100	300	150	0,766	0,821	0,859
13	200	300	150	100	100	0,699	0,804	0,885
14	200	300	150	100	150	0,668	0,836	0,844
15	200	300	150	300	100	0,761	0,805	0,885
16	200	300	150	300	150	0,766	0,836	0,842
17	400	100	100	100	100	0,728	0,816	0,940
18	400	100	100	100	150	0,714	0,821	0,941
19	400	100	100	300	100	0,761	0,817	0,939
20	400	100	100	300	150	0,766	0,822	0,939
21	400	100	150	100	100	0,700	0,821	0,949
22	400	100	150	100	150	0,669	0,818	0,917
23	400	100	150	300	100	0,762	0,821	0,950
24	400	100	150	300	150	0,765	0,813	0,917
25	400	300	100	100	100	0,728	0,789	0,907
26	400	300	100	100	150	0,714	0,817	0,941
27	400	300	100	300	100	0,760	0,791	0,907
28	400	300	100	300	150	0,767	0,823	0,939
29	400	300	150	100	100	0,699	0,804	0,922
30	400	300	150	100	150	0,668	0,836	0,914
31	400	300	150	300	100	0,762	0,805	0,921
32	400	300	150	300	150	0,766	0,836	0,911
					Mean	0,733	0,816	0,900
					Std. Dev.	0,034	0,013	0,034

After determination of all the discharge coefficients, developed analytical model is tested for its flow rate and control pressure estimation performance by comparing its

results to CFD data. The comparison graphs for some cases are given in figures Figure 3.19 and Figure 3.20. It shows that the model can calculate the flow rate and control pressure for different cases with a minimal amount of error.

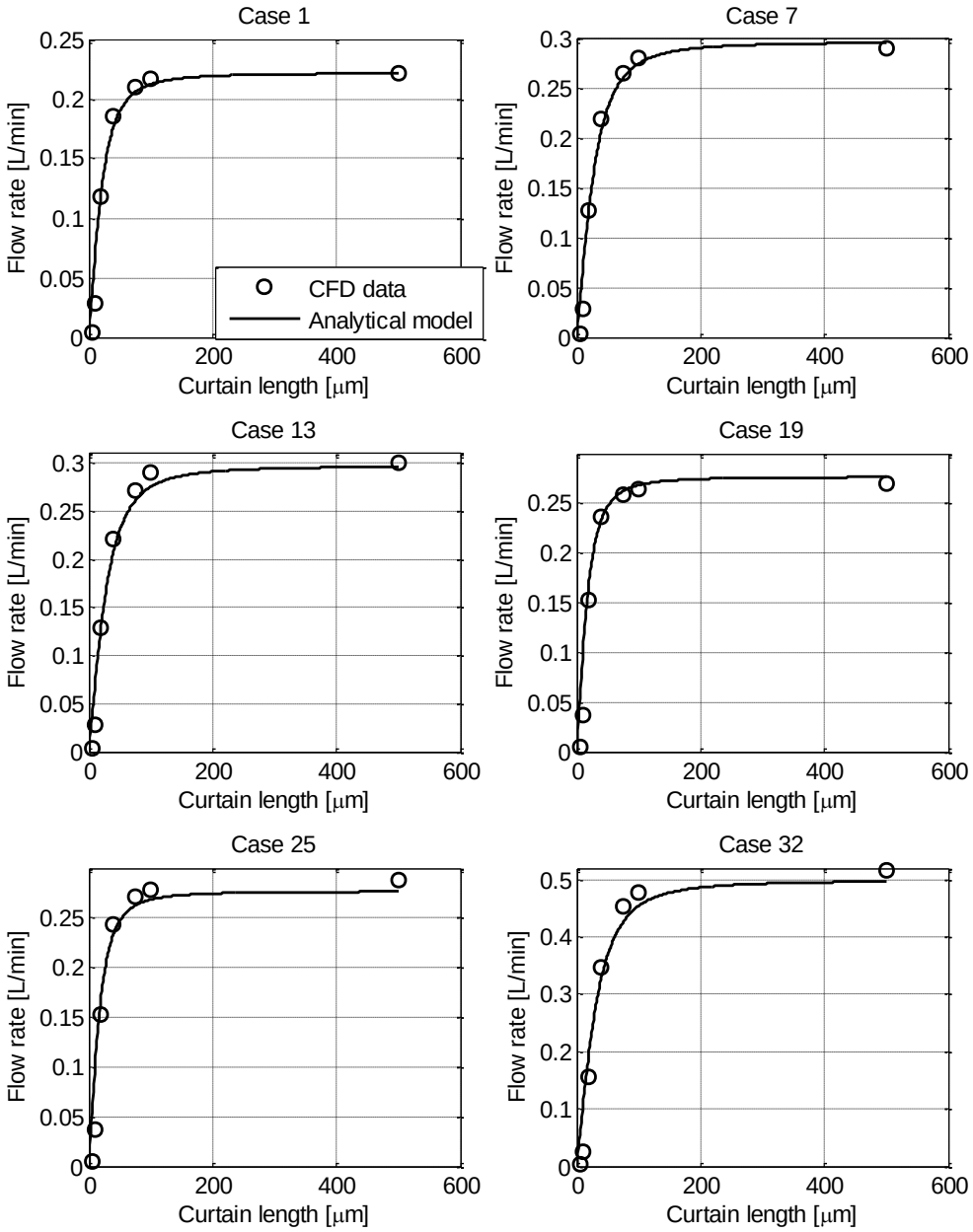

Figure 3.19 – Flow rate estimation performance of analytical model compared to CFD data of selected cases

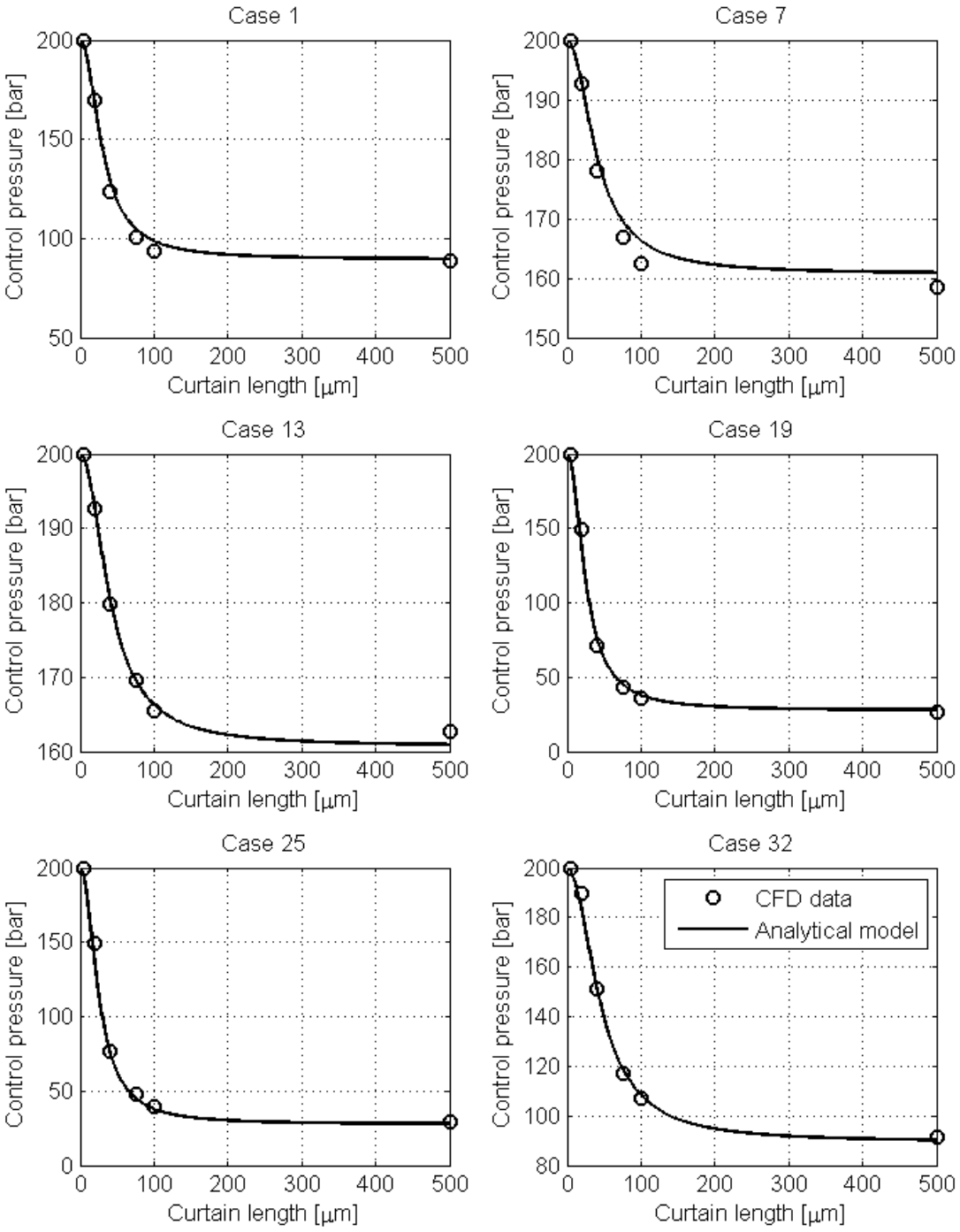

Figure 3.20 – Control pressure estimation performance of analytical model compared to CFD data of selected cases

3.2.1. Pressure Sensitivity Analysis

Although Zhu and Fei question its validity in their 2016 paper [25], nozzle-flapper valves are heavily designed according to maximum pressure sensitivity criterion and they underline this fact too. So, the model proposed in this study will be compared against the classical nozzle-flapper valve model in terms of its pressure sensitivity estimation performance.

By pressure sensitivity here, the rate of change of pressure difference between the branches of nozzle-flapper valve at zero flapper position is implied. Since this pressure difference ($P_r - P_l$ refering to Figure 2.3) creates the force causing the spool to move, it will be referred from here on as control pressure;

$$P_c \triangleq P_r - P_l \tag{3.10}$$

So the mathematical expression for pressure sensitivity can be written as;

$$K_{ps} = \left.\frac{\partial P_c}{\partial x_f}\right|_{x_f=0} \tag{3.11}$$

Having high first stage pressure sensitivity improves a double stage servovalve's both static and dynamic performance, so it makes sense to design the first stage for maximum pressure sensitivity. So different nozzle-flapper valve analytical models are compared in this section in terms of their curtain length estimation performances to achieve maximum pressure sensitivity. For this comparison the results obtained by each model are compared against the CFD analysis result to assess its accuracy. Compared models are given in Figure 3.21.

Model 1: Classical Nozzle-Flapper Valve Model:

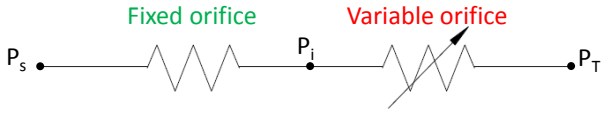

Model 2: Classical Nozzle-Flapper Valve Model w/ Drain Orifice:

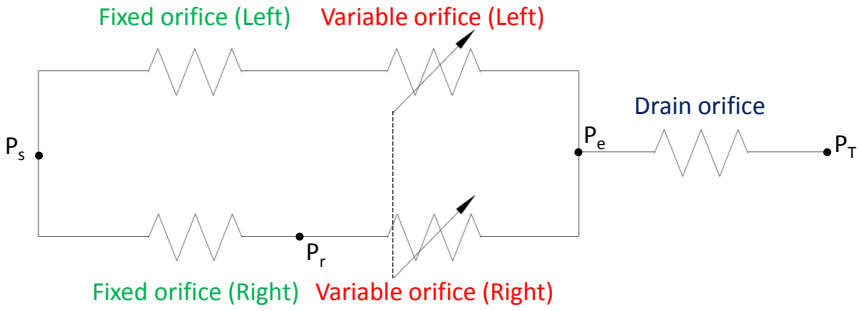

Model 3: Developed Nozzle-Flapper Valve Model w/ Drain Orifice:

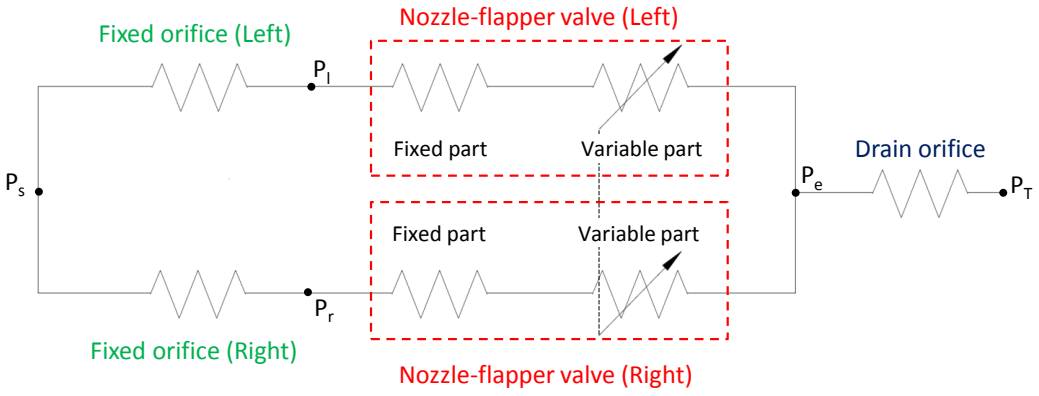

Figure 3.21 – First stage models compared in this section

Referring to Figure 3.21, for Model 1 the continuity equation for the left branch of the nozzle-flapper valve given in Figure 2.2 is as follows;

$$C_{D,f}\frac{\pi D_f^2}{4}\sqrt{\frac{2}{\rho}(P_s - P_l)} = C_{D,n}\pi D_n(x_0 + x_f)\sqrt{\frac{2}{\rho}P_l} \tag{3.12}$$

Solving for P_l one obtains

$$P_l = \frac{C_{D,f}^2 D_f^4 P_s}{C_{D,f}^2 D_f^4 + 16 C_{D,n}^2 D_n^2 \left(x_0 + x_f\right)^2} \tag{3.13}$$

Similarly, the pressure at the right branch is found as

$$P_r = \frac{C_{D,f}^2 D_f^4 P_s}{C_{D,f}^2 D_f^4 + 16 C_{D,n}^2 D_n^2 \left(x_0 - x_f\right)^2} \tag{3.14}$$

Evaluating equation (3.11) pressure sensitivity is found as

$$K_{ps} = \frac{64 C_{D,f}^2 D_f^4 C_{D,n}^2 D_n^2 x_0 P_s}{\left(C_{D,f}^2 D_f^4 + 16 C_{D,n}^2 D_n^2 x_0^2\right)^2} \tag{3.15}$$

To find the x_0 value that maximizes K_{ps}, which will be denoted as $\tilde{x}_0$ from here on, equation (3.16) should be solved for x_0;

$$\frac{\partial K_{ps}}{\partial x_0} = 0 \tag{3.16}$$

The resulting $\tilde{x}_0$ definition is found as

$$\tilde{x}_0 = \frac{C_{D,f} D_f^2 \sqrt{3}}{12 C_{D,n} D_n} \tag{3.17}$$

Model 2 introduces a drain orifice after the first stage, which is used in two stage servovalves to eliminate the risk of cavitation [27] [28] [53]. To make the model manageable, it should be assumed that the exit pressure P_e is constant at its value at $x_f = 0$. In reality P_e should change during the operation of the servovalve since the flow rate through the drain orifice changes with respect to x_f. But since the movement of flapper increases the restriction on one nozzle while decreasing it on the other, it makes sense to assume that these effects cancel out each other and the flow rate through the drain orifice (i.e., tare flow) stays constant.

Since the intermediate pressures at both branches are equal at $x_f = 0$ ($P_r = P_l$), referring to the intermediate pressure as P_i the continuity equation through the drain orifice at $x_f = 0$ becomes

$$2C_{D,n}\pi D_n x_0 \sqrt{\frac{2}{\rho}(P_i - P_e)} = C_{D,E}\frac{\pi D_E^2}{4}\sqrt{\frac{2}{\rho}P_e} \tag{3.18}$$

When solved for P_e;

$$P_e = \frac{64C_{D,n}^2 D_n^2 x_0^2}{C_{D,e}^2 D_e^4 + 64C_{D,n}^2 D_n^2 x_0^2} P_i \tag{3.19}$$

The continuity equation through a nozzle at $x_f = 0$ is

$$C_{D,f}\frac{\pi D_f^2}{4}\sqrt{\frac{2}{\rho}(P_s - P_i)} = C_{D,n}\pi D_n x_0 \sqrt{\frac{2}{\rho}(P_i - P_e)} \tag{3.20}$$

Substituting the P_e definition in equation (3.19) into (3.20) and solving for P_i it is found that

$$P_i = \frac{C_{D,f}^2 D_f^4 \left(C_{D,e}^2 D_e^4 + 64C_{D,n}^2 D_n^2 x_0^2\right)}{16C_{D,n}^2 D_n^2 x_0^2 C_{D,e}^2 D_e^4 + C_{D,f}^2 D_f^4 \left(C_{D,e}^2 D_e^4 + 64C_{D,n}^2 D_n^2 x_0^2\right)} P_s \tag{3.21}$$

Again substituting equation 3.21 into 3.19 the final definition of P_e is found as

$$P_e = \frac{64C_{D,n}^2 D_n^2 x_0^2 C_{D,f}^2 D_f^4}{16C_{D,n}^2 D_n^2 x_0^2 C_{D,e}^2 D_e^4 + C_{D,f}^2 D_f^4 \left(C_{D,e}^2 D_e^4 + 64C_{D,n}^2 D_n^2 x_0^2\right)} P_s \tag{3.22}$$

Now that the pressure at nozzles exits is defined the continuity equation for the left and right branches becomes, respectively

$$C_{D,f}\frac{\pi D_f^2}{4}\sqrt{\frac{2}{\rho}(P_s - P_l)} = C_{D,n}\pi D_n \left(x_0 + x_f\right)\sqrt{\frac{2}{\rho}(P_l - P_e)} \tag{3.23}$$

$$C_{D,f}\frac{\pi D_f^2}{4}\sqrt{\frac{2}{\rho}(P_s-P_r)}=C_{D,n}\pi D_n\left(x_0-x_f\right)\sqrt{\frac{2}{\rho}(P_r-P_e)} \tag{3.24}$$

The rest of the procedure is the same as it is for Model 1. By substituting the P_e definition given in equation (3.22) into (3.23) and (3.24) and solving for P_l and P_r, the intermediate pressure definitions for both branches are found and control pressure can be defined as it is given in equation (3.10). Then equations (3.11) and (3.16) are evaluated to find the curtain length that yields the maximum pressure sensitivity as

$$\tilde{x}_0=\sqrt{\frac{2C_{D,f}^2D_f^4\sqrt{C_{D,e}^4D_e^8+4C_{D,f}^2D_f^4C_{D,e}^2D_e^4+C_{D,f}^4D_f^8}-2C_{D,f}^4D_f^8-C_{D,f}^2D_f^4C_{D,e}^2D_e^4}{48C_{D,n}^2D_n^2\left(C_{D,e}^2D_e^4+4C_{D,f}^2D_f^4\right)}} \tag{3.25}$$

Evaluation of Model 3 is very similar to Model 2's except for the definition of flow rate through nozzle, which is this time given as

$$Q=\frac{C_{D,v}C_{D,n}\pi D_n^2(x_0\pm x_f)}{\sqrt{16C_{D,v}^2(x_0\pm x_f)^2+C_{D,n}^2D_n^2}}\sqrt{\frac{2}{\rho}(P_i-P_e)} \tag{3.26}$$

To define the exit pressure P_e first, the continuity equation through the drain orifice is written in the same way as equation (3.18);

$$2\frac{C_{D,v}C_{D,n}\pi D_n^2x_0}{\sqrt{16C_{D,v}^2x_0+C_{D,n}^2D_n^2}}\sqrt{\frac{2}{\rho}(P_i-P_e)}=C_{D,e}\frac{\pi D_e^2}{4}\sqrt{\frac{2}{\rho}P_e} \tag{3.27}$$

Solving for P_e it is found that

$$P_e=\frac{64C_{D,n}^2C_{D,v}^2D_n^2x_0^2}{\lambda}P_i \tag{3.28}$$

where

$$\lambda = 64C_{D,n}^2 C_{D,v}^2 D_n^2 x_0^2 + C_{D,e}^2 D_e^4 \left(16C_{D,v}^2 x_0^2 + C_{D,n}^2 D_n^2\right) \tag{3.29}$$

The continuity equation through a nozzle at $x_f = 0$ is

$$C_{D,f} \frac{\pi D_f^2}{4} \sqrt{\frac{2}{\rho}(P_s - P_i)} = \frac{C_{D,v} C_{D,n} \pi D_n^2 x_0}{\sqrt{16C_{D,v}^2 x_0 + C_{D,n}^2 D_n^2}} \sqrt{\frac{2}{\rho}(P_i - P_e)} \tag{3.30}$$

Substituting the P_e definition in equation (3.28) into (3.30) and solving for P_i it is found that

$$P_i = \frac{C_{D,f}^2 D_f^4 \lambda}{C_{D,f}^2 D_f^4 \lambda + 16C_{D,n}^2 C_{D,v}^2 C_{D,e}^2 D_n^4 D_e^4 x_0^2} P_s \tag{3.31}$$

Again substituting equation (3.28) into (3.31) the final definition of P_e is found as

$$P_e = \frac{64C_{D,n}^2 C_{D,v}^2 C_{D,f}^2 D_n^2 D_f^4 x_0^2}{C_{D,f}^2 D_f^4 \lambda + 16C_{D,n}^2 C_{D,v}^2 C_{D,e}^2 D_n^4 D_e^4 x_0^2} P_s \tag{3.32}$$

Now that the pressure at nozzles exits is defined the continuity equation for the left and right branches becomes, respectively

$$C_{D,f} \frac{\pi D_f^2}{4} \sqrt{\frac{2}{\rho}(P_s - P_l)} = \frac{C_{D,v} C_{D,n} \pi D_n^2 (x_0 + x_f)}{\sqrt{16C_{D,v}^2 (x_0 + x_f)^2 + C_{D,n}^2 D_n^2}} \sqrt{\frac{2}{\rho}(P_l - P_e)} \tag{3.33}$$

$$C_{D,f} \frac{\pi D_f^2}{4} \sqrt{\frac{2}{\rho}(P_s - P_r)} = \frac{C_{D,v} C_{D,n} \pi D_n^2 (x_0 - x_f)}{\sqrt{16C_{D,v}^2 (x_0 - x_f)^2 + C_{D,n}^2 D_n^2}} \sqrt{\frac{2}{\rho}(P_r - P_e)} \tag{3.34}$$

The rest of the procedure is the same as the previous models. By substituting the P_e definition given in equation (3.32) into (3.33) and (3.24) and solving for P_l and P_r, the intermediate pressure definitions for both branches are found and control pressure can be defined as it is given in equation (3.10). Then equations (3.11) and (3.16) are evaluated to find $\tilde{x}_0$, but the definition will not be given here explicitly since this time it is a little overcrowded. One could use an equation manipulator such as MATLAB's Symbolic Math Toolbox® to obtain the definition. MATLAB code for this purpose is given in Appendix A for reference.

Numerical values of discharge coefficients used in the models are given Table 3.11.

Table 3.11 – Discharge coefficients used with the models

Variable	Value	Notes
$C_{D,f}$	0.733	Table 3.10
$C_{D,n}$	0.816	For Model 3 (Table 3.10)
	0.600	For Model 1 and 2 [7]
$C_{D,v}$	0.900	Table 3.10
$C_{D,e}$	0.700	[7]

And for the diameters, it is assumed that fixed orifice diameter is equal to nozzle diameter while the exit orifice diameter is twice of it. With these values $\tilde{x}_0$ estimations of three models are given in Table 3.12.

Table 3.12 – $\tilde{x}_0$ estimations of the models

Model	$\tilde{x}_0$
1	$0.1763D_n$
2	$0.1657D_n$
3	$0.0844D_n$

CFD analyses are conducted using the same configuration with the models, at $\tilde{x}_0$ values given in Table 3.12, with a similar set up given in Table 3.9. x_0 values of $0.0625D_n$ and $0.125D_n$ are also included in the analyses to expand the data for easier interpretation. Pressure sensitivity values are calculated for three x_f values,

namely $0.005D_n$, $0.015D_n$ and $0.025D_n$, to also see the change in the pressure sensitivity with respect to flapper position. Results are given in Figure 3.22.

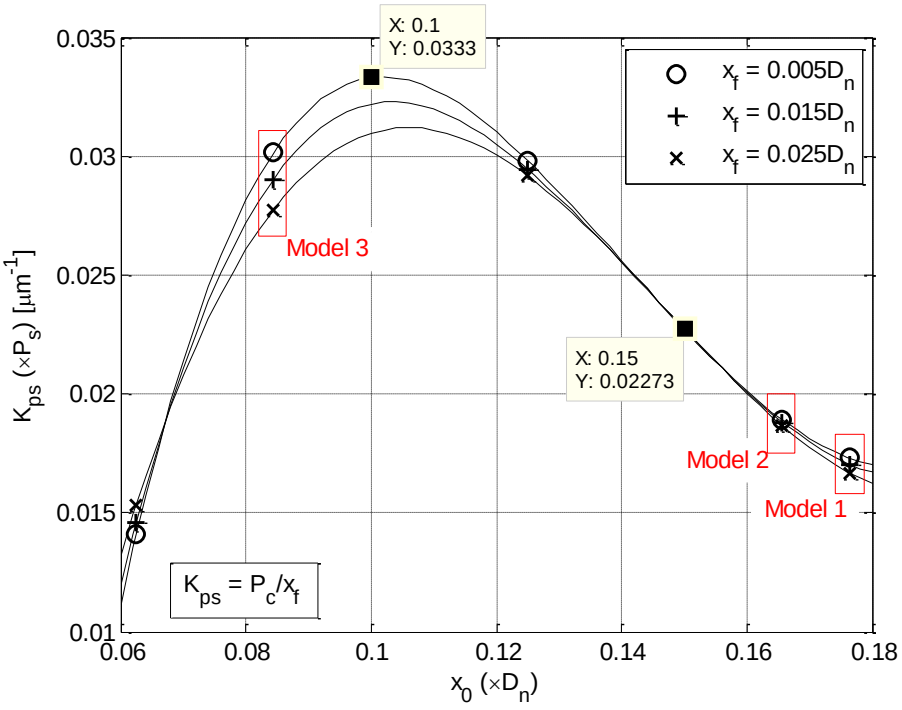

Figure 3.22 – First stage pressure sensitivity analysis results

Figure 3.22 shows that Model 3 yields much better results than 1 and 2. But spline interpolation curves indicates that the maximum pressure sensitivity actually occurs around $x_0 = 0.1D_n$ for $x_f = 0$. To make the model more accurate compared to CFD results, $C_{D,v}$ value found previously as 0.9 is updated since it is actually a function of x_f. From the CFD analysis it found that at $x_0 = 0.1D_n$, $C_{D,v} \approx 0.75$. So, when the $C_{D,v}$ used with Model is updated to 0.75, $\tilde{x}_0$ is calculated as $0.1012D_n$.

Pressure sensitivity at this $\tilde{x}_0$ value is also calculated with CFD and it is found to be $0.0352P_s$, $0.0340P_s$ and $0.0322P_s$ at the x_f values of $0.005D_n$, $0.015D_n$ and $0.025D_n$, respectively. These values are consistent with the prediction of spline interpolation.

The value of 0.75 for $C_{D,v}$ also makes more sense than 0.9 since it is more consistent with the common knowledge that the discharge coefficients of sharp edged orifices range from 0.6 to 0.8. So the value of 0.75 will be used for $C_{D,v}$ in the final model. Final set of discharge coefficients are given in Table 3.11.

Table 3.15.

Table 3.13 – Final set of discharge coefficients

Variable	Value
$C_{D,f}$	0.733
$C_{D,n}$	0.816
$C_{D,v}$	0.750
$C_{D,e}$	0.700

$C_{D,v}$ is updated to increase the $\tilde{x}_0$ estimation accuracy of Model 3 so it is now even superior than models 1 and 2. But one could question this approach since $C_{D,n}$ of models 1 and 2 can be updated as well so they could match the performance of Model 1. The $\tilde{x}_0$ definition found with Model 1 in equation (3.17) can be equated to $0.1D_n$ and solved for $C_{D,n}$ to find the $C_{D,n}$ value that makes the Model 1 to lead to the same result as the CFD analysis yields, which actually is found as 1.06. This value is beyond the physical limits for a discharge coefficient which cannot be greater than 1. The same thing can be done with equation (3.25) of Model 2 to find that $C_{D,n}$ should be 0.994 this time which is just as unreasonable. Even if the physical meaning is disregarded, such a drastic change in $C_{D,n}$ would lead to other calculation errors such as flow rate estimation.

Another point arises from Figure 3.22 that should be taken into consideration is that pressure sensitivity changes as the flapper moves when x_0 is around $0.1D_n$, but it seems insensitive to flapper position when x_0 is around $0.15D_n$. This indicates that when the pressure sensitivity at $x_f = 0$ is maximized the linearity of the output with respect to flapper motion is adversely affected. By increasing x_0 towards $0.15D_n$ the

pressure sensitivity could be compromised in favour of linearity. So, there is a trade-off between the pressure sensitivity and linearity and for some cases the first stage design may need to be made carefully.

One could also question the necessity of the inclusion of the exit pressure into the model, which complicates things incredibly. To clarify this issue, definition of $\tilde{x}_0$ is found for Model 3 with $P_e = 0$ in equations (3.33) and (3.24) using the MATLAB code given in Appendix A. Result is found as;

$$\tilde{x}_0 = \frac{C_{D,f} C_{D,n} D_f^2 D_n}{4 C_{D,v} \sqrt{3\left(C_{D,f}^2 D_f^4 + C_{D,n}^2 D_n^4\right)}} \tag{3.35}$$

Substituting discharge coefficients with their respective values given in Table 3.13, equation (3.35) is reevaluated for different D_f values and results are given in Table 3.14.

Table 3.14 – $\tilde{\boldsymbol{x}}_{\boldsymbol{0}}$ values calculated with equation (3.35)

$\boldsymbol{D_f}$ $(\times \boldsymbol{D_n})$	$\tilde{\boldsymbol{x}}_{\boldsymbol{0}}$ $(\times \boldsymbol{D_n})$
0,5	0,0344
0,75	0,0708
1	0,105

On the other hand $\tilde{x}_0$ values for Model 3 with respect to D_e is plotted in comparison to the results in Table 3.14 in Figure 3.23. The figure shows that although the error rate increases as the fixed orifice diameter increases, equation (3.35) estimates $\tilde{x}_0$ pretty close to Model 3 if $D_e \geq 2D_n$. Since a practical servovalve is likely to have $D_e \geq 2D_n$, first stage model can be simplified by omitting exit pressure with a little loss in accuracy.

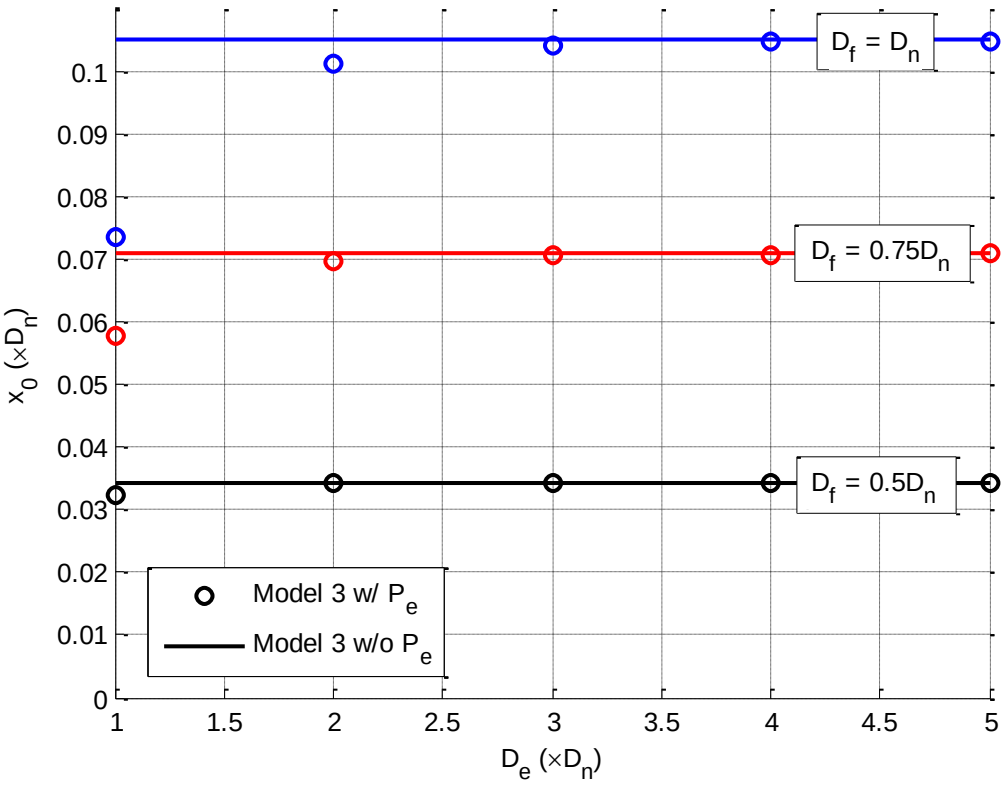

Figure 3.23 – Comparison of $\tilde{\boldsymbol{x}}_{\boldsymbol{0}}$ values found with or without $\boldsymbol{P_e}$

3.3. Spool Valve Model

Overlap and underlap conditions in a spool valve imply two different geometrical conditions; therefore, at least two different functions should be used to define the flow rates in these conditions. In order these two functions to form a continuous flow curve throughout the entire spool position range to overcome the non-smooth transition problem mentioned in Section 2.4, they must abide by the following constraints:

$$Q_{UL}|_{L=0} = Q_{OL}|_{L=0} \tag{3.36}$$

$$\left.\frac{\partial Q_{UL}}{\partial L}\right|_{L=0} = \left.\frac{\partial Q_{OL}}{\partial L}\right|_{L=0} \tag{3.37}$$

In equations (3.36) and (3.37), Q_{UL} and Q_{OL} are the flow rate functions for underlap and overlap conditions, respectively. Equation (3.36) implies that at the transition point ($L = 0$) two functions must yield the same result. Similarly, equation (3.37) implies that the slopes of both functions must be the same at this transition point. As the starting point, standard form of the well-known orifice equation that defines the flow rate through a spool valve in underlap condition is revisited;

$$Q_{UL} = C_{D,S} A \sqrt{\frac{2}{\rho}\Delta P} \tag{3.38}$$

To increase the accuracy, the orifice area "*A*" in equation (3.38) is defined as the truncated conical area between the spool and sleeve as shown in Figure 3.24.

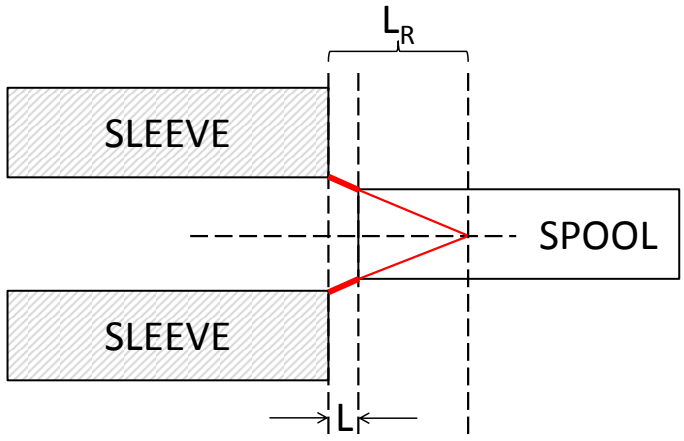

Figure 3.24 – The truncated conical area between the spool and the sleeve

The area of this truncated cone is given by

$$A = \pi(R + r)\sqrt{B^2 + L^2} \tag{3.39}$$

Since $R \approx r$, this area can be approximately written as follows:

$$A = 2\pi R\sqrt{B^2 + L^2} \tag{3.40}$$

Substituting this area expression into equation (3.38), Q_{UL} becomes

$$Q_{UL} = 2C_{D,s}\pi R\sqrt{B^2 + L^2}\sqrt{\frac{2}{\rho}\Delta P} \tag{3.41}$$

The function defining the flow rate in overlap condition is developed based on equation (1). The problem with equation (1) is the term with L being alone in the denominator. In order to prevent singularity as L approaches to zero, another term (M) is added to the denominator

$$Q_{OL} = \frac{\pi R B^3}{6\mu L + M}\Delta P \tag{3.42}$$

Note that in equation (2.28) the effect of eccentricity between the spool and sleeve is taken into account. According to equation (2.28) when the spool is 100% eccentric, the flow rate is 2.5 times more than it would be if it was concentric with the sleeve. But the effect of eccentricity becomes important only when $L \gg B$. As L approaches zero, the effect of eccentricity diminishes, becoming totally ineffective at zero-lapped condition. That is because the pressure drop is caused by the sudden decrease in the area through which the fluid passes, rather than the shear forces between the fluid and walls as it was if the fluid flowed through an annulus. When the spool comes to zero-lapped position, the eccentricity does not affect the amount of reduction in area. So the term representing eccentricity in equation (2.28) is neglected in equation (3.42), since the port lappings of a spool valve are assumed to deviate around zero with a small amount.

The definition of "M" in equation (3.42) is found by evaluating equation (3.43).

$$2C_{D,s}\pi RB\sqrt{\frac{2}{\rho}\Delta P} = \frac{\pi R B^3}{M}\Delta P \tag{3.43}$$

Solving for M yields

$$M = \frac{B^2\sqrt{2\rho\Delta P}}{4C_{D,s}} \tag{3.44}$$

Now that equation (3.36) is satisfied, equation (3.37) can be worked on to complete the model. The slope of equation (3.42) at $L = 0$ is found as

$$\left.\frac{\partial Q_{OL}}{\partial L}\right|_{L=0} = \left.\frac{6\mu\pi RB^3\Delta P}{\left(6\mu L + \frac{B^2\sqrt{2\rho\Delta P}}{4C_{D,s}}\right)^2}\right|_{L=0} = -\frac{48C_{D,s}^2\mu\pi R}{\rho B} \tag{3.45}$$

while the slope of equation (3.41) at $L = 0$ becomes

$$\left.\frac{\partial Q_{UL}}{\partial L}\right|_{L=0} = \left.\frac{2C_{D,s}\pi R\sqrt{\frac{2}{\rho}\Delta P}}{\sqrt{B^2 + L^2}}\right|_{L=0} = 0 \tag{3.46}$$

It is obvious that slopes of equations (3.41) and (3.42) when $L = 0$ cannot be equal in their current forms. But if the discharge coefficient $C_{D,s}$ is treated as a function of L rather than treating it as a constant this problem can be resolved. The importance of treating the discharge coefficient as a variable was already underlined in the literature [42]. Using variable$C_{D,s}$, the slope of equation (3.41) at $L = 0$ becomes

$$\begin{aligned}\left.\frac{\partial Q_{UL}}{\partial L}\right|_{L=0} &= \left(\frac{\partial C_{D,s}}{\partial L}2\pi R\sqrt{B^2 + L^2}\sqrt{\frac{2}{\rho}\Delta P} + \frac{2C_{D,s}\pi R\sqrt{\frac{2}{\rho}\Delta P}}{\sqrt{B^2 + L^2}}\right)_{L=0} \\ &= \left.\frac{\partial C_{D,s}}{\partial L}\right|_{L=0} 2\pi RB\sqrt{\frac{2}{\rho}\Delta P}\end{aligned} \tag{3.47}$$

By using the slope matching condition dictated by equation (3.37) one gets

$$\left.\frac{\partial C_{D,s}}{\partial L}\right|_{L=0} = \frac{24C_{D,0}^2\mu}{B^2\sqrt{2\rho\Delta P}} \tag{3.48}$$

Equation (3.48) is the rate of change of the discharge coefficient at $L = 0$ for a spool valve control port. A discharge coefficient definition satisfying equation (3.48) provides a continuous flow curve at all spool positions. But since equation (3.48) cannot be solved analytically, the function defining the discharge coefficient is found by fitting a function on the data from CFD analyses.

It is reported in the literature that the discharge coefficient is a function of Reynolds number and the orifice geometry [7]. The Reynolds number is defined as

$$Re = \frac{\rho V L}{\mu} \tag{3.49}$$

where L is the characteristic length of the subject geometry. The characteristic length of the annular orifice investigated here is the radial clearance B shown in Figure 2.7.

Furthermore, the velocity definition $\sqrt{2\Delta P/\rho}$ of standard orifice equation can be used to estimate the velocity V before the flow takes place. After these modifications the Reynolds number estimation becomes

$$Re^* = \frac{B\sqrt{2\rho\Delta P}}{\mu} \tag{3.50}$$

Computational fluid dynamics analyses for 200 different design points are conducted in order to characterize $C_{D,S}$. Design points are obtained by varying B, ρ, ΔP, and μ of equation (3.50), to calculate flow rates for each case. The results are substituted into equation (3.41) at $L = 0$ and equation (3.41) is solved for $C_{D,S}$. This process is repeated using different turbulence models and wall functions in the CFD solver to determine which model demonstrates best performance by comparing $C_{D,S}$ versus Re^* graphs.

All analyses are carried out in 2D axisymmetric domains shown in Figure 3.25 using Fluent's parametric analysis capability. Figure 3.26 shows the details around the radial clearance of a sample grid that has 6217 cells with minimum orthogonal quality of 82.8% and maximum aspect ratio of 1.66. Grids with similar quality are

used in all CFD analyses conducted in the analyses. Some details about mesh generation and solution are given in Table 3.11.

Table 3.15 – Calculation details for spool valve discharge coefficient analyses

Minimum num. of cells across any gap	14
Growth rate	1.04
Maximum face size	200 µm
Convergence criteria	Residuals to drop below 10^{-5}
Pressure-Velocity coupling scheme	Coupled
Discretization scheme	Second order upwind for all equations
Maximum iteration	1000
Mesh adaption	Every 50th iteration
Max. level of refinement for adaption	2
Adaption method	Cells with at least 10% of max. velocity gradient

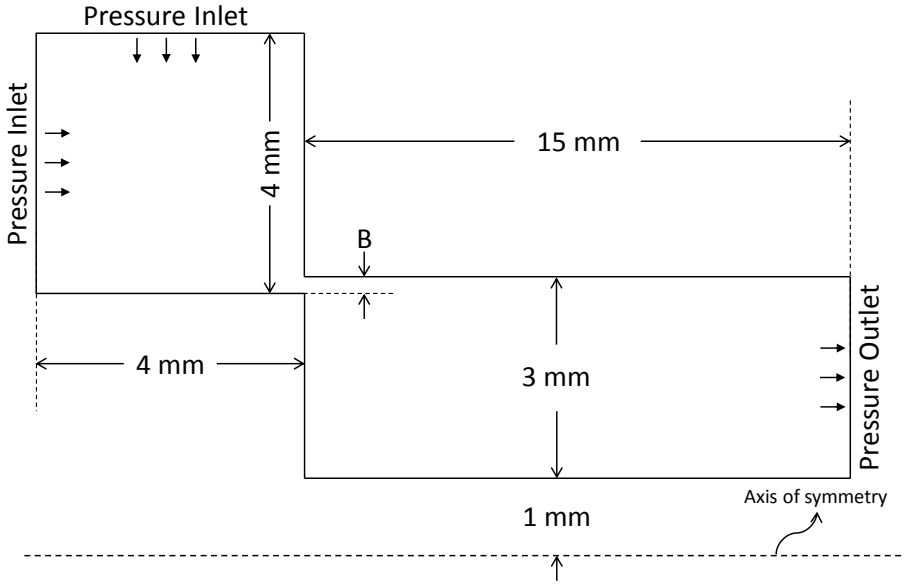

Figure 3.25 – Details of analysis domain

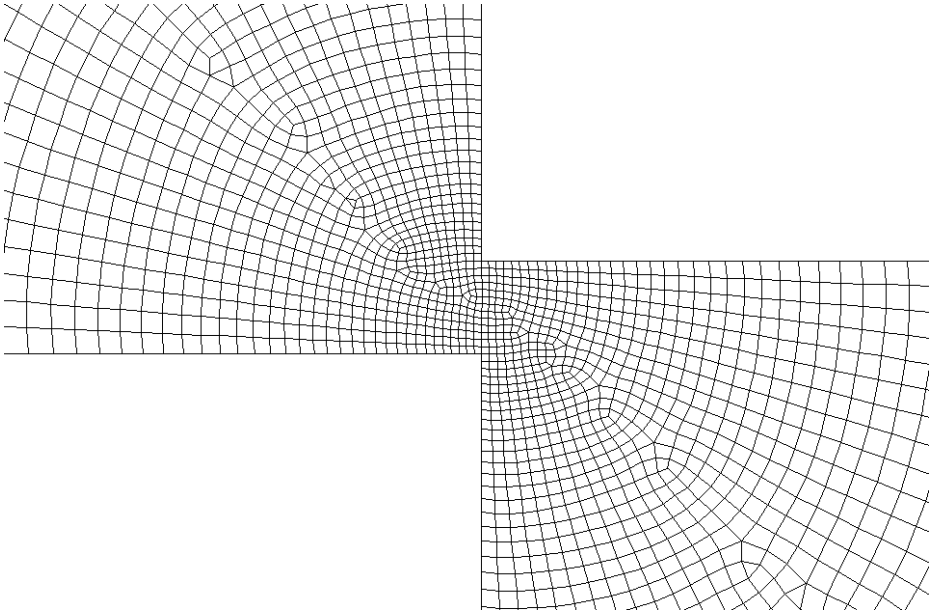

Figure 3.26 – Details around the radial clearance in a sample grid

Each turbulence model-wall function combination yields a unique discharge coefficient curve as given Figure 3.27. As shown in Figure 3.27, the laminar solution is also obtained for low Reynolds numbers for comparison. It is known in the literature that the use of scalable wall functions at low Reynolds numbers is likely to yield inaccurate results [54]. It is apparent that solutions with scalable wall function resulted in lower flow rate estimations comparing to laminar solution. So, it is decided that the use of scalable wall function is inappropriate for the purposes of our study.

On the other hand, the $C_{D,0}$ curve obtained using RNG k–ε + Enhanced Wall Treatment combination is physically unrealistic because of the two local maxima it possesses. Therefore, from the two k–ω solutions which showed very similar performance to each other, the discharge coefficient curve of shear stress transport (SST) k–ω solution is used as a reference to develop a mathematical model.

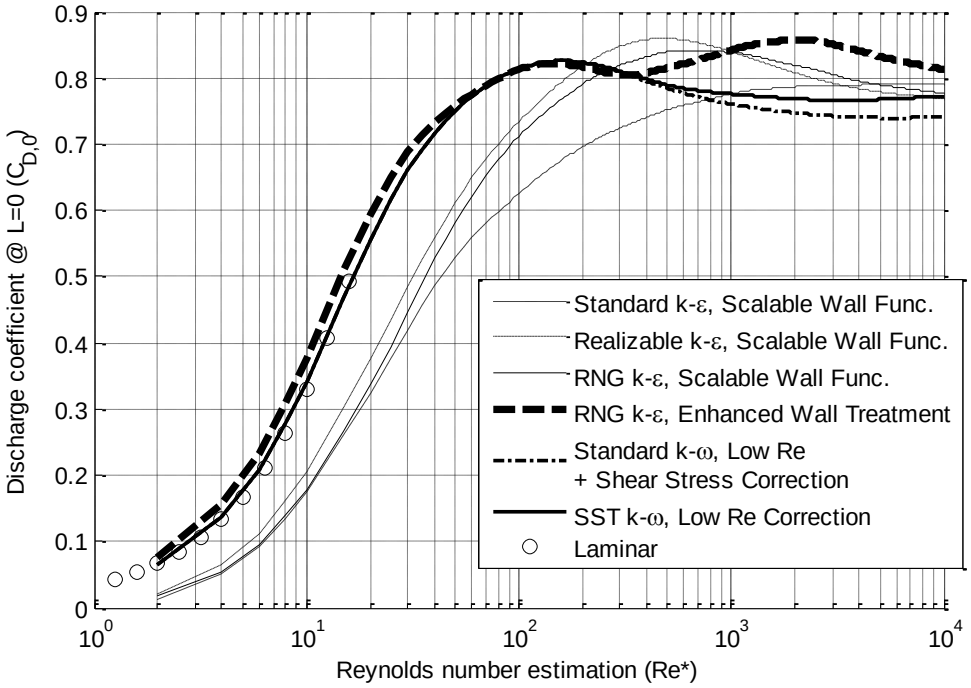

Figure 3.27 – Comparison of discharge coefficient versus Reynolds number estimation curves obtained using different turbulence model and wall function combinations

Similar works in the literature studying the discharge coefficient on spool valves are examined to check the degree of agreement. Posa et al. conducted numerical analyses on 2D axisymmetric spool valve geometry, very similar to the analyses in this work [41]. They provided a very detailed report on their work in terms of the geometric dimensions, fluid properties, and boundary conditions that were used. Using the same parameters with theirs, a set of CFD analyses are conducted using SST k–ω turbulence model as opposed to their direct numerical solution approach. The comparison of the results is given in Figure 3.28.

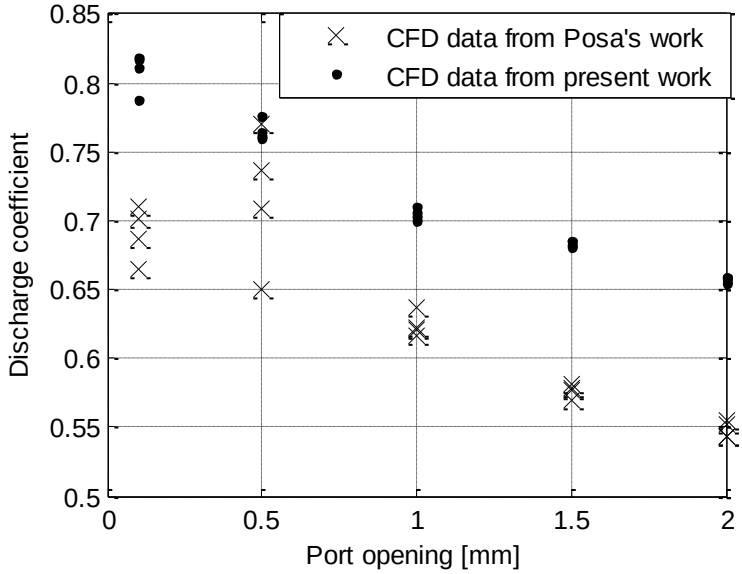

Figure 3.28 – Comparison of discharge coefficient data in the paper of Posa et al. to the ones obtained by SST k–ω turbulence model. Different discharge coefficients for same port openings are obtained by using different flow rates.

Figure 3.28 shows the discharge coefficients found using SST k–ω are consistently higher than the ones found in [41]. In another work by Pan et al. [40], even lower discharge coefficients are reported. So it can be said that there is no common agreement on the discharge characteristics of spool valves in the literature yet. One should consider this fact before using the models provided in such works.

A mathematical function is fitted to the $C_{D,0}$ curve obtained from SST k–ω solution and given in Figure 3.27. This function is given in equation (3.51), and its performance is illustrated in Figure 3.29 comparing to CFD data.

$$C_{D,0} = \frac{0.77\left(\widetilde{Re}^4 + \widetilde{Re}\right)\exp\left(-0.09\widetilde{Re}^{-0.3}\right)}{\widetilde{Re}^4 - 3.6\widetilde{Re} + 7.2} \tag{3.51}$$

where

$$\widetilde{Re} = \log(Re^* + 1) \tag{3.52}$$

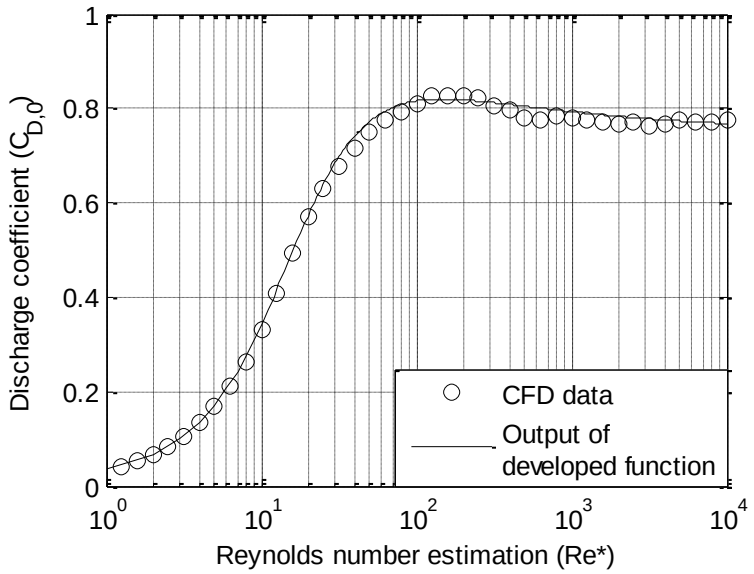

Figure 3.29 – Comparison of discharge coefficient data obtained by SST k–ω turbulence model and output of the fitted function

It should be noted that CFD analysis presented here is only conducted for $L = 0$. Therefore, discharge coefficient estimations here are named as $C_{D,0}$. If the spool is moved so the orifice is underlapped, then the geometry changes. Since $C_{D,s}$ is a function of geometry too, there should be a term in the $C_{D,s}$ expression to reflect the changes in the geometry.

The general shape of the orifice between the spool and sleeve for $L < 0$ with the parameters defining it is shown in Figure 3.30.

In order to study the effects of θ in Figure 3.30 on $C_{D,s}$, a separate set of CFD analyses are conducted again using SST k–ω turbulence model. The graph of the resulting data is shown in Fig. 12.

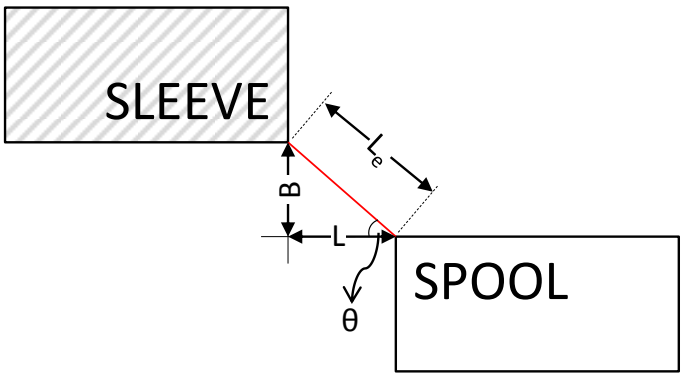

Figure 3.30 – Parameters which are used to define the underlap condition

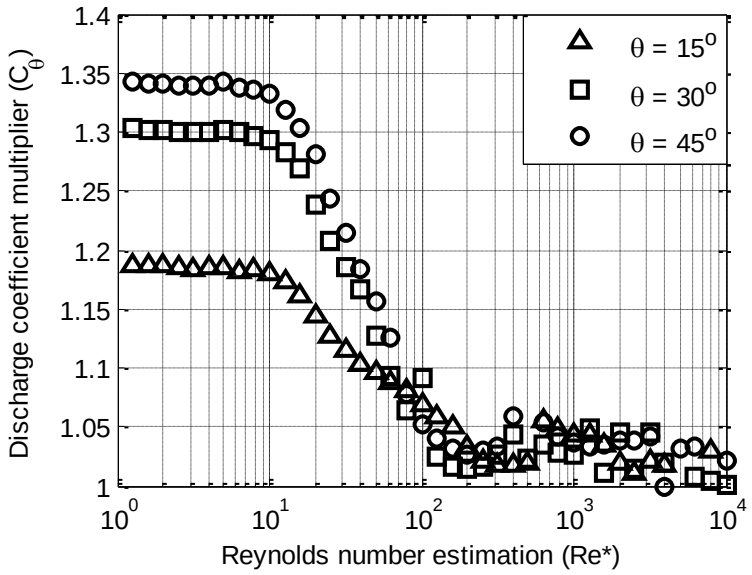

Figure 3.31 – C_θ curves obtained from CFD analyses

C_θ in Figure 3.31 is the ratio of the discharge coefficient at a certain L value to the $C_{D,s}$ estimation if $L = 0$ with the other parameters fixed;

$$C_\theta = f\left(\theta, \widetilde{Re}\right) = \frac{C_{D,s}}{C_{D,0}} \tag{3.53}$$

In the analyses, θ is varied with constant L_e and the Reynolds number estimation given in equation (3.50) is updated as $L_e\sqrt{2\rho\Delta P}/\mu$ so that the Reynolds number estimation is kept constant as θ changes. A function is developed that would reflect

the effect of the changes in θ on C_θ based on the data for $Re^* < 10$ and given in the following equation:

$$C_\theta = 1 + (C_\theta|_{\theta=45^\circ} - 1)\frac{\sin\theta + \cos\theta - 1}{\sqrt{2} - 1} \tag{3.54}$$

Comparison of the results of equation (22) to CFD data is given in Figure 3.32.

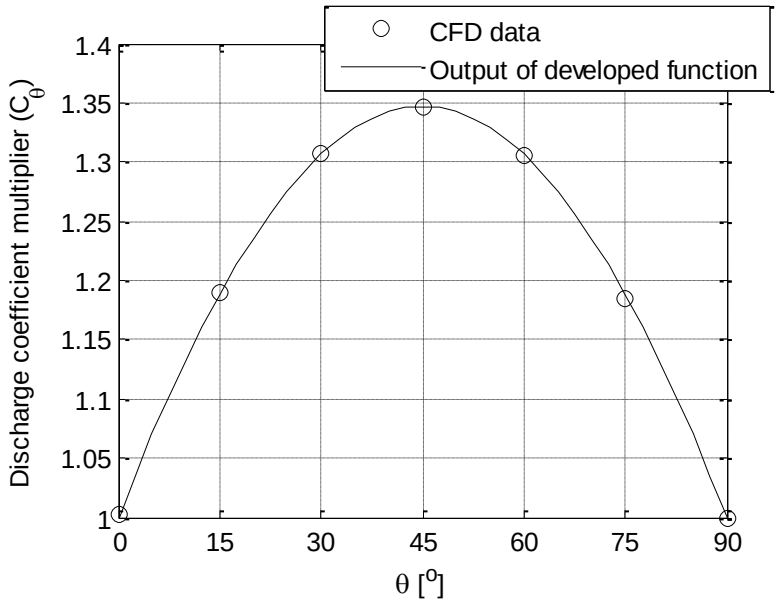

Figure 3.32 – Change in C_θ with respect to θ for $Re^* < 10$

Note that to be able to use equation (22), C_θ at $\theta = 45°$ must be known. So, one final function to calculate $C_\theta|_{\theta=45^\circ}$ is developed based on the data shown in Figure 3.31;

$$C_\theta|_{\theta=45^\circ} = 1.34 - 0.31\tanh\frac{\widetilde{Re}^5}{20} \tag{3.55}$$

Thus, the C_θ function takes its final form as follows

$$C_\theta = 1 + \frac{\left(0.34 - 0.31\tanh\frac{\widetilde{Re}^5}{20}\right)(\sin\theta + \cos\theta - 1)}{\sqrt{2} - 1} \tag{3.56}$$

A comparison of the results of equation (3.56) and data in Figure 3.31 is given in Fig. 14.

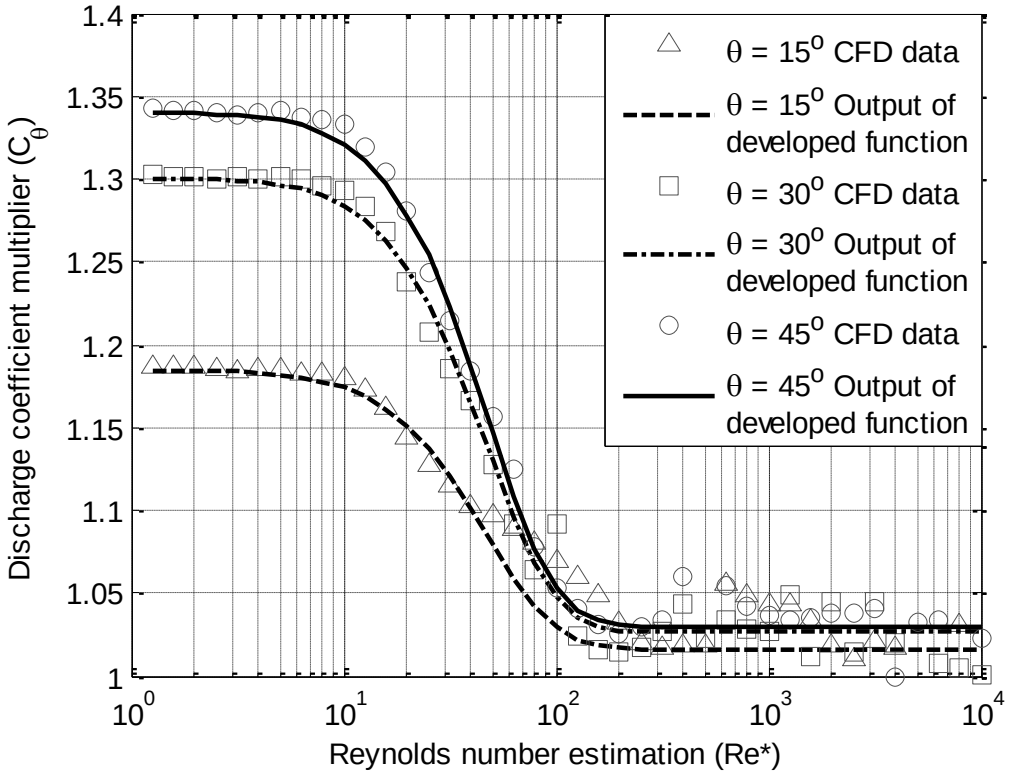

Figure 3.33 – Comparison of developed $\boldsymbol{C_\theta}$ function to CFD data

At this point, the model for the calculation of flow rate at the orifices of a spool valve is completed and given as equation (3.57).

$$Q = \begin{cases} \dfrac{\pi R_s B^3}{6\mu L + \dfrac{B^2\sqrt{2\rho\Delta P}}{4C_{D,0}}}\Delta P & if\ L \geq 0 \\ 2C_{D,s}\pi R_s\sqrt{B^2+L^2}\sqrt{\dfrac{2}{\rho}\Delta P} & if\ L < 0 \end{cases} \tag{3.57}$$

where

$$C_{D,s} = C_{D,0}C_\theta$$

$$C_{D,0} = \frac{0.77\left(\widetilde{Re}^4 + \widetilde{Re}\right)\exp\left(-0.09\widetilde{Re}^{-0.3}\right)}{\widetilde{Re}^4 - 3.6\widetilde{Re} + 7.2}$$

$$C_\theta = 1 + \frac{\left(0.34 - 0.31 \tanh \frac{\widetilde{Re}^5}{20}\right)(\sin\theta + \cos\theta - 1)}{\sqrt{2} - 1}$$

$$\widetilde{Re} = \log(Re^* + 1)$$

$$Re^* = \frac{\sqrt{B^2 + [\min(L, 0)]^2}\sqrt{2\rho\Delta P}}{\mu}$$

The model is evaluated on a four-way spool valve with dimensions given in Figure 3.34 to demonstrate its performance.

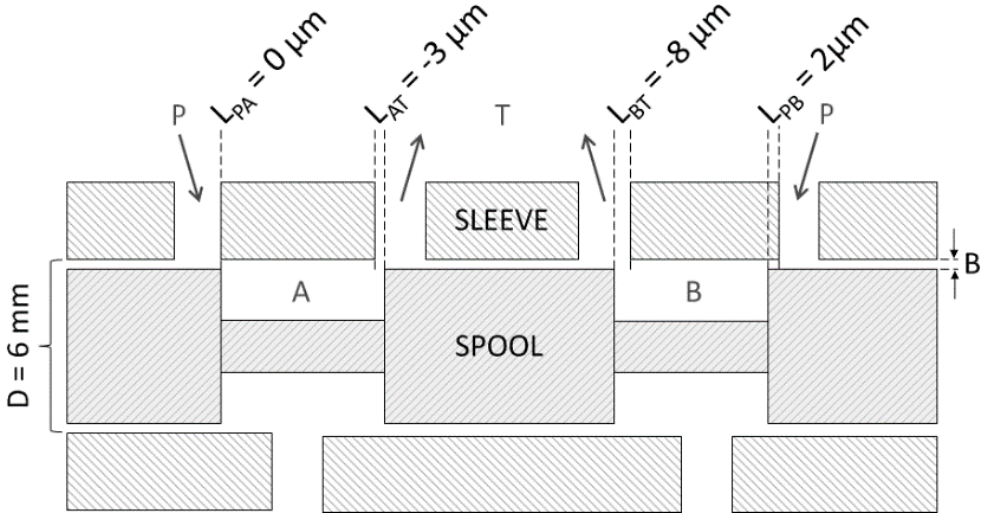

Figure 3.34 – The valve geometry which is used to test final model

Calculations are carried out with 100 bar inlet pressure, 1000 kg/m^3 fluid density, and 0.02 Pa·s dynamic viscosity. The position range of the spool is assumed to be ±100 µm. A CFD analysis is conducted for the same case using SST k–ω turbulence model, and the results are compared in Figure 3.35.

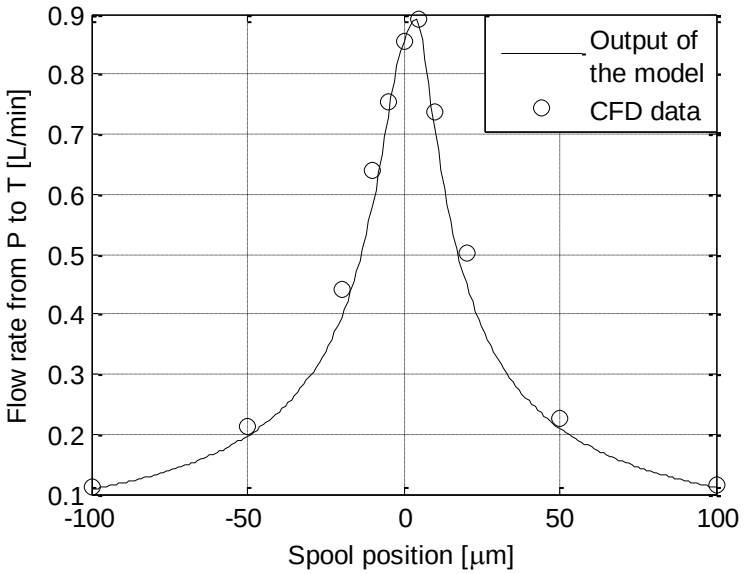

Figure 3.35 – Flow rate estimations of developed model and CFD analysis

It is seen in Figure 3.35 that the model yields consistent results with CFD data especially around null position. As the spool deviates from null position, the model suggested yields a lower flow rate estimation than the CFD analysis. This is due to the addition of an artificial term (M) to the denominator of equation (2.28). Apparently, this term makes the resistance of the annular orifice at overlap condition be calculated higher than it is in CFD analyses. A percentage error map between CFD data and model's result across the entire spool position range of Figure 3.35 is given in Figure 3.36. It is seen in Figure 3.36 that the maximum error of the model in this case is 13.3%. Since each port of the valve is modeled as a separate orifice, and these orifices are connected in serial to form the overall valve simulation, the model would work with a similar performance for any imaginable port configuration.

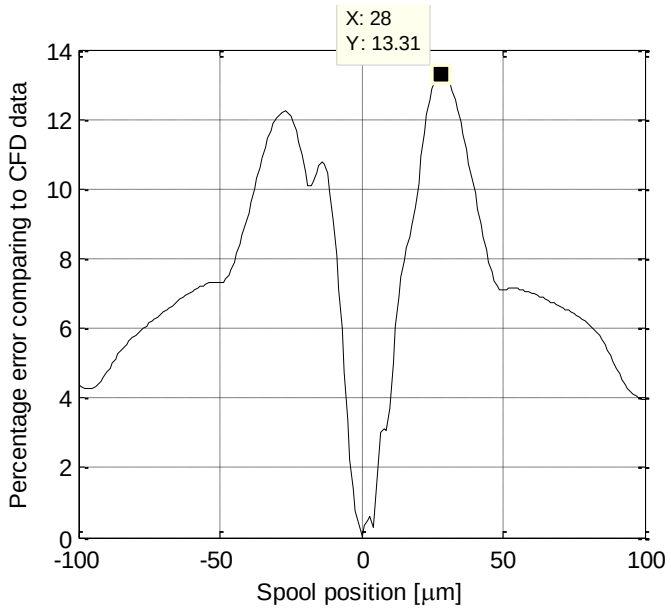

Figure 3.36 – Error map of the model's output for the test case

To validate the model, test data for pressure sensitivity and leakage flow of a spool valve are compared with model's estimation. A picture of tested spool and sleeve is shown in Figure 3.37. The cross-sectional view from their computer-aided design model is shown in Figure 3.38. The spool diameter is 5.020 mm, and there are four control ports corresponding to each spool land, located through the sleeve circumference with equal distances. Each control port has a nominal width of 3.1 mm.

The tests are performed using the configuration shown in Figure 3.39. In the figure, the inlet and outlet pressure data of valve are obtained from the pressure sensors 1 and 2. Pressure data at load ports are obtained from the pressure sensors 3 and 4. The flow rate through the valve during the test is obtained from flow meter 5.

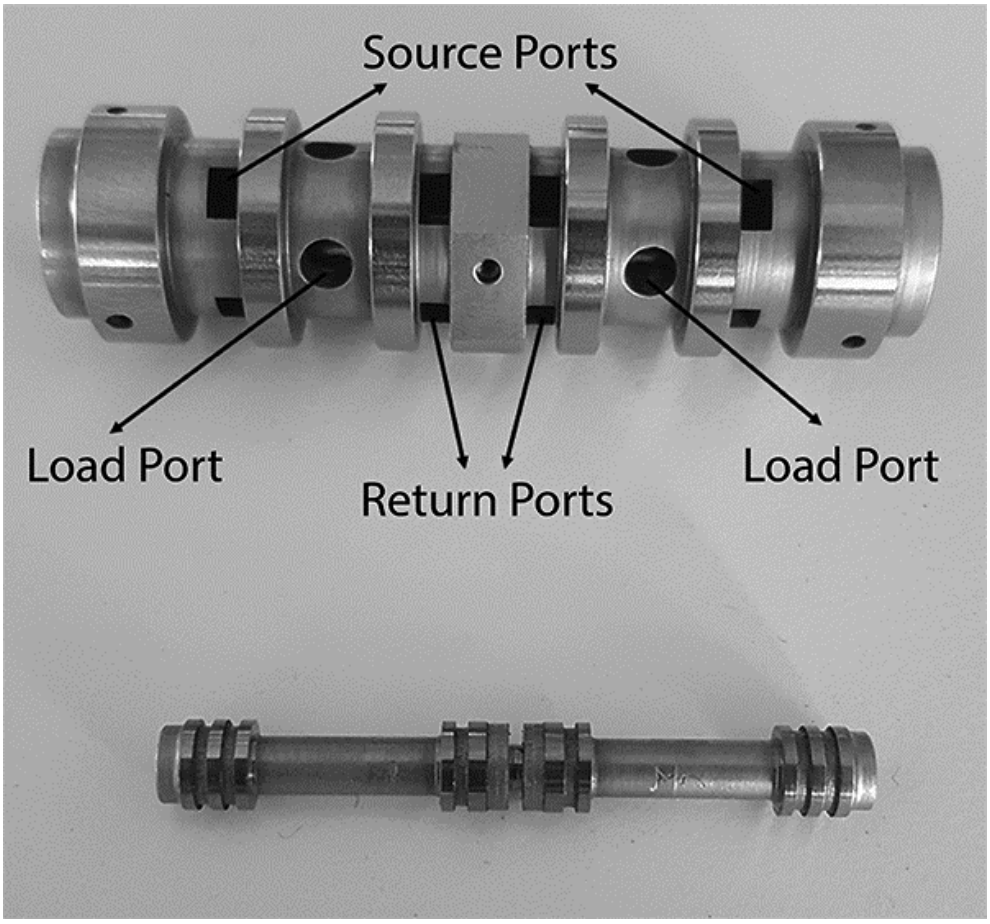

Figure 3.37 – A picture of the spool and the sleeve used in the tests

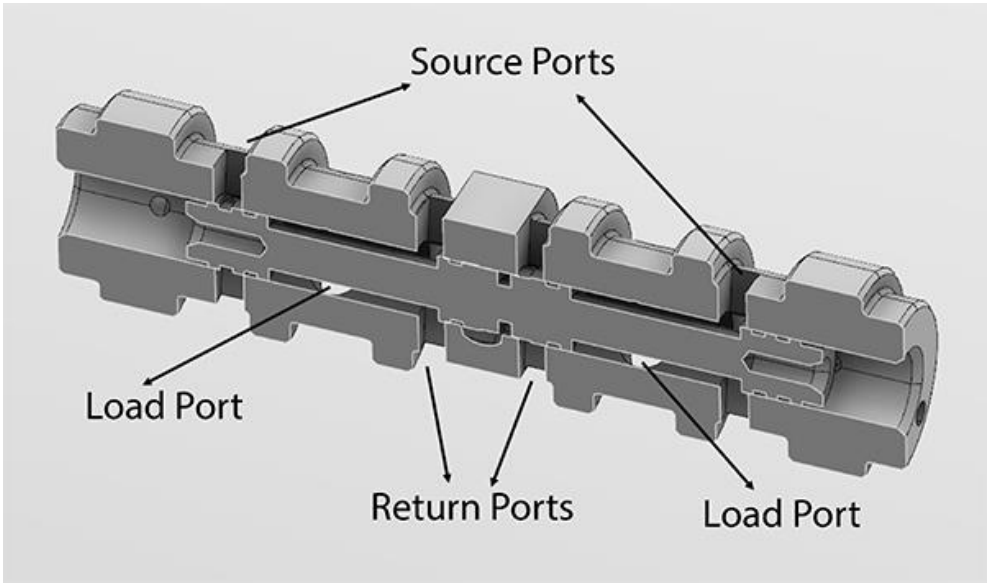

Figure 3.38 – Cross-sectional view of tested spool valve's computer aided design model

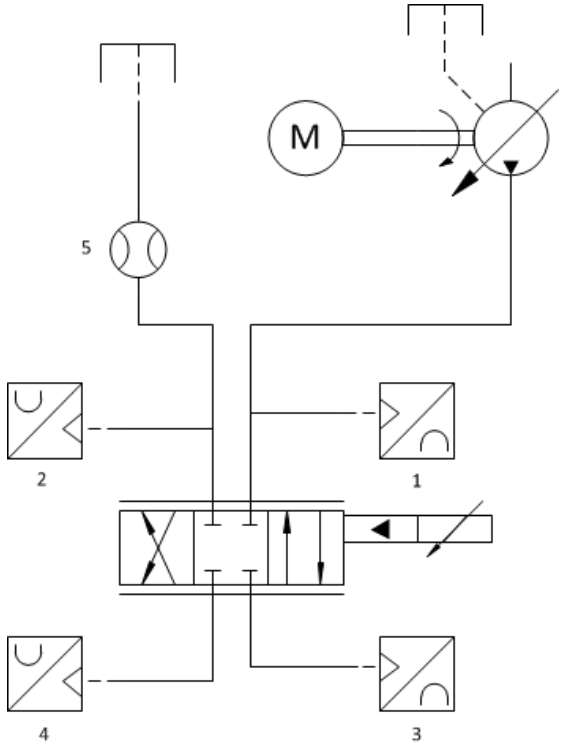

Figure 3.39 – Hydraulic scheme of test configuration

A series of tests are performed at 165 bar of source pressure while MIL-H-5606 hydraulic oil is used. The equipment used in the test system are given in Table 3.16.

Table 3.16 – Equipment used in spool valve test system

Equipment	Company	Model	Details
Pump	Parker	PV080	Variable Displacement, 80cc
Flowmeter	VSE	VSI 0.1	10000 pulse/L resolution, 10 L/min maximum flow rate
Pressure sensor	Trafag	NAH 8254	0-60 bar measurement range, accuracy ≤ ±%0.125 FS
LVDT	Applied Measurements	AML/M	< ±%1.0 FS Non-Linearity < ±%0.1 FS Repeatability
Data acquisition system	National Instruments	9219 universal input module on cRIO-9064 chassis	50 Hz noise rejection mode: 130 ms conversion time
Working fluid	Belgin Oil	MIL-H-5606	@20 °C

During the tests, the spool is driven from one end to change its position, and an linearly variable differential transformer is used to measure the position at the other end. The valve is tested with the configuration suggested in [55], i.e., load ports are blocked, the pressure at valve chambers and the flow rate from valve to reservoir are measured. Under these conditions, the valve has a maximum leakage flow rate of 0.487 L/min and pressure sensitivity (i.e., slope of load pressure curve at null position) of 29.96 bar/µm. The model's prediction of radial clearance and port lappings of the valve are given in Table 3.17.

Table 3.17 – Model's prediction of valve dimensions

B (µm)	L_{PA} (µm)	L_{AT} (µm)	L_{PB} (µm)	L_{BT} (µm)
3	-4	-5	6	6

With these dimensions, model calculates a maximum leakage flow rate of 0.485 L/min and pressure sensitivity of 29.96 bar/µm. Since there are no available measurement results for the distances between sleeve ports and spool lands, model's prediction for these dimensions are presented but not verified. Nevertheless, the model estimates the leakage flow rate and pressure sensitivity with very high accuracy capturing the shape of related curves on Figure 3.40 and Figure 3.41 very well at the same time. Therefore, the developed model shows promise for utilization in geometric tolerance determination of spool valves.

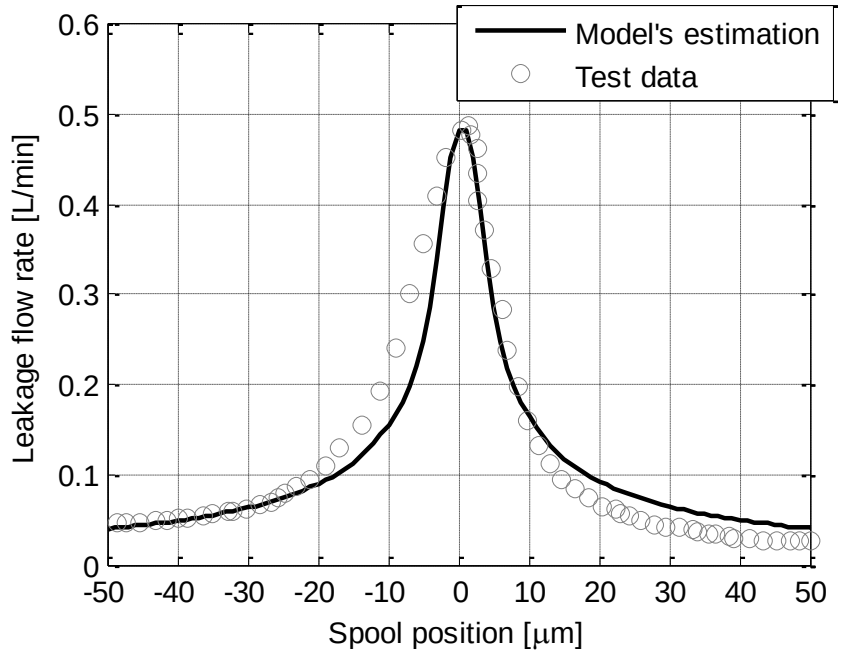

Figure 3.40 – Comparison of model's leakage flow rate estimation to test data

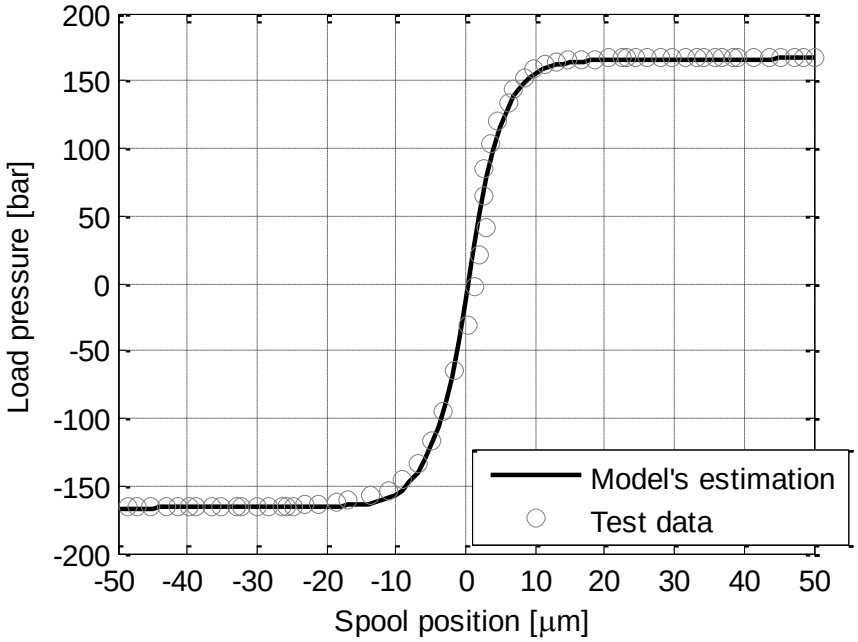

Figure 3.41 – Comparison of model's load pressure estimation to test data

CHAPTER 4

COMPLETE DYNAMICAL MODEL OF A DOUBLE STAGE NOZZLE-FLAPPER SERVOVALVE

A nonlinear model in Simulink® environment using SimScape® blocks reflecting all the nonlinearities that are observed in a is developed in this chapter.

Ouline of the nonlinear model created in SimScape is shown in Figure 4.1.

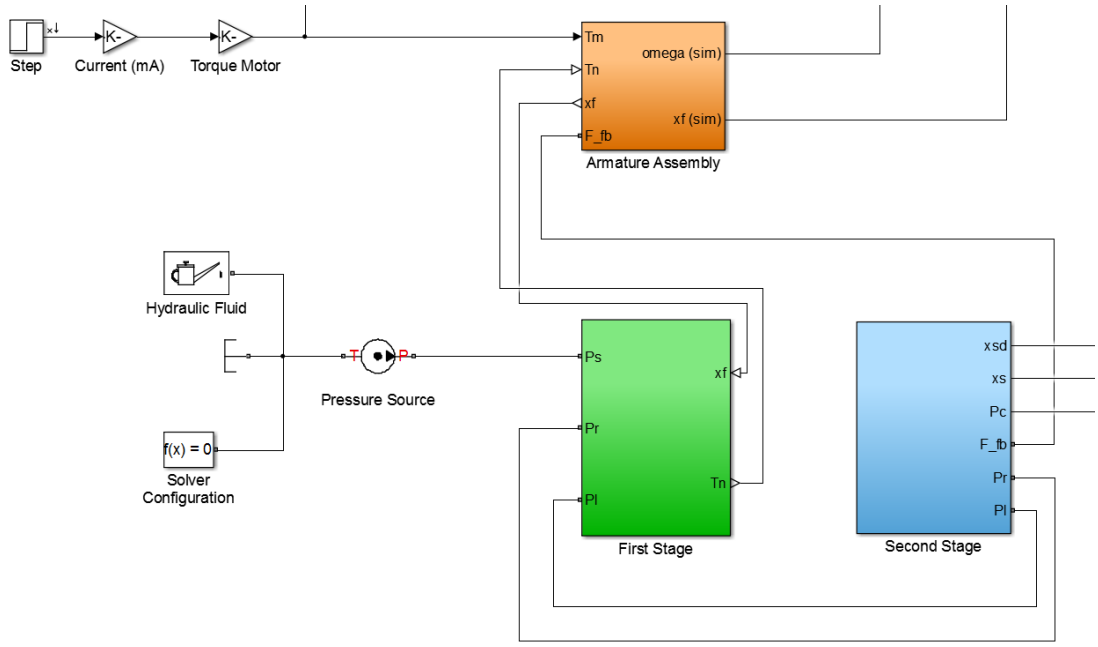

Figure 4.1 – Outline of the SimScape Model

As seen in the figure, valve is split into three main components: Armature Assembly, First Stage and Second Stage. Torque input to the armature assembly is calculated by multiplying the input current by a torque constant k_T, while the supply pressure P_s is supplied to the system using a "Pressure Source" block which supplies constant pressure during the simulation.

In what follows the three main components are explained in detail.

4.1. SimScape Model

4.1.1. Armature Assembly

Armature assembly component takes the torque produced by the torque motor (T_m), the torque produced by the fluid jets ejected from the nozzles (T_n) and spool position information to calculate the force applied by the feedback spring as its inputs. Outputs of it are the flapper speed/position and the force from the feedback spring applied to the spool in the second stage. Details of the component are shown in Figure 4.2.

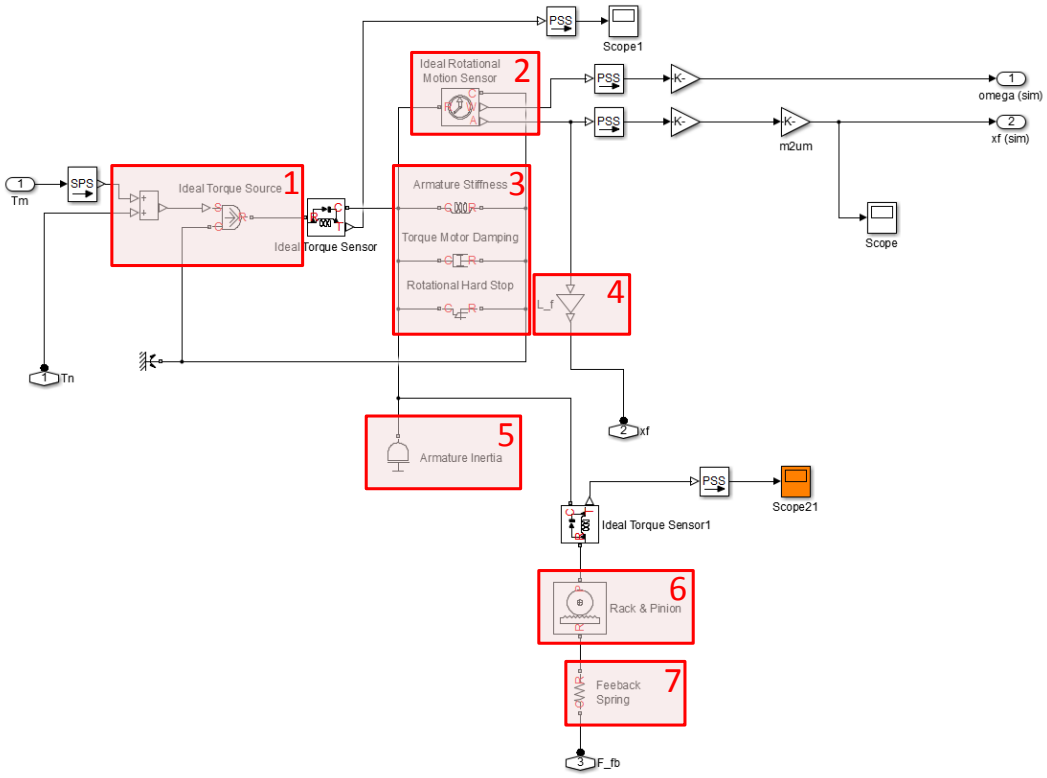

Figure 4.2 – Details of Armature Assembly Component

What is done in Armature Assembly component is basically the solution of equation (2.1) which is given below for reference.

$$T_{tm} + T_n = J_{FS}\ddot{\theta} + c_{FS}\dot{\theta} + k_{fb}L_f(x_s + x_f) + k_{ft}\theta \quad (2.1)$$

Referring to Figure 4.2, the torque summation "$T_{tm} + T_n$" is carried out and supplied to an "Ideal Torque Source" block at (1). At (3), the flexure tube stiffness (k_{ft}) and armature damping (c_{FS}) are introduced to the system, and a hard stop is used to simulate the case in which the flapper hits against the nozzles. The motion sensor at (2) extracts the position and velocity information of the inertia defined at (5) to supply to the first stage and for monitoring. At (4) the rotational position of flapper is converted to translational position at the nozzle axis (refer to Figure 2.3) to be supplied to First Stage component. At (6) rotational properties of the armature assembly is converted translational properties via a "Rack & Pinion" block to couple its information with spool's so the force exerted by the feedback spring on both the armature and spool can be calculated. At (7) this information is supplied to a "Translational Spring" block to simulate the feedback spring. The torque sensors seen in the figure are used for monitoring purposes.

4.1.2. First Stage

First Stage component takes the flapper position information from Armature Assembly, calculates spool control pressures and the torque caused by the fluid jets from the nozzles on the flapper for a given supply pressure. The details of the component are shown in Figure 4.3.

Referring to Figure 4.3, the flapper position information is taken in and curtain areas for each nozzle branch is calculated at (1). At (2), supply pressure information is taken in and fed to the fixed orifices at each branch. At (3), pressure information between the fixed orifices and nozzles are fed to second stage. At (4) the nozzles are simulated as shown in Figure 3.11. At (5) the equations (2.2) to (2.6) are carried out

to calculated T_n, and the information is supplied to Armature Assembly component. At (6) the flow rate from the nozzles to the servovalve outlet port measured and monitored, which is the "tare flow" of the servovalve [55]. Finally, the drain orifice of the servovalve (refer to Figure 3.21) is simulated at (7) using a Fixed Orifice block.

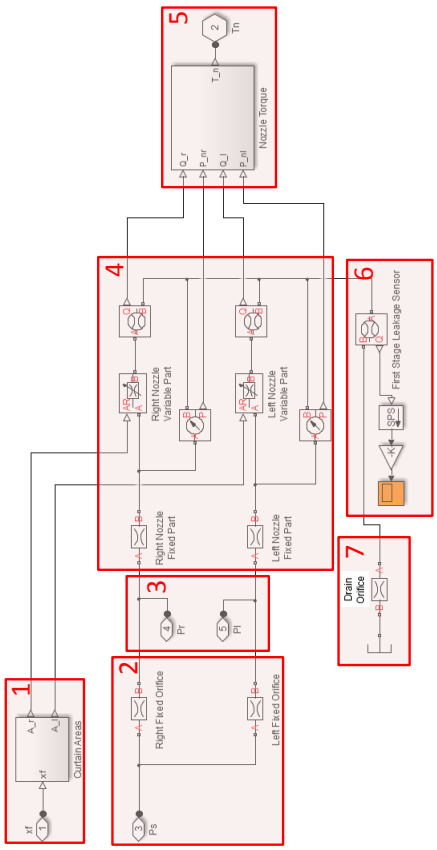

Figure 4.3 – Details of First Stage Component

4.1.3. Second Stage

Second Stage component takes control pressures and feedback spring force as its inputs and calculates simulates spool motion and flow through the spool ports. Its details are shown in Figure 4.4.

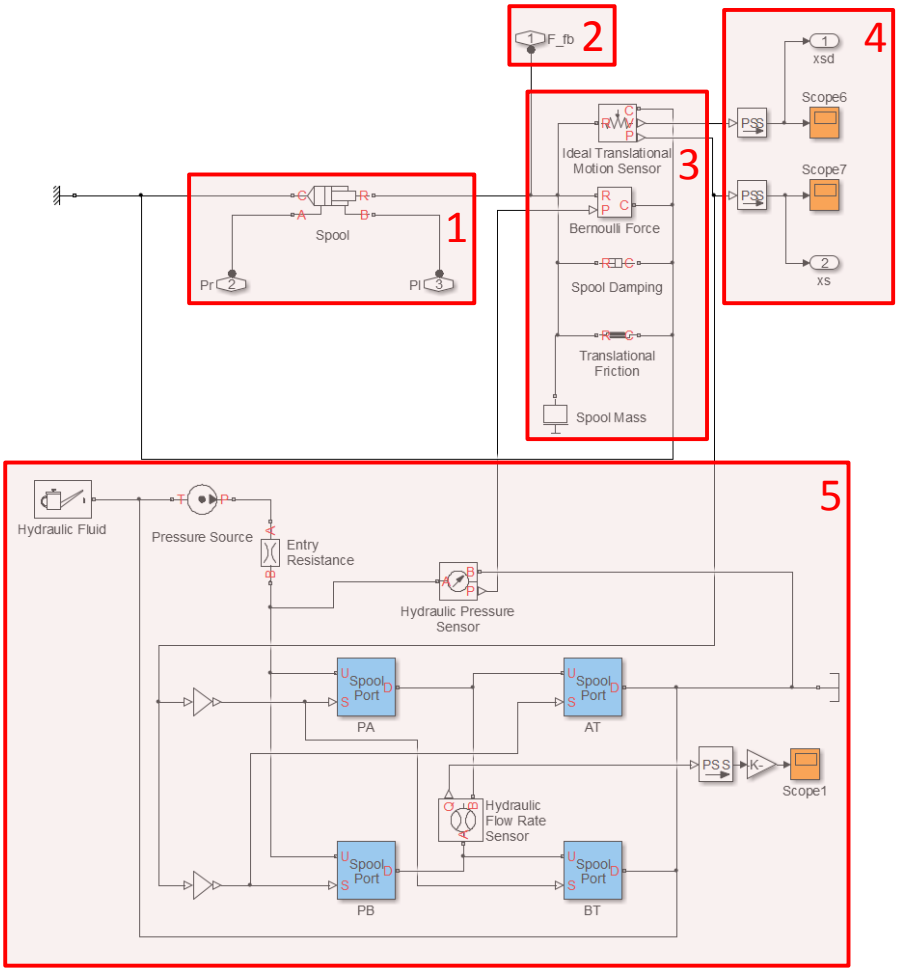

Figure 4.4 – Details of Second Stage Component

In Figure 4.4, the pressures information from both branches of the first stage in imported and used for calculation of the driving force of the spool at (1). Here the spool is modeled using a "Double-Acting Hydraulic Cylinder" block which lets the information of spool area, maximum stroke and dead volumes at the ends so it can account for the compressibility of the fluid. The mass, damping and friction on the spool are defined at (3). The damping coefficient is defined as it is given in equation (2.25). Also, the Bernoulli force is defined at (3) as a spring having a stiffness coefficient given in equation (4.5). A custom block is created to simulate the Bernoulli force with the source code given in Appendix C. If equation (2.24) was

used directly to define the Bernoulli force it would cause convergence problems at $x_s = 0$ since x_s is in the denominator.

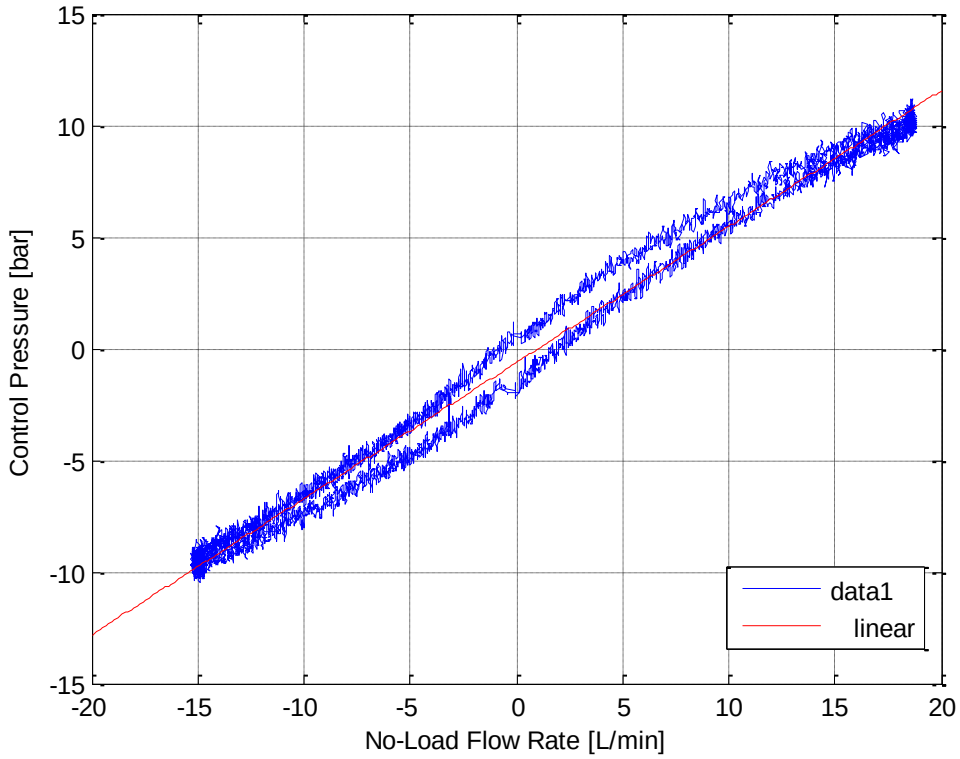

Figure 4.5 – Relation between the control pressure and no-load flow rate

The test data given in Figure 4.5 shows the relation between the control pressure and no-load flow rate of a double stage servovalve. The hysteresis in the test data is caused by the hysteresis of the sensors, and orientation difference of the spool when moving in different directions. Since control pressure creates the force on the spool which balances the Bernoulli force, and there is a linear relation between the flow rate and the spool position, the data in Figure 4.5 can be used to interpret the relation between the spool position and Bernoulli force. According to the data, Bernoulli force can be modeled as a spring force;

$$F_B = k_B x_s \tag{4.1}$$

One may prefer to model the Bernoulli force as a linear spring force accepting a small amount of error. If the control pressure and spool position data is available k_B can be defined as a constant;

$$k_B = \frac{P_{c,max} A_s}{x_{s,max}} \tag{4.2}$$

where $x_{s,max}$ is the maximum spool position and $P_{c,max}$ is the control pressure at $x_{s,max}$. Alternatively, it can be estimated as it is done in equation (2.39);

$$k_B = 0.77 C_{D,s}^2 w (P_s - P_L) \tag{4.3}$$

Equation (4.3) can be further simplified substituting $C_{D,s}$ with its asymptotical value 0.77 as found in equation (3.51). Also, since servovalves' performance tests are conducted theoretically in no-load flow condition (see Section 4.1.3 for more detail), load pressure P_L can also be neglected to finally get;

$$k_B = 0.46 w P_s \tag{4.4}$$

The 0.46 constant in the formula can be named as Bernoulli force constant (K_B) and can be tuned for different valves if the test data is available. Also, one should be aware of the fact that the pressure drop across the second stage can actually never be equal to supply pressure P_S on the entire working range since there will be a certain amount of resistance to flow at the entry, the exit and the line connecting the load ports of the servovalve in reality. This effect is the reason that the slope of the curve in Figure 4.5 decreases as the flow rate increases. So, in reality, equation (4.4) should be expressed in terms of pressure drop across the second stage instead of supply pressure;

$$k_B = K_B w \Delta P_{SS} \tag{4.5}$$

Turning back to Figure 4.4, at (2) spool motion information is shared with First Stage component to be used for the calculation of feedback spring force. At (4) spool position and velocity is exported for monitoring purposes.

At (5), the spool ports are simulated to calculate the flow rate during the simulation. Each “Spool Port” component here simulates one of the four ports of the 4-way valve used in the second stage of double-stage servovalve. Name convention for the ports is as shown in Figure 1.1. The Spool Port component is compiled as a custom SimScape block using the model derived in Section 3.2.1 with the source code given in Appendix D. The user interface of the block is shown in Figure 4.6, where the user must enter the spool radius, radial clearance, the ratio of sleeve perimeter which is used as port (see Figure 3.37) and the lapping of the port at null position. The block has three connection ports as seen in Figure 4.4, where U and D are the ports for upstream and downstream flow lines and S is the position signal. Positive position signal closes the port while negative one opens it.

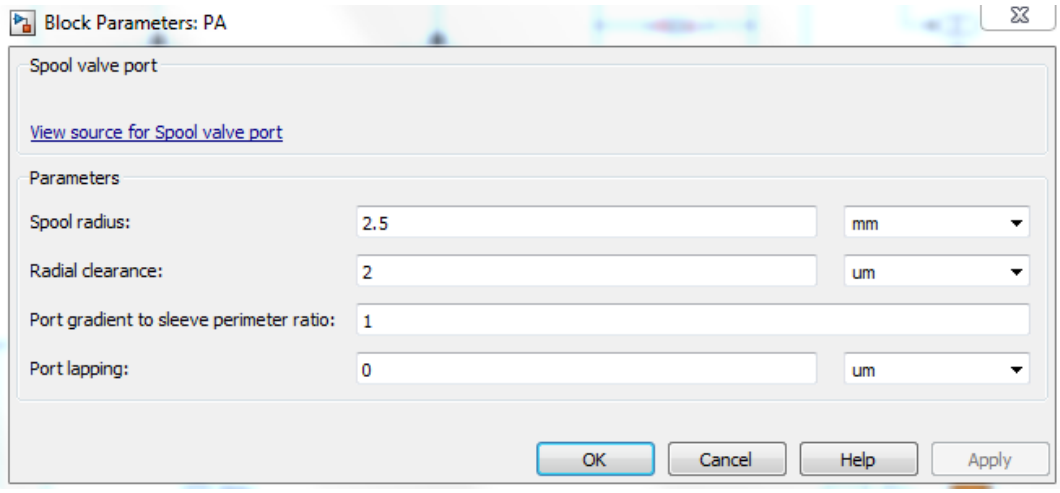

Figure 4.6 – Custom spool port block user interface

Although both stages of a servovalve is supplied from the same pressure source (i.e., pump), a separate “Pressure Source” block is used in the simulation for Second Stage since the numerical stability could not be sustained when the same pressure source with the First Stage is used.

The ports are connected in the “No-Load Flow Test” configuration in Figure 4.4 as per SAE ARP 490 [55]. Hydraulic scheme of this configuration is also showed in Figure 4.7.

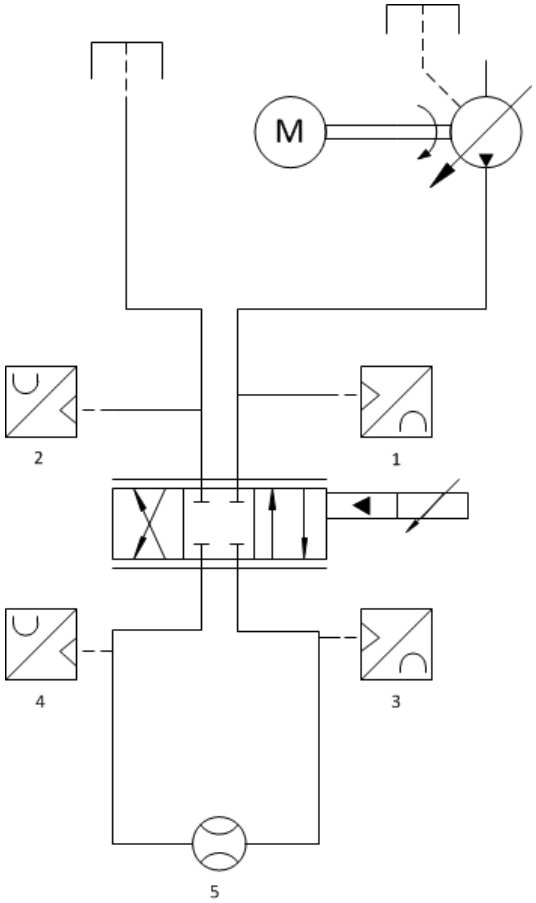

Figure 4.7 – No-Load Flow test configuration hydraulic scheme

In this configuration the output characteristics of the servovalve such as maximum no-load flow rate, linearity or null region can be quantified. The other test configuration is “Leakage Flow Test Configuration”, the hydraulic scheme of which is shown in Figure 3.39. A servovalves pressure sensitivity (or pressure gain) and maximum internal leakage is measured using that configuration. The model shown in Figure 4.4 can easily be changed to leakage flow configuration by simply changing the flow rate sensor with a pressure sensor. Full list of performance metrics of a servovalve and their definitions are given in detail in SAE ARP 490 [55].

Also note that in Figure 4.4 there is a fixed orifice at the upstream of the spool ports used to account for the flow resistances of the inlet and the outlet of the servovalve manifold. It is possible to use separate fixed orifices for inlet and oulet but a single

orifice is preferred here combining the effects of both to keep the number of components low. A servovalve must be so designed that pressure drop is kept as low as possible between the inlet port and spool ports, or the spool ports and the return port. Otherwise the pressure drop across the second stage cannot be kept constant throughout the working range and this affects the output linearity adversely.

4.2. Simulation of Moog 31 Series Servovalve

To test the created model, parameter set of a commercial valve, namely Moog Series 31 Nozzle-Flapper Servovalve is used. Parameters and output performance of this valve are made available by the manufacturer in [5] and given in Appendix E.

Despite the parameters are originally given in imperial units, they are converted to SI units and given in Table C.1. Note that armature related stiffness, damping and inertia parameters are given $^{Nm}/_{m}$, $^{Nm}/_{(m/s)}$ and $^{Nm}/_{(m/s^2)}$ to be used in direct calculation of the flapper states x_f, $\dot{x_f}$ and $\ddot{x_f}$. But the equations of motion of the model which is constructed for this study are based on armature rotation, not the flapper translation. Since the relation between the armature rotation and flapper position is given by $x_f = L_f\theta$, L_f must be determined in order to make the parameters compatible with the present model. L_f is not provided in the datasheet, but the external dimensions (Figure C.1) and a cross sectional view of the servovalve are given (Figure 4.8). Using the given information, L_f and L_s of the valve is approximated by determining the distances in pixels on Figure 4.8 and mapping them on a known dimension. This dimension is chosen to be the middle axis of torque motor connector and the lower end of the valve manifold, which is given as 34.8 mm in Figure C.1.

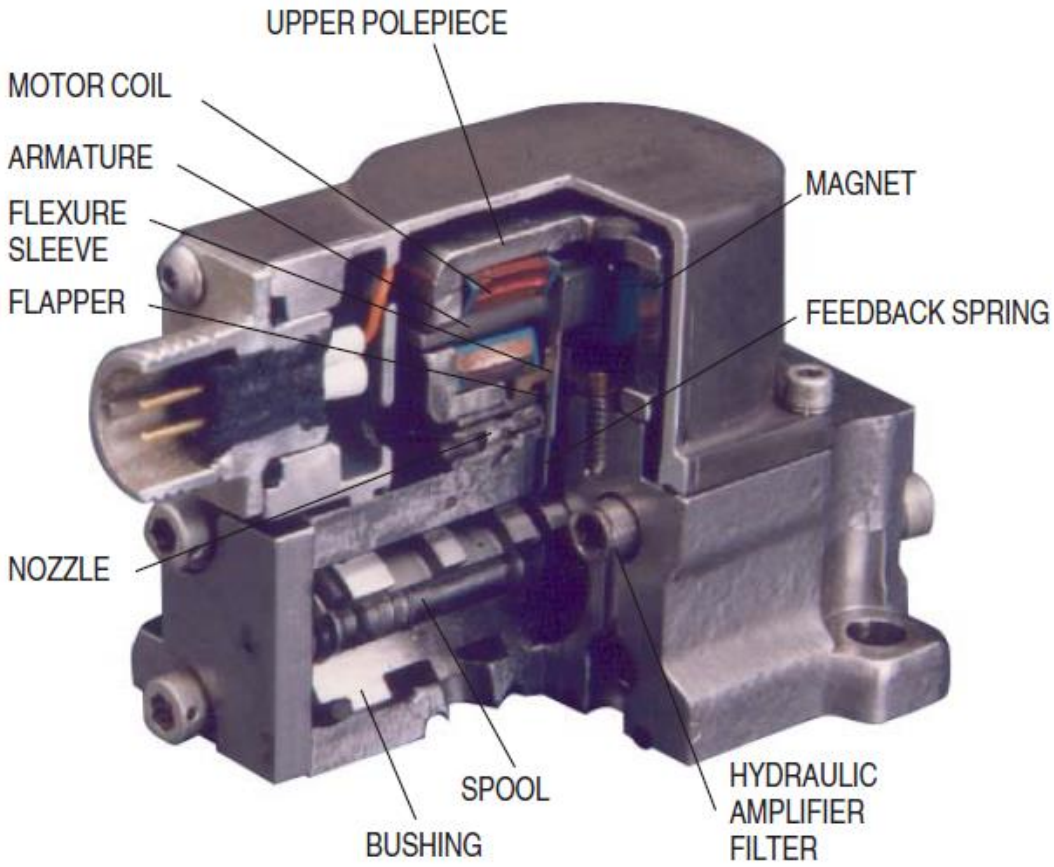

Figure 4.8 – Cross sectional view of Moog Series 31 Servovalve [4]

The related distances are found using the program WebPlotDigitizer [56]. The image that is imported to the program is given in Figure 4.9.

The distances measured are namely the connector middle line (which approximately coincides with armature middle line) to flexure tube base, to nozzle axis (see Figure 2.3), to spool axis and to manifold lower end. Since connector middle line to manifold lower end distance is known as 34.8 mm the other are interpolated according to that distance. The results are given in clearer view in Figure 4.10. Since Figure 4.10 is a schematic view the dimensions are not in correct scale on with the figure.

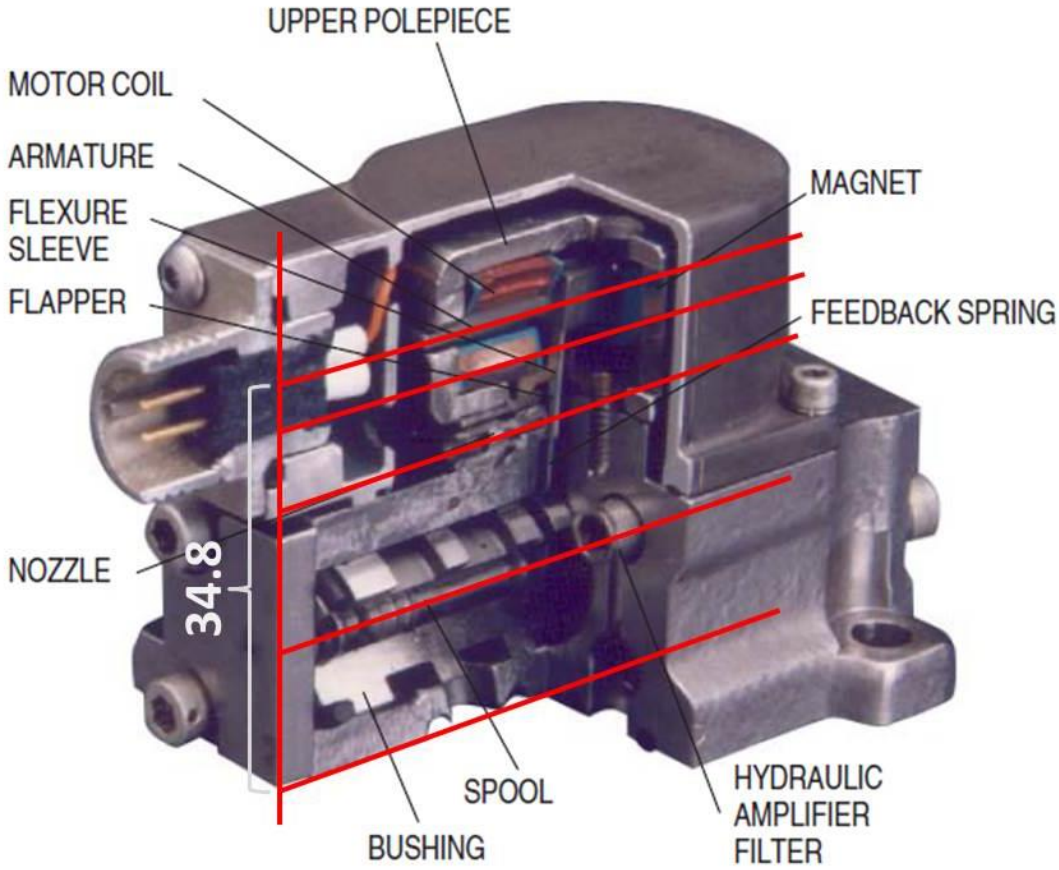

Figure 4.9 – The locations of the points of which the distances are found

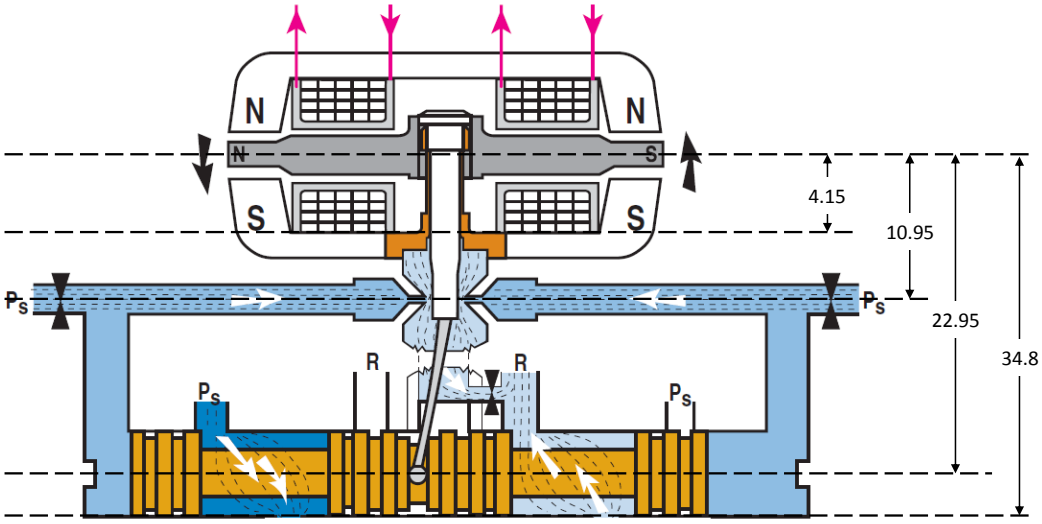

Figure 4.10 – Results of the measurement

Since the pivot point of the flapper should lie somewhere in the middle of the 4.15 mm dimension (see Appendix B), half of this dimension is subtracted from 10.95 and 22.95 to estimate L_f and L_s, which are found as 8.87 and 20.87 mm, respectively.

Now that L_f and L_s is known, armature related parameters can be transformed as given in Table 4.1.

Table 4.1 – Converted parameters

Parameter	Originally	Relation	Value
k_A	k_f	$k_A = k_f L_f$	4.53 N.m/rad
k_{fb}	k_w	$k_{fb} = k_w / L_s$	3560 N/m
b_A	b_f	$b_A = b_f L_f$	$6.3 \cdot 10^{-4}$ N.m/(rad/s)
J_A	J_f	$J_A = J_f L_f$	$1.74 \cdot 10^{-7}$ N.m/(rad/s^2)

The sleeve in Figure 3.37 is actually the sleeve of a Moog Series 31 Servovalve. Its rectangular ports' total width on one section, i.e., the port gradient w is measured as 12 mm. Spool weight is measured as 3 gr. The fixed orifice measured in Section 3.1 is also from a Moog Series 31 Servovalve, so assuming same diameter for nozzle exit and fixed orifice 200 μm is used for both dimensions. Also assuming 40 μm for x_0, 2 μm for B [57] and completely neglecting the spool damping as suggested in Section 2.3. The only parameter that is left undetermined is the area of the orifice which is used to simulate the resistance to low in the second stage apart from the metering ports. Since it is known that the valve provides 15.1 L/min control flow at $x_s = 381$ μm, the pressure drop can be found using equation (2.34);

$$\frac{15.1 \frac{L}{min}}{1000 \frac{L}{m^3} \cdot 60 \frac{s}{min}} = .77(12 \cdot 10^{-3} m)(381 \cdot 10^{-6} m) \sqrt{\frac{\Delta P}{860 \frac{kg}{m^3}}} \rightarrow \Delta P = 44\ bar$$

It is also given that this flow rate is obtained at 70 bar supply pressure, so the flow resistance of the valve manifold must cause a 26 bar pressure drop at 15.1 L/min flow rate. Therefore using standard orifice formula;

$$\frac{15.1\frac{L}{min}}{1000\frac{L}{m^3}\cdot 60\frac{s}{min}} = C_D A\sqrt{\frac{2}{860\frac{kg}{m^3}}(26\cdot 10^5\ Pa)} \rightarrow C_D A = 3.24\ mm^2$$

In the Fixed Orifice block used to account for manifold resistance in the simulation model, discharge coefficient C_D can simply be defined as unity and area A can be defined as 3.24 mm^2. With the area defining the entry resistance is determined, the complete set of parameters used in the simulation is become as given in Appendix F.

With these parameters spool position and control flow graphs are given in Figure 4.11.

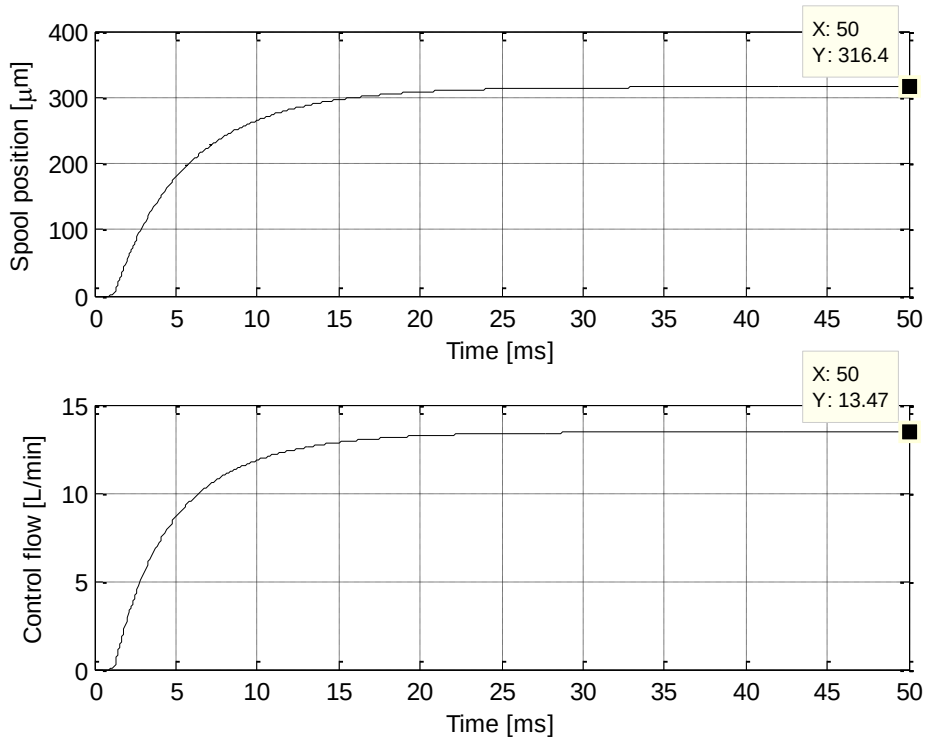

Figure 4.11 – Spool position and control flow rate graphs with initial parameter set

The simulation has underestimated the control flow by ~10% than the datasheet value 15.1 L/min. But note that the parameters given in datasheet are given for a much simpler linear model shown in Figure 4.12.

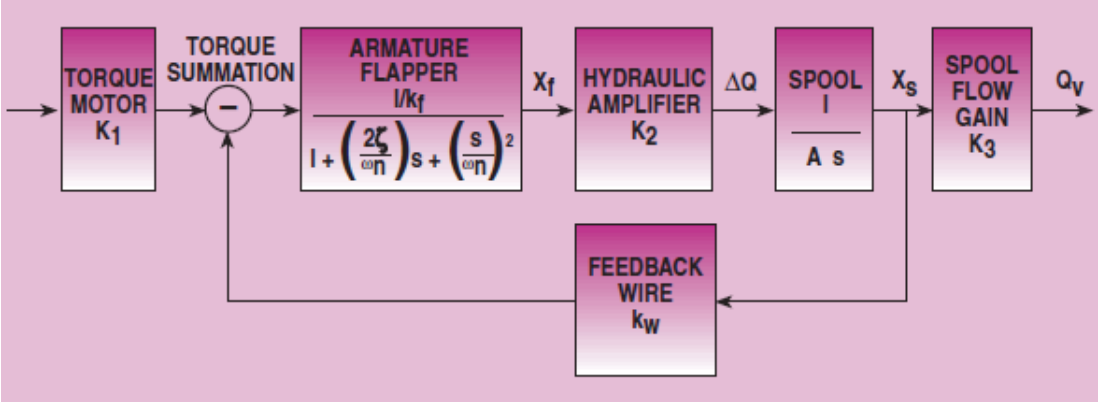

Figure 4.12 – The model suggested in Moog Type 30 Servovales catalogue [5]

The model shown in Figure 4.12 doesn't take many effects into consideration such as the torque applied by the nozzle jets on the flapper or the feedback springs effect on spool. These effects may not be significant when singled out, but their absence together can explain the 10% underestimation of the flow rate. It should also be considered that the parameters given in the datasheet are probably tuned for the model in Figure 4.12. Also, the parameters L_f and L_s are extracted from the picture of the valve (Figure 4.8), while D_n and x_0 are guessed based on assumptions. So, these parameters can be tuned with the constants of the present model to fit the available data. For this purpose, the parameters given in Table 4.2 are updated to the given values.

Table 4.2 – Updated parameters

Parameter	New value
D_n	235 µm
x_0	35 µm
L_f	9,85 mm
L_s	19,87 mm
k_{fb}	3300 N/m
K_B	0.45

With the updated parameters results becomes as shown in Figure 4.13.

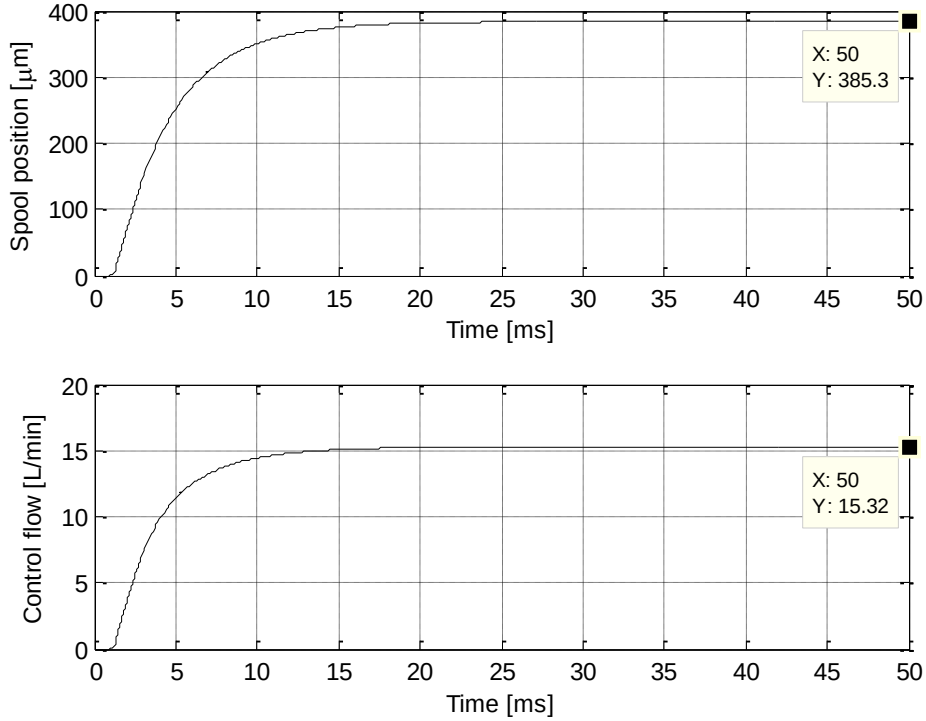

Figure 4.13 - Spool position and control flow rate graphs with updated parameter set

As shown in the figure, static spool position and control flow performance meets the datasheet values now. Bode plot of the valve is predicted as shown in Figure 4.14 with 210 bar supply pressure and ±25% of the full input (2.5 mA). It is seen that the -3 dB magnitude frequency is 77.4 Hz and -90° phase lag is at 337 Hz, which is given as >200 Hz in the data sheet.

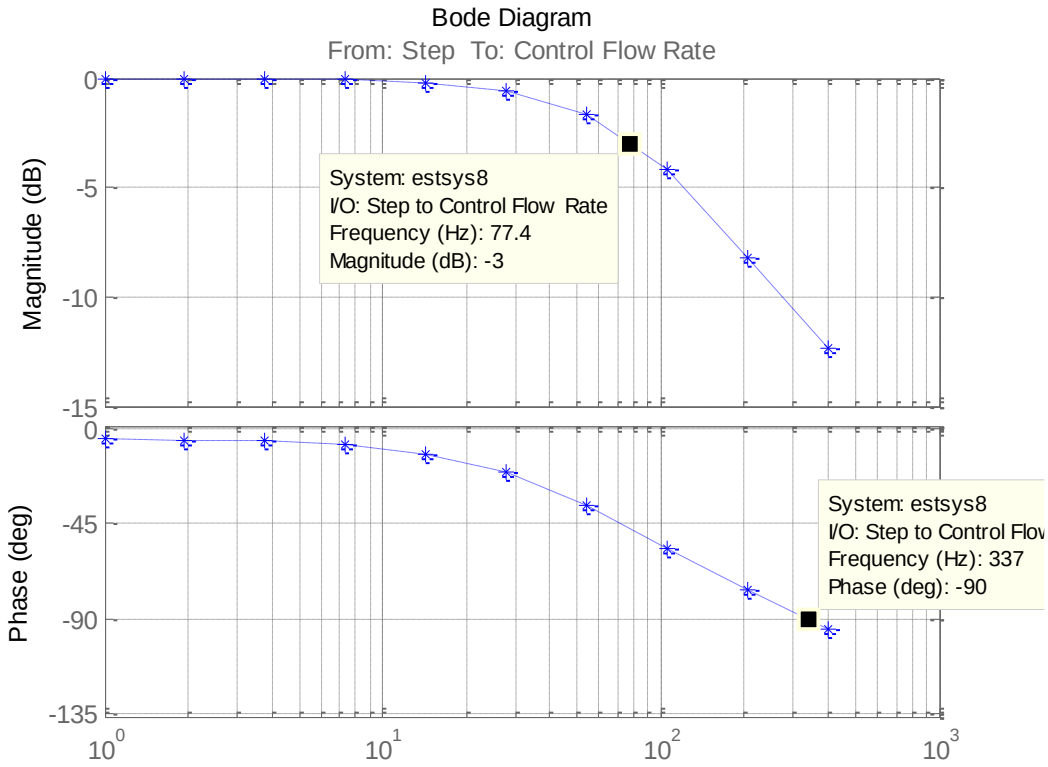

Figure 4.14 – Bode plot prediction with the updated parameters

The control flow curve with the new parameters is given in Figure 4.15. Maximum nonlinearity is calculated as 7% explained in SAE ARP 490. This value also is given in the datasheet as ≤7%. By switching to leakage flow test configuration as explained in Section 4.1.3, valves load pressure and spool leakage curves are also obtained and given in the figures Figure 4.16 and Figure 4.17. As seen in Figure 4.16, the load pressure increases to 40% of supply pressure in 0.2% of the rated current and the maximum spool leakage is 0.35 L/min which should be <1.2% and <1 L/min, respectively according to the datasheet. Note that all metering ports on the second stage are critically lapped in the simulation which is very hard to manage in reality. The tare flow of the valve is also obtained as 0.37 L/min which should be lower than 0.45 L/min again according to the datasheet. By changing all the parameters one can see the variations in the servovalve performance and this is the power of the developed simulation model. For example if all the metering ports were 5 μm overlapped, these graphs would become as shown in figures Figure 4.18 to

Figure 4.20. Note that overlapping the valve decreases its pressure sensitivity and creates a dead zone around null position in the no-load flow curve.

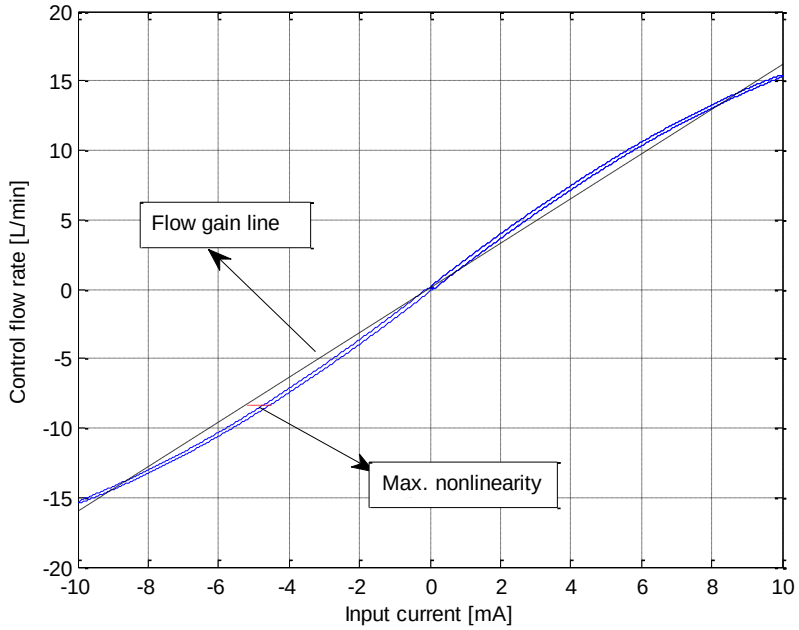

Figure 4.15 – Predicted no-load flow curve of Moog Series 31 Servovalve

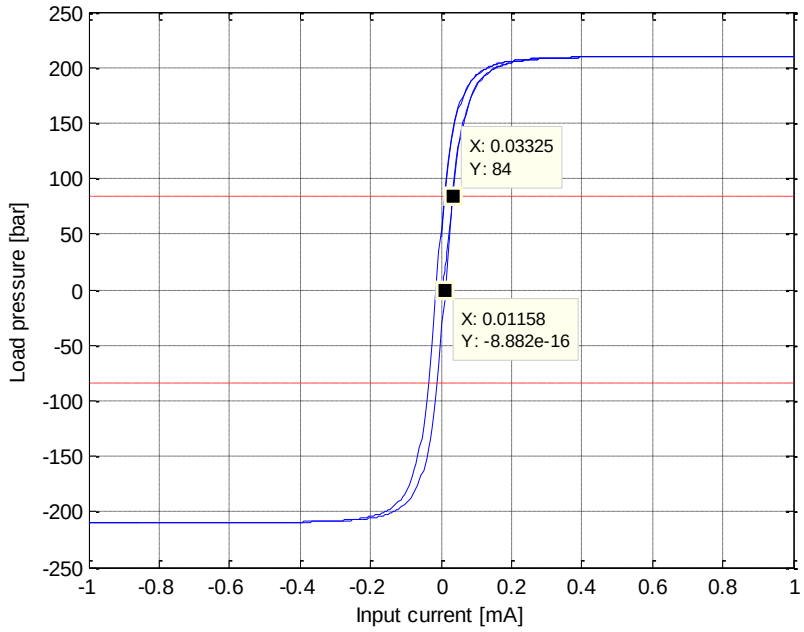

Figure 4.16 – Predicted load pressure curve of Moog Series 31 Servovalve

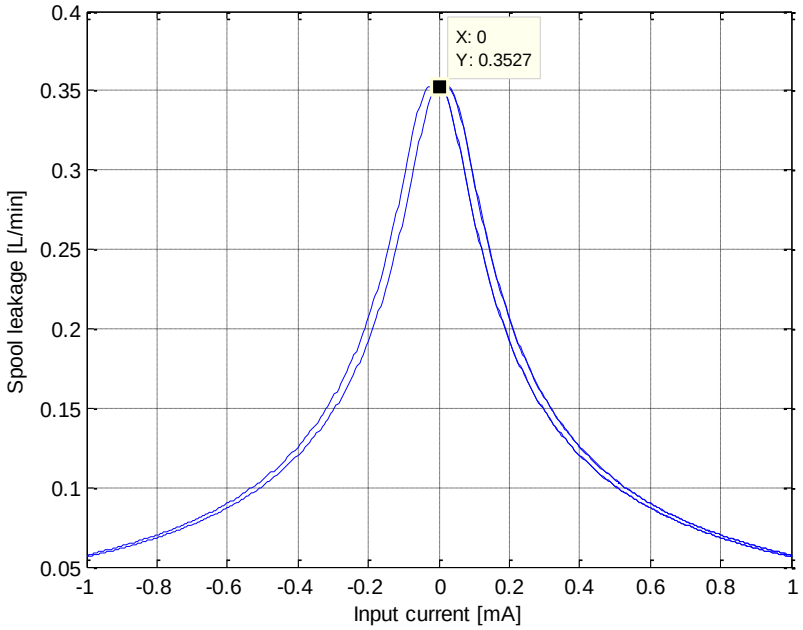

Figure 4.17 - Predicted spool leakage curve of Moog Series 31 Servovalve

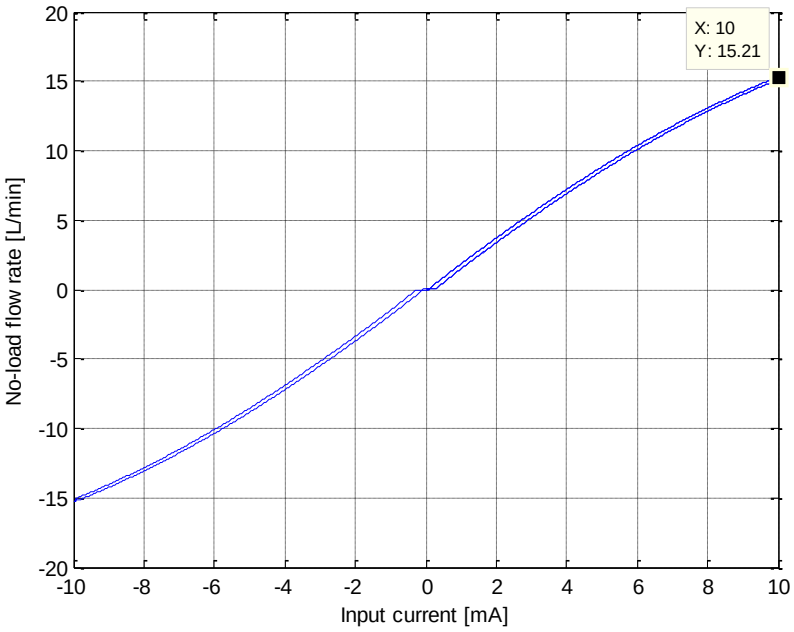

Figure 4.18 – No-load flow curve with 5 µm overlapped metering ports

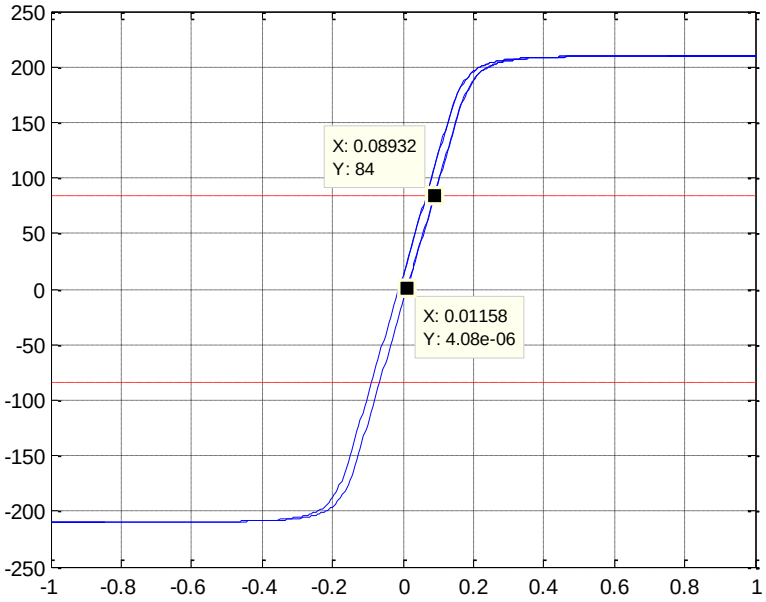

Figure 4.19 – Load pressure curve with 5 µm overlapped metering ports

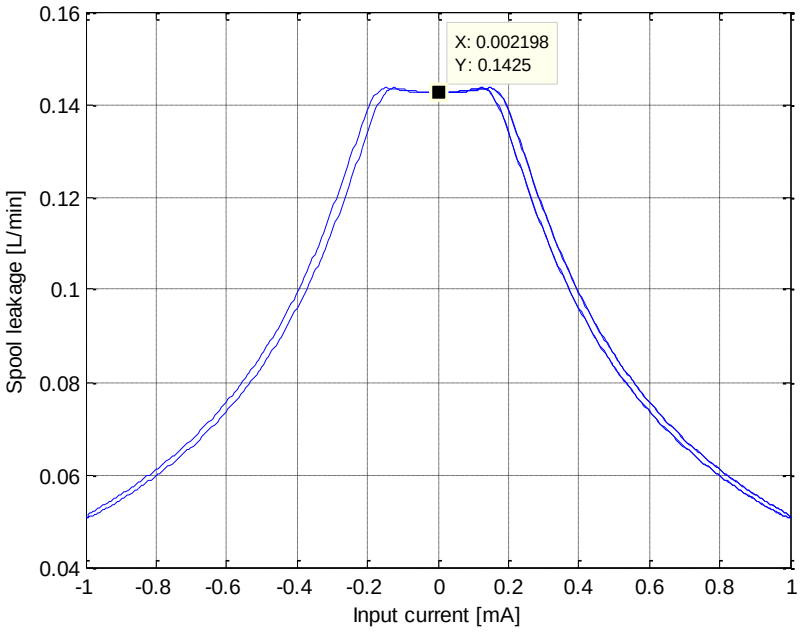

Figure 4.20 – Spool leakage curve with 5 µm overlapped metering ports

If all the ports were underlapped by 5 µm, a higher flow gain region would be created around the null position of the no-load flow curve as shown in Figure 4.21.

Its load pressure and spool leakage curves would become as shown in Figure 4.22 and Figure 4.23. As seen the spool leakage greatly increases by underlapping the ports exceeding maximum leakage of 1 L/min given in the datasheet.

As shown in the examples, little deviations in the geometric dimensions of a servovalve ccan cause drastic changes in the performance. With the developed model, effects of all the parameters on a servovalves performance can be examined. This could be helpful in many ways, such as determining geometric tolerances or diagnosing a servovalve if the performance data is available.

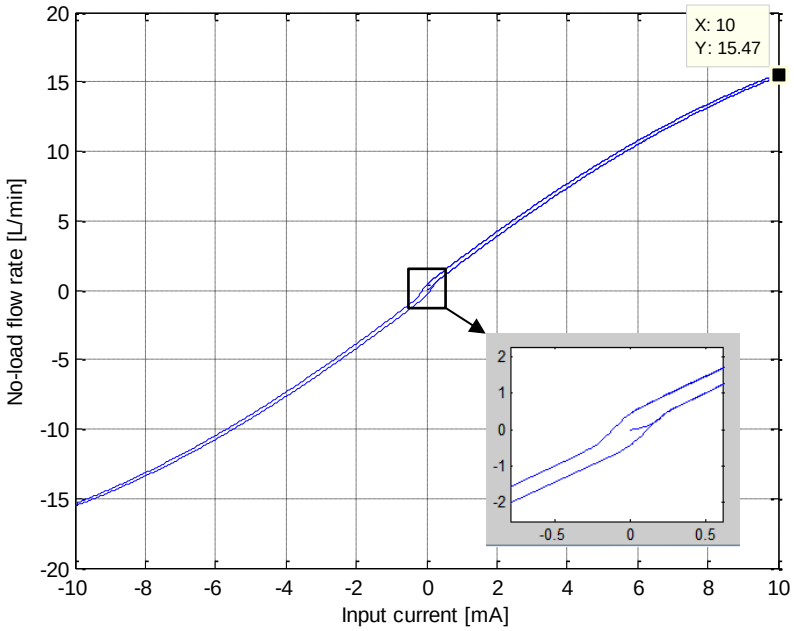

Figure 4.21 – No-load flow curve with 5 µm underlapped metering ports

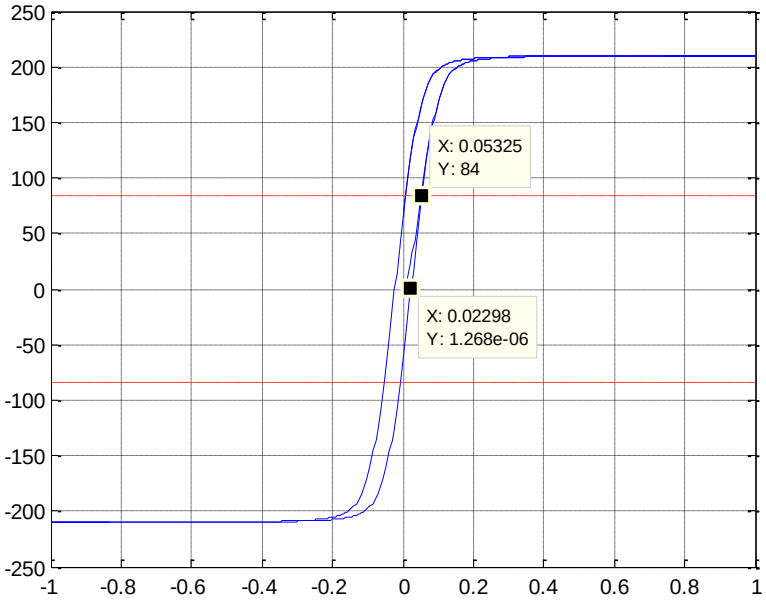

Figure 4.22 – Load pressure curve with 5 µm underlapped metering ports

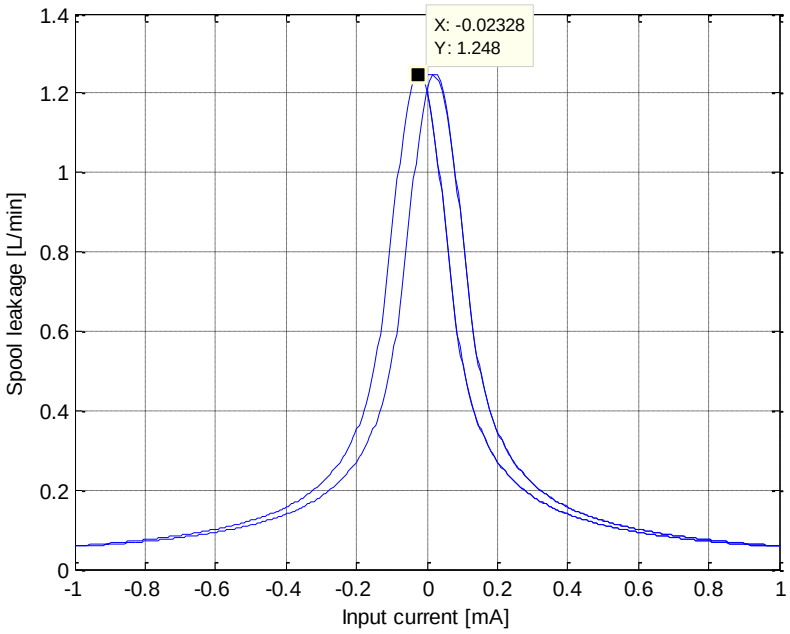

Figure 4.23 – Spool leakage curve with 5 µm underlapped metering ports

CHAPTER 5

SUMMARY AND CONCLUSIONS

5.1. Summary

In the present study, a simulation model for double stage nozzle-flapper type electrohydraulic servovalves is developed. Motivation behind this attempt is to create a complete servovalve model that simulates the effects of all the geometric dimensions on its performance so it can be used as a geometric tolerance analysis tool. The model simulates the effects of several critical parameters of a servovalve on its performance, such as port lappings, first stage geometric dimensions, manifold resistance, fluid properties, etc.

The development process begins with summarizing the existing relations defining servovalve hydraulics and underlining their deficiencies. Then more accurate analytical models are developed, starting with a nozzle-flapper valve model, which is used as the first stage of a double stage servovalve combined with a pair of fixed orifices. For model development, most accurate turbulence models and wall functions are determined by comparing fixed orifice experimental pressure drop vs. flow rate data with the ones found using numerical analyses. After that, a more accurate analytical model for nozzle-flapper valve is suggested. The model treats the nozzle as a combination of a fixed and a variable orifice connected in serial, as opposed to the common approach of modeling it as just a variable orifice. The suggested first stage model needs three discharge coefficients to be determined, one for the fixed orifice of the first stage and two for the nozzle. By the help of CFD again, discharge coefficients related to fixed orifice and nozzles are determined numerically.

Another model is developed for the second stage of the servovalve, i.e., the spool valve. The problem of invalidity of the equation that defines the relation between the pressure drop and flow rate for an annular gap (i.e., the overlapped case) around zero lap length is solved by modifying the existing expression. This modification is carried out by introducing a new constant to the denominator to prevent it to go to zero as lap length approaches to zero. The definition of this constant is found by imposing the constraint that implies the equations defining the flow rates for underlapped and overlapped cases should yield the same result at zero lap length. To ensure that the transition between these equations is smooth, another constraint is imposed equating the slopes of the equations at zero lap length. This second constraint led to the result that the discharge coefficient for a spool valve port must be modeled as a variable to make the smooth transition possible. Then, the discharge coefficient is determined by the help of CFD as a function of Reynolds' number and geometry, and the model is completed.

By combining the developed models in the SimScape® environment, a complete servovalve model is created as the result.

5.2. Conclusions

Performance of the model is tested using the parameters provided by the Moog, Inc. for their Series 31 Servovalve [4]. Many parameters, which are missing in the datasheet, are predicted to use them with the model. Despite this prediction probably has errors, the model is able to yield accurate results. So, it is concluded that the model is promising, and by further tuning with more reliable datasets it could be used as a geometric tolerance analysis or a diagnosis tool with a high accuracy.

Lastly, the effects of changing the port lappings on the servovalve static performance metrics no-load flow, pressure sensitivity and spool leakage are examined using the model and the results are discussed. Such analyses can be made for all the other

parameters by the help of the developed model to aid the designers with finding the best dimensions to meet the performance requirements, determination of the tolerances for these dimensions and understand the servovalve behavior under different conditions.

5.3. Recommendations for Future Work

Since a full set of parameters is not available for the servovalve modeled and investigated in this study, only a partial validation of the model is carried out in this thesis. So, there is still room for a much reliable validation and update to increase the accuracy if a complete and correct set of parameters and performance data could be obtained.

Moreover, the present model is developed for the hydraulics of a servovalve, but the torque motor component is not modeled in detail. Efforts should be made towards building a detailed torque motor model and integrate it into the present model.

REFERENCES

[1] The McGraw-Hill Companies, Inc., Dictionary of Engineering, 2. Ed., McGraw-Hill, 2003.

[2] Moog GmbH, «D634-P Series Direct Drive Proportional Valve».

[3] J. Blackburn, G. Reethof ve J. Shearer, Fluid Power Control, Massachusetts: The MIT Press, 1960.

[4] Moog Inc., «Type 30 Nozzle-Flapper Flow Control Servovalves».

[5] A. Plummer, «Electrohydraulic servovalves – past, present, and future,» *10th International Fluid Power Conference*, Dresden, 2016.

[6] Parker Hannifin Corporation, «Parker Abex Jet-Pipe® Servovalves - Model 425».

[7] MTS Systems Corporation, «Series 256 Servovalves».

[8] H. E. Merritt, Hydraulic Control Systems, NY: John Wiley & Sons Inc., 1967.

[9] J. Watton, Fundamentals of Fluid Power Control, Cambridge: Cambridge University Press, 2009.

[10] D. Gall ve F. Steghart (Tinsley Industrial Instruments Ltd), «Improvements in or relating to Servo Systems». Patent: GB620688, March 1949.

[11] H. B. Kolm-Jr., «Flow Control Servo Valve with Dynamic Load Pressure Feedback». ABD Patent: 3,095,906, 2 June 1963.

[12] W. B. Lloyd, «Pressure Feedback Servo Valve». ABD Patent: 2,889,815, 9 June 1959.

[13] J. W. Blanton, «Servo Valve with Flow Rate Feedback». ABD Patent: 3,054,388, 18 September 1962.

[14] A. C. Lancaster Jr. ve D. I. H. Tonawanda (Moog Servocontrols), «Mechanical Feedback Flow Control Servo Valve». East Aurora, N.Y. Patent: 3,023,782, 6

March 1962.

[15] S. Karunanidhi ve M. Singaperumal, «Mathematical modelling and experimental characterization of a high dynamic servo valve integrated with piezoelectric actuator,» *J. Systems and Control Engineering,* vol. 224, pp. 419-432, 2010.

[16] S. Karunanidhi ve M. Singaperumal, «Design, analysis and simulation of magnetostrictive actuator and its application to high dynamic servo valve,» *Sensors and Actuators A,* vol. 157, pp. 185-197, 2010.

[17] Alibaba Group, «Jack Ma on the China Opportunity at Gateway '17,» 21 June 2017. [Online]. Available: https://www.youtube.com/watch?v=B0vkX-CzKTY. [Accessed: 11 November 2017].

[18] M. Ivantysynova, «Technologies and Innovations for Hydraulic Pumps,» *10th International Fluid Power Conference*, Dresden, 2016.

[19] W. Anderson, Controlling Electrohydraulic Systems, New York: Marcel Dekker, Inc., 1988.

[20] M. G. Rabie, Fluid Power Engineering, McGraw Hill, 2009.

[21] S. J. Lin ve A. Akers, «The Predicted Performance of a Flapper-Nozzle Valve: Comparison with Expretiment,» *American Control Conference*, Atlanta, USA, 1988.

[22] D. McCloy ve H. R. Martin, Control of Fluid Power, Analysis and Design, Halsted Press, 1980.

[23] S. J. Lin ve A. Akers, «A Dynamic Model of the Flapper-Nozzle Component of an Electrohydraulic Servovalve,» *Journal of Dynamic Systems Measurement and Control,* no. 111, pp. 105-109, 1989.

[24] S. J. Lin ve A. Akers, «A Nonlinear Model of a Flapper-Nozzle Valve,» *American Control Conference*, Pittsburgh, USA, 1989.

[25] N. Z. Aung, Q. Yang, M. Chen ve S. Li, «CFD analysis of flow forces and energy loss characteristics in a flapper–nozzle pilot valve with different null clearances,» *Energy Conversion and Management,* no. 83, p. 284–295, 2014.

[26] Y. Zhu ve S. Fei, «Design criterion involving comprehensive performance characteristics of nozzle–flapper valves,» *J Systems and Control Engineering*, vol. 5, no. 230, pp. 452-466, 2016.

[27] L. Li, H. Yan, H. Zhang ve J. Li, «Numerical simulation and experimental research of the flow force and forced vibration in the nozzle-flapper valve,» *Mechanical Systems and Signal Processing*, no. 99, p. 550–566, 2017.

[28] A. Kılıç, S. Kapucu, S. Bayseç ve J. R. Jones, «İki kademeli elektro hidrolik valfin kanatçık valf modeli ve kanatçık nozul boşluğu basıncının incelenmesi,» *VIII. Ulusal Hidrolik Pnömatik Kongresi*, İzmir, 2017.

[29] J. Watton, «The Effect of Drain Orifice Damping on the Performance Characteristics of a Servovalve Flapper/Nozzle Stage,» *Journal of Dynamic Systems, Measurement, and Control*, vol. 109, no. 1, pp. 19-23, 1987.

[30] A. Ellman, K. Koskinen ve M. Vilenius, «Through-Flow in Short Annulus of Fine Clearance,» *International Mechanical Engineering Congress and Exposition*, San Francisco, CA, 1995.

[31] A. Ellman, «Leakage Behaviour of Four-Way Servovalve,» *Fluid Power Systems and Technology*, vol. 5, pp. 163-167, 1998.

[32] A. Ellman ve T. Virvalo, «Formation of Pressure Gain in Hydraulic Servovalves and its Significance in System Behavior,» *International Mechanical Engineering Congress and Exposition*, Atlanta, GA, 1996.

[33] B. Eryılmaz ve B. H. Wilson, «Combining Leakage and Orifice Flows in a Hydraulic Servovalve Model,» *Journal of Dynamic Systems, Measurement and Control*, vol. 122, pp. 576-579, 1999.

[34] M. Feki ve E. Richard, «Including Leakage Flow in the Servovalve Static Model,» *International Journal of Modelling and Simulation*, vol. 25, no. 1, pp. 51-56, 2005.

[35] S. Mookherjee, S. Acharyya, K. Majumdar ve D. Sanyal, «Static-performance based computer-aided design of a DDV and its sensistivity analysis,» *International Journal of Fluid Power*, vol. 2, no. 2, pp. 47-63, 2001.

[36] D. Gordić, M. Babić ve N. Jovičić, «Modelling of Spool Position Feedback Servovalves,,» *International Journal of Fluid Power,* vol. 5, no. 1, pp. 37-51, 2004.

[37] D. Gordić, M. Babić, D. Milanovic ve S. Savic, «Spool Valve Leakage Behaviour,» *Arch Civil Mech Eng,* pp. 859-866, 2011.

[38] T. Nakada ve Y. Ikebe, «Measurement of unsteady axial flow force on a spool valve,» *IFAC Pneumatic & Hydraulic Components,* pp. 193-198, 1980.

[39] Y. Ikebe ve H. Ohuchi, «Generalized formulation of momentum theory,» *Fluidic Quarterly,* no. 10, pp. 27-46, 1978.

[40] A. C. Afatsun ve T. Balkan, «(In Turkish) Orifis Akışı Çözümlemelerinde Türbülans Modellerinin Başarımlarının Karşılaştırılması,» *HPKON 2017*, İzmir, 2017.

[41] X. Pan, G. Wang ve Z. Lu, «Flow field simulation and a flow model of servo-valve spool valve orifice,» *Energy Conversion and Management,* no. 52, p. 3249–56, 2011.

[42] A. Posa, P. Oresta ve A. Lippolis, «Analysis of a directional hydraulic valve by a Direct Numerical Simulation using an immersed-boundary method,» *Energy Conversion and Management,* no. 65, p. 497–506, 2013.

[43] J. R. Valdes, J. M. Rodriguez, J. Saumell ve T. Pütz, «A methodology for the parametric modelling of the flow coefficients and flow rate in hydraulic valves,» *Energy Conversation and Management,* no. 33, pp. 598-611, 2014.

[44] J. R. Valdes, M. J. Miana, J. L. Nunez ve T. Pütz, «Reduced order model for estimation of fluid flow and flow forces in hydraulic proportional valves,» *Energy Conversation and Management,* no. 49, pp. 1517-29, 2008.

[45] M. K. Mondal, N. K. Manna ve R. Saha, «Study of leakage flow through a spool valve under blocked-actuator port condition - Simulation and experiment,» *J Mechanical Engineering Science,* vol. 8, no. 228, p. 1405–17, 2014.

[46] K. O. Eyyüpoglu, «Development of a novel surface damping treatment (M.Sc.

Thesis),» Middle East Technical University, Ankara, 2016.

[47] ANSYS, Inc., ANSYS Fluent Theory Guide, Canonsburg, PA: ANSYS, Inc., 2017.

[48] P. Promvonge ve K. Silapabanleng, «Simulation of Turbulent Flow through a Circular Orifice,» *13th National Mechanical Engineering Conference*, South Pattaya, Cholburi, 1999.

[49] *MATLAB R2013b Simscape Hydraulic Fluid Database.*

[50] K. W. Linfield, «A study of the discharge coefficient of jets from angled slots and conical orifices (Ph.D. Thesis),» University of Toronto, 2000.

[51] J. H. L. V ve J. H. L. (IV), «Velocity Coefficients For Free Jets From Sharp-Edged Orifices,» *Journal of Fluids Engineering*, vol. 106, pp. 13-17, 1984.

[52] C. L. Hollingshead, «Discharge Coefficient Performance of Venturi, Standard Concentric Orifice Plate, V-Cone, and Wedge Flow (M.Sc. Teshis),» Utah State University, 2011.

[53] H. D. Burghardt, Machine Tool Operation - Part II: Drilling Machine, Shaper and Planer, Milling and Grinding Machines, Spur Gears and Bevel Gears, NY: McGraw-Hill Book Company, 1922.

[54] F. Moukalled, L. Mangani ve M. The Finite Volume Method Darwish, The Finite Volume Method in Computational Fluid Dynamics, Cham, Switzerland: Springer International Publishing, 2015.

[55] SAE, «ARP 490: Electrohydraulic Servovalves,» SAE International, Warrendale, PA, 1993.

[56] «WebPlotDigitizer,» [Online]. Available: https://automeris.io/WebPlotDigitizer. [Accessed: 30 03 2019].

[57] R. Park, «Contamination Control - A Hydraulic OEM Perspective,» Moog Australia Pty Ltd, Melbourne, 1997.

[58] F. Beer, E. Johnston, J. DeWolf ve D. Mazurek, Mechanics of Materials (5th Ed.), Singapore: McGraw-Hill, 2009.

APPENDICES

A. MATLAB Codes

Linearization of the definitions of torque applied on the flapper by the fluid jets exiting the nozzles and the control force on the spool (i.e., T_n and F_c);

```
syms Ps Pl Pr Cdf Cdn rho xf Dn Df x0 Lf Ds xsd theta
An      = pi*Dn^2/4;
As      = pi*Ds^2/4;
xf      = Lf*theta

Qfl     = Cdf*pi*Df^2/4*sqrt(2/rho*(Ps-Pl));
Qnl     = Cdn*pi*Dn*(x0+xf)*sqrt(2/rho*Pl);
Pl      = solve(Qfl == Qnl - As*xsd, Pl);
Pl      = Pl(2);
Qnl     = Cdn*pi*Dn*(x0+xf)*sqrt(2/rho*Pl);
ul      = Qnl/An;
Fnl     = An*(Pl + 1/2*rho*ul^2);

Qfr     = Cdf*pi*Df^2/4*sqrt(2/rho*(Ps-Pr));
Qnr     = Cdn*pi*Dn*(x0-xf)*sqrt(2/rho*Pr);
Pr      = solve(Qfr == Qnr + As*xsd, Pr);
Pr      = Pr(2);
Qnr     = Cdn*pi*Dn*(x0-xf)*sqrt(2/rho*Pr);
ur      = Qnr/An;
Fnr     = An*(Pr + 1/2*rho*ur^2);

Tn      = Lf*(Fnl-Fnr);
D_Tn    = subs(diff(Tn,theta),[theta xsd],[0 0])* theta +
subs(diff(Tn,xsd),[ theta xsd],[0 0])*xsd;

Fc      = As*(Pr-Pl);
D_Fc    = subs(diff(Fc,theta),[theta xsd],[0 0])* theta +
subs(diff(Fc,xsd),[ theta xsd],[0 0])*xsd;
```

Symbolic manipulation to find $\tilde{x}_0$ definition for Model 3;

```
syms Cdf Cdv Cdn Cde Df De Dn x0 xf rho Ps Pr Pl Pe
Cd1=Cdv*Cdn*Cde; %For simplification
Cd2=Cdv*Cdn*Cdf; %For simplification
L = Cde^2*De^4*(16*Cdv^2*x0^2+Cdn^2*Dn^2)+64*Cdv^2*Cdn^2*Dn^4*x0^2; %Lambda
Qfr = Cdf*pi*Df^2/4*sqrt(2/rho*(Ps-Pr)); %Fixed orifice flow rate (right)
Qnr = Cdv*Cdn*pi*Dn^2*(x0-xf)/sqrt(16*Cdv^2*(x0-xf)^2+Cdn^2*Dn^2)...
    *sqrt(2/rho*(Pr-Pe)); %Nozzle flow rate (right)
Qfl = Cdf*pi*Df^2/4*sqrt(2/rho*(Ps-Pl)); %Fixed orifice flow rate (left)
Qnl = Cdv*Cdn*pi*Dn^2*(x0+xf)/sqrt(16*Cdv^2*(x0+xf)^2+Cdn^2*Dn^2)...
    *sqrt(2/rho*(Pl-Pe)); %Nozzle flow rate (left)
Pr = solve(Qfr == Qnr,Pr); %Pressure at right branch
Pl = solve(Qfl == Qnl,Pl); %Pressure at left branch
Pc = Pr-Pl; %Control pressure
Pe_d = 64*Cd2^2*Df^4*Dn^4*x0^2*Ps/(16*Cd1^2*Dn^4*De^4*x0^2+Cdf^2*Df^4*L;
%Exit pressure definition
DPc = subs(diff(Pc,xf),[xf Pe],[0 Pe_d)]); %Control pressure sensitivity at
xf=0
x0_max = solve(diff(DPc,x0),x0); %Curtain length for max. control pressure
sensistivity (2 roots obtained)
x0_max = x0_max(2); %Second root is the positive one
```

Symbolic manipulation to find $\tilde{x}_0$ definition for Model 3 with $P_e = 0$;

```
syms Cdf Cdv Cdn Cde Df De Dn x0 xf rho Ps Pr Pl
Cd1=Cdv*Cdn*Cde; %For simplification
Cd2=Cdv*Cdn*Cdf; %For simplification
L = Cde^2*De^4*(16*Cdv^2*x0^2+Cdn^2*Dn^2)+64*Cdv^2*Cdn^2*Dn^4*x0^2; %Lambda
Qfr = Cdf*pi*Df^2/4*sqrt(2/rho*(Ps-Pr)); %Fixed orifice flow rate (right)
Qnr = Cdv*Cdn*pi*Dn^2*(x0-xf)/sqrt(16*Cdv^2*(x0-xf)^2+Cdn^2*Dn^2)...
    *sqrt(2/rho*Pr); %Nozzle flow rate (right)
Qfl = Cdf*pi*Df^2/4*sqrt(2/rho*(Ps-Pl)); %Fixed orifice flow rate (left)
Qnl = Cdv*Cdn*pi*Dn^2*(x0+xf)/sqrt(16*Cdv^2*(x0+xf)^2+Cdn^2*Dn^2)...
    *sqrt(2/rho*Pl); %Nozzle flow rate (left)
Pr = solve(Qfr == Qnr,Pr); %Pressure at right branch
Pl = solve(Qfl == Qnl,Pl); %Pressure at left branch
Pc = Pr-Pl; %Control pressure
DPc = subs(diff(Pc,xf),xf,0); %Control pressure sensitivity at xf=0
x0_max = solve(diff(DPc,x0),x0); %Curtain length for max. control pressure
sensistivity (2 roots obtained)
x0_max = x0_max(1) %First root is the positive one
```

B. Bending of flexure tube and determination of L_f and L_s

Flexure tube and flapper are two beams fixed together from one end (upper end). The other end of the flexure tube is fixed to the valve manifold, while the other end of the flapper is free to move.

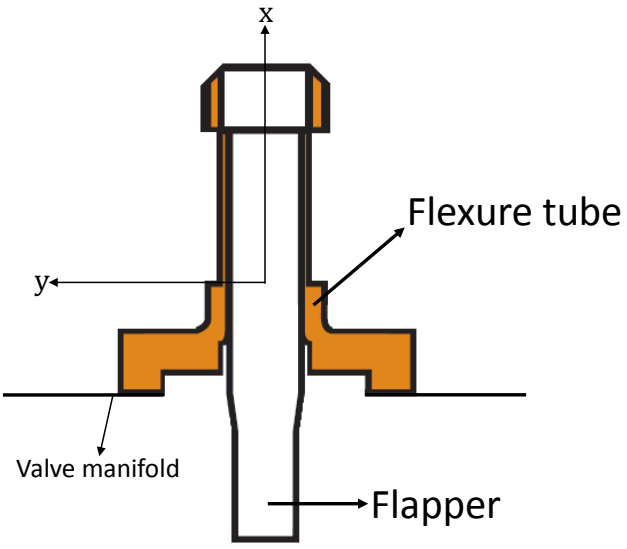

Figure A.1 – Flexure tube and flapper

The upper end of the flexure tube is subjected to a torque from the torque motor. For a beam which is fixed on the one end and subjected to a torque from the other, deflection of the moving end (maximum deflection) is calculated by [58];

$$y = -\frac{TL^2}{2EI} \tag{A.1}$$

and the slope of the moving end is calculated by [58];

$$\frac{dy}{dx} = -\frac{TL}{EI} \tag{A.2}$$

where T is the torque applied, L is the length of beam which is the length of the thinnest section of the flexure tube, E is the elastic modulus of the material and I is the bending moment of inertia of the geometry. When the torque is applied flexure

tube bends and flapper rotates with it since it is free on the lower end. Center of this rotation can be found by calculating the point a line cuts the x axis, which passes through the point $(x, y) = (L, -\frac{TL^2}{2EI})$ and has the slope given in equation (A.2).

A line is defined by;

$$y = ax + b \tag{A.3}$$

Since a is the slope it is known that $a = -\frac{TL}{EI}$. b can be found by imposing the end point constraint;

$$-\frac{TL^2}{2EI} = -\frac{TL}{EI}L + b \rightarrow b = \frac{TL^2}{2EI} \tag{A.4}$$

So, the point this line cuts the x axis can be found by;

$$0 = -\frac{TL}{EI}x + \frac{TL^2}{2EI} \rightarrow x = \frac{L}{2} \tag{A.5}$$

So, the pivot point of the flapper will always be the middle point of the thinnest section of flexure tube. L_f is equal to the distance from this point to the nozzle axis, and L_s is equal to the distance from this point to the point where the feedback spring touches the spool.

C. Bernoulli Force SimScape Block Source Code

```
component berno < foundation.mechanical.translational.branch
% Bernoulli force

inputs
    P = { 0, 'Pa' }; % P:left
end

parameters
    grad = { 10, 'mm' };  % Port gradient
    K_B  = { .46, '1' };  % Bernoulli force constant
end

variables
    x = { 0, 'm'};
end

function setup
    if grad <= 0
        pm_error('simscape:GreaterThanZero','Spring rate' )
    end
end

equations
    v == x.der;
    f == K_B*grad*P*x;
end

end
```

D. Spool Port SimScape Block Source Code

```
component spool_model
% Spool valve port

nodes
    U = foundation.hydraulic.hydraulic; % U:left
    D = foundation.hydraulic.hydraulic; % D:right
end

inputs
    S = { 0, 'um' }; % S:left
end

variables
    pressure        = {80e5, 'Pa' };        % Pressure differential
    flow_rate       = {3e-06 , 'm^3/s' };   % Flow rate
    Cd              = {0.4, '1' };          % Discharge Coefficient
    logRe           = {1, '1'};
end

parameters
    R               = {2.5, 'mm'}; % Spool radius
    B               = {2,'um' };   % Radial clearance
    beta            = {1,'1' };    % Port gradient to sleeve perimeter
ratio
    iL              = {0,'um'};    % Port lapping
end

branches
    flow_rate : U.q -> D.q;
end

equations
    let
        mu = U.viscosity_kin*U.density;
        state = iL+S;
    in
        pressure == U.p - D.p;
        if state >= 0
            logRe == log10(B*sqrt(2*pressure*U.density)/mu + 1);
            Cd == .77*(logRe^4+logRe)*exp(-.09*logRe^(-.3))/(logRe^4-
3.6*logRe+7.2);
            flow_rate ==
pi*R*B^3*pressure/(6*mu*state+B^2*sqrt(U.density*pressure/2)/(2*Cd));
        else
            logRe == log10(sqrt(B^2+state^2)*sqrt(2*pressure*U.density)/mu
+ 1);
            Cd == .77*(logRe^4+logRe)*exp(-.09*logRe^(-.3))/(logRe^4-
3.6*logRe+7.2)*(1+(.34-.31*tanh(.05*logRe^5))*(B/sqrt(B^2+state^2)-
state/sqrt(B^2+state^2)-1)/(sqrt(2)-1));
            flow_rate ==
2*Cd*pi*R*sqrt((state^2+B^2)*2/U.density*pressure);
        end
    end
end
end
```

E. Typical Parameters for Moog Series 31 Servovalve

Table C.1 – Typical parameters for Moog Series 31 Servovalve in SI units

Parameter	Definition	Value
i	Torque motor current	±10 mA
x_s	Spool displacement	381 µm max
Q_{max}	Servovalve control flow	15.1 L/min (@70 bar)
K_1	Torque motor gain	0.00282 N·m/mA
K_2	Hydraulic amplifier flow gain	0.0059 (L/min)/µm
K_3	Flow gain of spool	0.0405 (L/min)/µm
A	Spool end area	16.8 mm^2
k_f	Net stiffness on armature/flapper	511 N·m/m
k_w	Feedback spring stiffness	74.3 N·m/m
b_f	Net damping on armature/flapper	0.071 N·m/(m/s)
J_f	Rotational mass of armature/flapper	1.96e-5 N·m/(m/s^2)
ω_n	Natural frequency of first stage	814 Hz
ζ	Damping ratio of first stage	0.4

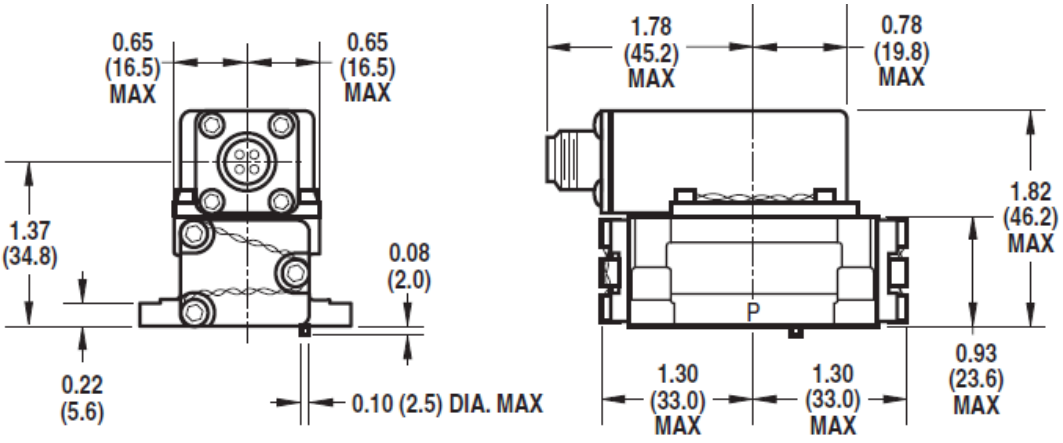

Figure C.1 – Dimension of Moog Series 31 Servovalve [4]

F. Parameter set used in Moog Series 31 Servovalve simulation

```
P_s      = 70e5;      %[Pa] Source pressure
rho      = 860;       %[kg/m^3] Mass density of MIL-H-5606 @20 oC
mu       = .018;      %[Pa*s] Dynamic viscosity of MIL-H-5606 @20 oC
beta     = 1.556e9;   %[Pa] Bulk modulus

k_T      = 2.82;      %[Nm/A] Torque motor gain
k_A      = 4.53;      %[Nm/rad] Armature stiffness
k_fb     = 3560;      %[N/m] Feedback spring stiffness
J_A      = 1.74e-7;   %[kg*m^2/rad] Armature intertia
b_T      = 6.3e-4;    %[Nm/(rad/s)] First stage damping coefficient

L_f      = 8.87e-3;   %[m] Pivot point to nozzle axis length
L_s      = 20.87e-3;  %[m] Pivot point to feedback-spring-ball-center length

C_dv     = .75;       %[] Discharge coef. of nozzle variable part
C_dn     = .82;       %[] Discharge coef. of nozzle fixed part
C_df     = .73;       %[] Discharge coef. of fixed orifice
C_dE     = .70;       %[] Discharge coef. of exit orifice
D_f      = 200e-6;    %[m] Fixed orifice diameter
D_n      = 200e-6;    %[m] Nozzle diameter
x_0      = 40e-6;     %[m] Initial nozzle opening (Right)
A_entry  = 3.24e-6;   %[m^2] Entry orifice area

m_s      = 3e-3;      %[kg] Spool mass
D_s      = 4.625e-3;  %[m] Spool diameter
w        = 12e-3;     %[m] Port gradient
wr       = w/pi/D_s;  %[] Spool gradient (w) to perimeter (pi*D_s) ratio
B        = 2e-6;      %[m] Radial clearance between spool and sleeve
F_stiction  = 1;      %[N] Breakaway friction on the spool
F_coulomb   = .8;     %[N] Coulomb friction on the spool
```